UNIVERSIDADE
BEIRA INTERIOR

Design and characterization of Ta and Sr ion doped tricalcium phosphate bioceramic

(Versão final após defesa)

Gabriel Flor Alves Rodrigues Barreira da Costa

Dissertação para obtenção do Grau de Mestre em
Bioengenharia
(2º ciclo de estudos)

Orientador: Prof. Doutor Abílio Manuel Pereira Silva
Co-Orientador: Prof. Doutor Mariusz Winiecki
Co-Orientador: Mestre Natanael Filipe Ferreira Fernandes

dezembro 2024

Declaração de Integridade

Eu, Gabriel Flor Alves Rodrigues Barreira da Costa, que abaixo assino, estudante com o número de inscrição M12872 de/o Bioengenharia da Faculdade de Engenharia, declaro ter desenvolvido o presente trabalho e elaborado o presente texto em total consonância com o **Código de Integridades da Universidade da Beira Interior**.

Mais concretamente afirmo não ter incorrido em qualquer das variedades de Fraude Académica, e que aqui declaro conhecer, que em particular atendi à exigida referenciação de frases, extratos, imagens e outras formas de trabalho intelectual, e assumindo assim na íntegra as responsabilidades da autoria.

Universidade da Beira Interior, Covilhã 12 / 12 /2024

Assinado por: **Gabriel Flor Alves Rodrigues Barreira da Costa**
Num. de Identificação: 14595171
Data: 2024.12.12 14:13:30+00'00'

(assinatura conforme Cartão de Cidadão ou preferencialmente

assinatura digital no documento original se naquele mesmo formato)

Acknowledgements

I would like to express my deepest gratitude to all those who supported me throughout this dissertation journey. Without their encouragement, assistance, and understanding, this project would not have been possible.

To my advisor, Professor Doctor Abílio Manuel Pereira da Silva, who believed in my potential and gave me the opportunity to work alongside him, for his constant availability and understanding whenever I needed it, for the knowledge he shared, the questions he answered, the solutions to achieve the desired results, and his continuous encouragement throughout this time.

To my co-advisors, Professor Doctor Mariusz Winiecki, for suggesting the topic, sharing his knowledge in the field of metals, providing the materials for applying the coatings, and for his availability whenever I needed it, and to Master Natanael Filipe Ferreira Fernandes, for his support in the laboratory, sharing of cellular knowledge, and his availability to clarify doubts.

To C-MAST-UBI (Centre for Mechanical and Aerospace Science and Technologies) and CICS-UBI (Health Sciences Research Centre of the University of Beira Interior) for providing all the necessary conditions for the completion of this dissertation.

To the electron microscopy laboratory of the UBI Optics Center, particularly to Doctor Ana Paula Gomes, for preparing the samples, providing the equipment, and conducting the X-ray diffraction and scanning electron microscopy tests. To SAI (Servicio General de Apoyo a la Investigación) of the University of Zaragoza, for providing the field emission scanning electron microscope.

Special thanks to my parents for the education they provided, for the support and affection they have always given me, for their encouragement, and for providing all the necessary conditions to complete this stage, without them, I would not be who I am today.

Finally, I want to thank all my laboratory colleagues and friends—Duarte, Kateryna, João, Rodrigo, Ana, Júlia, and Beatriz—who helped me, shared their knowledge, and supported me to reach this point.

To all, my sincere thanks!

Resumo

Com o envelhecimento da população, os desafios na regeneração óssea tornam-se mais frequentes, criando a necessidade de alternativas eficazes que melhorem o bem-estar. Uma solução comum é o uso de materiais metálicos, como titânio e aço inoxidável, em implantes ortopédicos e dentários. No entanto, estes materiais, apesar das suas qualidades mecânicas e biológicas, podem sofrer troca iónica (corrosão) e causar reações adversas nos tecidos como metalose. Para mitigar esses problemas, o uso de cerâmicas, como o fosfato tricálcico (TCP), tem sido explorado como substituto ou revestimento metálico. O TCP é valorizado pelas suas propriedades bioativas, osteoindutoras e reabsorvíveis, facilitando a osteocondução.

A dopagem do TCP com iões metálicos, como estrôncio e tântalo, é uma melhoria que promove a função dos osteoblastos, inibindo a reabsorção óssea e aumentando a resistência mecânica e biocompatibilidade. Neste trabalho, foram desenvolvidas amostras de TCP dopado com tântalo, estrôncio e ambos, para avaliar seu desempenho como substituto ósseo e revestimento.

A caracterização das biocerâmicas demonstra que as composições apresentam propriedades promissoras. A incorporação de Sr isoladamente aumenta significativamente a resistência mecânica, 7,6 MPa para 12,9 MPa. Além disso, a incorporação combinada de Ta e Sr aumenta a porosidade de 24% para 34%, enquanto mantém a viabilidade celular próxima de 100% em todas as composições. Ademais, confirma-se que todas as composições são adequadas para a produção de revestimentos biocerâmicos em substratos de titânio.

Palavras-chave

Biocerâmicas; TCP dopado com Ta e Sr; resistência mecânica; revestimento cerâmico.

Abstract

With the aging population, challenges in bone regeneration are becoming more frequent, creating the need for effective alternatives that improve well-being. A common solution is the use of metallic materials, such as titanium and stainless steel, in orthopedic and dental implants. However, these materials, despite their mechanical and biological qualities, can undergo ionic exchange (corrosion) and cause adverse reactions in tissues, such as metallosis. To mitigate these problems, the use of ceramics, such as tricalcium phosphate (TCP), has been explored as a substitute or metallic coating. TCP is valued for its bioactive, osteoinductive, and resorbable properties, facilitating osteoconduction.

Doping TCP with metallic ions, such as strontium and tantalum, is an enhancement that promotes the function of osteoblasts, inhibits bone resorption, and increases mechanical strength and biocompatibility. In this work, samples of TCP doped with tantalum, strontium, and both were developed to evaluate their performance as bone substitutes and coatings.

The characterization of the bioceramics demonstrates that the compositions exhibit promising properties. The incorporation of Sr alone significantly enhances the mechanical strength, increasing it from 7.6 MPa to 12.9 MPa. Additionally, the combined incorporation of Ta and Sr increases porosity from 24% to 34%, while maintaining cell viability close to 100% across all compositions. Furthermore, it is confirmed that all compositions are suitable for producing bioceramic coatings on titanium substrates.

Keywords

Bioceramics; TCP doped with Ta and Sr; mechanical strength; ceramic coating.

Table of Content

List of Figures

List of Tables

Abbreviations List

Nomenclature

316 L	Stainless Steel with Low carbon content
3D	Three Dimensional
BCP	Biphasic Calcium Phosphate
BSE	Backscattered Electron
CAS-No	Chemical Abstracts Service Number
CICS	Health Sciences Research Centre
C-MAST	Center for Mechanical and Aerospace Science and Technologies
Co-Cr	Cobalt-Chrome alloy
CP Ti	Commercially Pure Titanium
CP	Commercially Pure
CVD	Chemical Vapor Deposition
DEM	Department of Electromechanical Engineering
DGUN	Detonation Gun
DMEM-F12	Dulbecco's Modified Eagle Medium/Nutrient Mixture F-12
DNA	Deoxyribonucleic acid
EHT	Electron High Tension
FBS	Fetal Bovine Serum
FCS	Faculty of Health Sciences
FDA	Food Drug Administration
FESEM	Field Emission Scanning Electron Microscope
HA	Hydroxyapatite
hOB	Human osteoblast cells
HV	Vickers Hardness
HVOF	High Velocity Oxygen Fuel
k^-	Negative Control
k^+	Positive Control
PMMA	Polymethyl Methacrylate
PSD	Particle Size Distribution
PTFE	Polytetra Fluro Ethylene
p-value	Probability Value
PVD	Physical Vapor Deposition
rpm	Rotations per minute
SAI	Servicio General de Apoyo a la Investigación
SBF	Simulated Body Fluids
SDGs	Sustainable Development Goals
SEM	Scanning Electron Microscope
SrRan	Strontium Ranelate

UV	Ultraviolet
WHO	World Health Organization
XPS	X-Ray Photoelectron Spectroscopy
XRD	X-Ray Diffraction
YLD	Years Lived with Disability
YSZ	Yttria-stabilized zirconia

Chemical symbols

$(NH_4)_3HPO_4$	Ammonium phosphate
Ag	Silver
Ag^+	Silver Ion
Al	Aluminum
Al_2O_3	Aluminum Oxide
Al^{3+}	Aluminum Ion
$BaSO_4$	Barium Sulfate
Ca	Calcium
Ca^{2+}	Calcium Ion
$Ca_2Ta_2O_7$	Calcium Tantalate
$CaCO_3$	Calcium Carbonate
CaO	Calcium Oxide
CaP	Calcium Phosphate
$CaTa_2O_6$	Calcium Ditantalate
Cl	Chlorine
CO_2	Carbon Dioxide
CO_3^{2-}	Carbonate Ion
Cu	Copper
Cu^+	Copper I Ion
Cu^{2+}	Copper II Ion
c-ZrO_2	Zirconium Dioxide Cubic phase
F^-	Fluoride Ion
F	Fluorine
Fe	Iron
Fe^{2+}	Iron II Ion
Fe^{3+}	Iron III Ion
H_2O	Water
K	Potassium
K^+	Potassium Ion
K_2O	Potassium Oxide
KOH	Potassium Hydroxide
Li	Lithium
Li^+	Lithium Ion
Mg	Magnesium
Mg^{2+}	Magnesium Ion
MgO	Magnesium Oxide
Mn	Manganese
Mn^{2+}	Manganese Ion
m-ZrO_2	Zirconium Dioxide Monocycle phase

Na	Sodium
Na^{+}	Sodium Ion
Na_2O	Sodium Oxide
$NaHCO_3$	Sodium Bicarbonate
NaOH	Sodium Hydroxide
Nb	Niobium
Ni	Nickel
P	Phosphorous
P_2O_5	Phosphorus Pentoxide
$P_2O_7^{4-}$	Diphosphate
P^{3-}	Phosphorous Ion
Sc_2O_3	Scandium Oxide III
Si	Silicon
Si^{4+}	Silicon Ion
SiO_2	Silicon Dioxide
Sr	Strontium
Sr^{2+}	Strontium Ion
$SrCO_3$	Strontium Carbonate
Ta	Tantalum
Ta_2O_5	Tantalum Oxide
Ta^{5+}	Tantalum Ion
TCP	Tricalcium Phosphate
Ti	Titanium
TiC	Titanium Carbide
TiCN	Titanium Carbon Nitrite
TiN	Titanium Nitride
TiO_2	Titanium Oxide (titania, rutile)
t-ZrO_2	Zirconium Dioxide Tetragonal phase
Y	Yttrium
Y_2O_3	Yttrium Oxide
Y^{3+}	Yttrium Ion
Zn	Zinc
Zn^{2+}	Zinc Ion
ZnO	Zinc Oxide
Zr	Zirconia
Zr^{4+}	Zirconium Ion
ZrO_2	Zirconium Dioxide (zirconia)
α'-TCP	Tricalcium Phosphate Alfa' Phase
α-Al_2O_3	Aluminum Oxide Alfa phase
α-TCP	Tricalcium Phosphate Alfa phase
α-Ti	Titanium Alfa phase

α-β-Ti	Titanium Alfa, Beta phase
β-TCP	Tricalcium Phosphate Beta phase
β-Ti	Titanium Beta phase

Equation Symbols

A_w	Water absorption
d	Average length of the two diagonals of the indentation
D	Diameter
D_f	Final Diameter
d_{hkl}	Distance between crystal planes with Miller indices
D_i	Initial diameter
D_s	Diametral shrinkage
F	Force/load
m	Weibull modulus
M_d	Dry mass
M_i	Immersed mass
M_s	Saturated mass
N	Number of specimens tested
n	Order of diffraction
n	Rank of the specimens in ascending order of failure stress
P_a	Apparent porosity
P_f	Cumulative probability of failure at the stress
t	Thickness
wt%	Percentage by weight
Θ	Angle of incident radiation
λ	Wavelength of the incident radiation
ρ_a	Apparent density
ρ_r	Relative density
ρ_t	Theoretical density
σ_o	Weibull characteristic strength
σ_s	Ultimate strength

International System of Units / Accepted units

µl	Microliter
µm	Micrometer
cm^3	Cubic centimeter
g	Gram
kcal	Kilocalories
kgf	Kilogram-force
kV	Kilovolt
m^3	Cubic meter
mg	Milligram
min	Minute
ml	Milliliter
mm	Millimeter
mM	Millimolar
mmol	Millimole
mol	Mole
MPa	Megapascal
MΩ	Megaohm
N	Newtons
nm	Nanometer
^oC	Degree Celsius
u	Atomic mass
v	Volume

1. Introduction

In this introductory chapter the general perspective of the study involving the dissertation is given. Sub-chapters like the framework, motivation, objectives/work plan will be talked about in this chapter.

1.1. Framework

Since the dawn of time, humanity has relentlessly sought the evolution of new methodologies, aiming to meet demands, and overcome emerging challenges in various areas. In bone regeneration, it is widely recognized that the inherent complexities in this domain are significant. Therefore, it is crucial to identify viable alternatives that promote well-being and contribute to a healthy existence.

The life expectancy of humans has experienced an increase, resulting in the aging of the global population. The older demographic faces significant health challenges, with a substantial proportion of these adversities associated with joint conditions and bone tissue, exemplified by aliments such as osteoarthritis and osteoporosis [1, 2]. These pathologies lead to the deterioration of joint cartilage and a reduction in bone mineral density, resulting in a more porous bone structure and, consequently, more susceptible to fragilities. In other words, it becomes more prone to fractures and tumors, affecting both cartilage and bone tissue [1-3]. Globally, a prevalence of musculoskeletal disorders of approximately 21.5 thousand cases per 100 thousand people was observed in 2021. In contrast, Portugal recorded a higher incidence, ranging 35.0 thousand cases per 100 thousand people in the same year [4], as illustrated in Figure 1a. Furthermore, globally, approximately 1.9 thousand per 100 thousand individuals lived with these disorders throughout the year, measured in Years Lived with Disability (YLD's). In Portugal, this number was approximately 3.4 thousand per 100 thousand individuals [4], as represented in Figure 1 b), (both figures can be seen in more detailed in the appendix).

Bone tissue possesses intrinsic regenerative capacity; however, it is limited by the size of the injury. Bone defects of considerable extent, resulting from traumas, infections, neoplasms, and developmental anomalies, are unable to regenerate spontaneously. This limitation poses a significant challenge in the fields of medicine and dentistry [5]. Faced with this limitation, there is an imperative need to seek alternatives capable of overcoming this challenge. In this context, the concept of biomaterial emerges, characterized as a material, whether of natural or synthetic origin, intended to interact with biological systems either temporarily or permanently. The purpose of this material is to assess, treat, enhance, or replace tissue, organ, or function, aiming to improve or maintain the patient's quality of life [6].

Although metals, such as titanium, are widely used in orthopedic and dental applications due to their mechanical strength, ductility, toughness, biological compatibility, durability, and relative

weight, they also pose significant challenges, such as corrosion, wear, and adverse tissue reactions [7-9]. To address these challenges, bioceramics materials have received considerable attention regarding their incorporation into clinical practice [8-10].

Despite the majority of bioceramics historically being inert by nature, active bioceramics, with a composition close to that of bone, have gained prominence due to their remarkable biocompatibility and the ability to establish a robust interface with the prosthesis [8]. Calcium phosphate-based ceramics, such as hydroxyapatite (HA) and TCP, are among the most investigated and utilized [11, 12]. The primary characteristic of calcium phosphate lies in their natural bioabsorption and bioactivity, dynamic attributes closely associated with biological factors [13]. However, when bioceramics are employed in living tissues, they not only need compatibility with the biological environment but also must demonstrate the ability to withstand complex stresses at the application site [14, 15]. When this capacity is not met, there arises a need to develop means that enhance their mechanical properties.

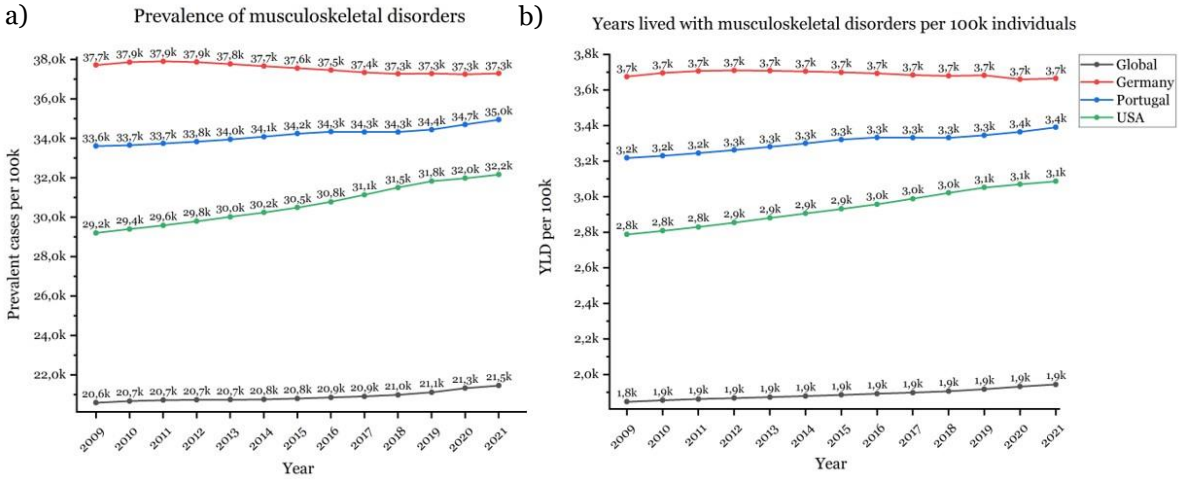

Figure 1. a) Medium of prevalence of musculoskeletal disorders per 100 thousand individuals; **b)** Medium of years lived with musculoskeletal disorders per 100 thousand individuals (Adapted from [4]).

In alignment with the United Nations Sustainable Development Goals (SDGs), this dissertation contributes to fostering progress in the areas of **health and quality (3)** and **quality of education (4)**, supporting the global commitment towards promoting the well-being to all and giving the knowledge to reach that.

1.2. Motivation

Ceramics based on calcium phosphate, such as HA and β-TCP, have been widely advocated as raw materials for bone substitutes, as well as coatings for metallic alloys used in dental and orthopedic implants. Their advantages as ceramic biomaterials stem from their similarity to bone mineral tissue, osteoconductive and osteoinductive behavior, bioabsorption capability, and high thermodynamic stability under physiological conditions (temperature, pH, exposure to body fluids, etc.). However, despite their considerable biocompatibility with living tissues, these bioceramics exhibit low mechanical strength and high fragility.

The inclusion of tantalum (Ta^{5+}) promotes the formation of an apatite layer, enhancing bioactivity and corrosion resistance due to the development of a bilayer structure. Additionally, osseointegration is favored with the addition of strontium ions (Sr^{+2}), contributing to the formation of dense new bone.

1.3. Objectives

Fabrication and characterization of doped TCP with Ta and Sr as additives.

Methodology

- Literature review. Understand the importance, advantages, and limitations of bioceramics, particularly those based on calcium phosphates. In what context they are used in the biomedical field, what type of experimental characterization is common in both mechanical and biological evaluation. Examples of important topics: Bioceramics applications; bone and dental substitutes; coating of metal alloys.

Challenges:
The role of HA and TCP in osteoconductive and osteoinductive behavior and in bioresorption behavior; The effect of tantalum and Sr addition:
Sr is the element that facilitates the growth of new bone tissue (so it enhances osteoinduction) but also it reduces bone resorption. *In vitro,* studies indicate that the presence of Sr increases the number of osteoblasts and reduces the number and activity of osteoclast cells. The doping with Ta was rather poorly studied. It was already proven that Ta promotes osseointegration and shows antibacterial properties, but it was with bioglass as the main material. Considering this, TCP will be doped with tantalum and strontium to study and evaluate their previously described properties.

- Fabrication of samples – Using solid reaction sinterization to obtain bioactive ceramics of doped TCP with two additives to obtain the compositions:

-TCP with 3 wt.% of pure tantalum (Ta);
-TCP with 3 wt.% of strontium (Sr);
-TCP with a combination of 1.5 wt.% of Ta and 1.5% Sr.
Type of samples: cylindric pieces, and film coating on titanium substrates.

- Experimental characterization. Extensive characterization will be performed, namely, the microstructure analysis (XRD, and SEM), evaluation of the density, porosity, mechanical strength and biological behavior.

Mechanical evaluation – Department of Electromechanical Engineering (DEM)/C-MAST
Biological evaluation – Faculty of health sciences (FCS)/CICS to examine cytocompatibility of the compositions with human osteoblast cell line (hOB).

- Write of the dissertation – The dissertation will be written gradually using the approved template. Regular meetings between the supervisors and the student are also intended to analyze the progress of the writing of the document.

1.4. Dissertation organization

This dissertation is structured to provide a comprehensive understanding of the research conducted on the fabrication and characterization of TCP doped with Ta and Sr. The organization of the chapters is designed to guide the reader through the theoretical background, methodology, results, and conclusions drawn from the study.

Chapter 1: Introduction

The introductory chapter outlines the framework of the study, including the motivation behind the research, the objectives, and the work plan. It sets the stage for the subsequent chapters by highlighting the significance of the research in the field of biomedical applications.

Chapter 2: Literature Review

This chapter reviews existing literature related to metals/metal-alloys, bioceramics, Ions used for doping, the influence of porosity in bioceramics, and the surface treatment of a substrate (in this case titanium). It discusses previous studies, identifies gaps in the current knowledge, and establishes the theoretical foundation for the research. Key concepts and definitions relevant to the study are also presented.

Chapter 3: Materials and methodology

In this chapter, the research materials and methodology employed in the study are detailed. It includes descriptions of the materials, experimental procedures, and analytical techniques used to gather and analyze data.

Chapter 4: Results and Discussion

This chapter presents and analyzes the findings from the experimental work. It systematically examines the physical, mechanical, and biological properties of the synthesized bioceramics. The results are discussed in relation to existing literature, interpreting their implications for the development of bioceramics.

Chapter 5: Proof of concept

In this chapter, the bioceramic coating on a titanium substrate is described and analyzed. The focus is on examining the surface morphology of the coating through SEM images to evaluate its quality and uniformity. The results are discussed in relation to their potential impact on the coating's performance. Additionally, challenges encountered during the coating process are highlighted.

Chapter 6: Final remarks

This chapter presents the main conclusions drawn from the study and reflects on the key findings. The results are summarized in relation to the initial objectives, highlighting the significance and potential applications of the developed bioceramic coating. Furthermore, future perspectives are discussed, focusing on possible improvements to the fabrication process and additional research that could expand the understanding and use of this material in biomedical applications.

References

A comprehensive list of all sources cited throughout the dissertation is provided in this section, adhering to the appropriate academic reference style.

Appendices

Any supplementary material, such as raw data, or additional figures, is included in the appendices for reference.

2. State of the art

In this state-of-the-art chapter, the diverse landscape of materials utilized in biomedical applications will be explored. The exploration encompasses an in-depth examination of metals, bioceramics, and the pre-treatment of substrates, with a specific focus on metals, providing a comprehensive understanding of their significance and applications.

2.1. Metals

As talked in the framework, with the need to improve the health and wellbeing of humankind, biomaterials started to emerge to assess, treat, enhance, or replace. One of those types of biomaterials are biometals.

The most commonly metals used in orthopedics and dentistry devices are alloys, given that pure metals do not have sufficient mechanical properties to resist the mechanical strains acting on bones [16, 17]. Pure metals, like platinum, copper or gold are used mostly in dentistry, and others like lead are highly toxic [17]. From all the alloys, there are a big three that have seen widespread adoption for application within the body, the stainless steel, cobalt-based and titanium [18].

Stainless steel is commonly used to prepare orthopedic devices. The most common has a carbon content of 0.03% and is referred as 316 L (L for low carbon content)[16, 17]. This alloy contains 60-65 wt% of iron, 17-20 wt% of chromium, and 12-17 wt% of nickel. Traces of molybdenum, phosphorus, silicon, manganese sulfur or nitrogen can also be found. The low carbon content provides interesting properties with an improve corrosion resistance [16, 17]. Stainless steels are used in surgical instrumentation, but also, importantly, in medical devices, including screws, rods, and plates for bone fixation and spinal fusion devices, mostly because of its good mechanical resistance properties and relative plasticity [18, 19].

Cobalt-based alloys are mainly used for arthroplasty devices. The most famous cobalt alloy is the Vitallium®, containing cobalt, chromium, and molybdenum [16, 17]. Co-Cr alloys are used for their mechanical resistance and good biocompatibility [17]. It is one of the most wear resistant alloys known and has been used for decades in total joint applications [18].

Titanium is never pure but always passivated by a thin Ti oxide layer, the “commercially pure” titanium is referred as CP Ti [16, 17]. Titanium has a principal alloy designated Ti-6Al-4V and it’s used in dental implants as well as total joint replacements among other applications [18]. This alloy has high strength, low elastic modulus, and is particularly good at interfacing with the biological system. Bone ingrowth into porous titanium surfaces, known as biological fixation, is a primary means by which orthopedic implants affix to bone directly [18].

As previously mentioned, a key requirement for a metal to serve as an implant is its biocompatibility. Within the realm of biocompatibility lies a crucial inquiry: how does the device

or material convey its structural composition to guide or impact the reaction of proteins, cells, and organisms towards it [18]? Factors such as cytotoxicity, genotoxicity, mutagenicity, carcinogenicity, allergenicity, and neurological effects must all be carefully assessed, alongside considerations of corrosion tendencies, when evaluating the biocompatibility of metallic biomaterials [20]. In the study referenced as [21], researchers conducted an *in vitro* comparison of metal release from different metallic biomaterials, including stainless steel, Co-Cr alloy, and titanium alloy. Their findings revealed that stainless steel and Co-Cr alloy implants released ions of nickel (Ni), cobalt (Co), chromium (Cr), and iron (Fe) into the physiological environment. Nickel and cobalt are associated with significant concerns regarding carcinogenic effects [22]. Furthermore, chromium and iron are not listed among the biocompatible elements [20]. Metal materials can provoke allergic reactions because of ion release [23]. Figures 2a) and 2b) depict allergic reactions in patients to the nickel content found in stainless steel materials. In both instances, the allergic reactions are triggered by the implant but typically subside shortly after its removal or replacement with a titanium alloy implant [24].

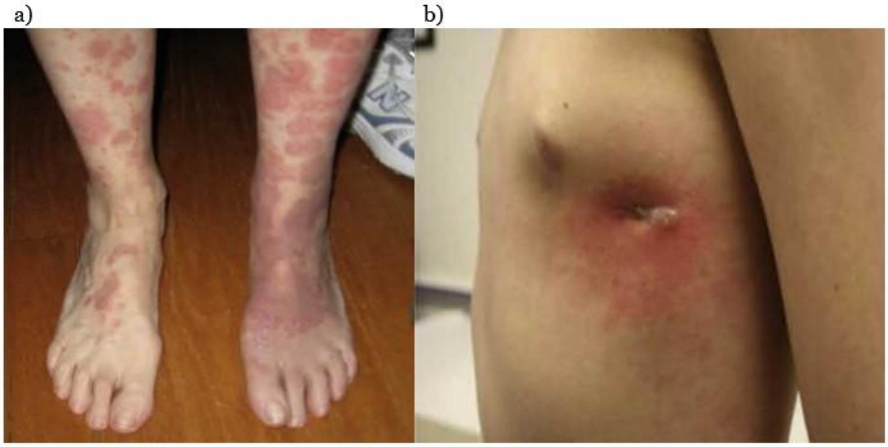

Figure 2. a) Nickel allergy reaction following implantation of stainless steel screws in bunion surgery; **b)** Metal allergy in a patient because of the use of stainless steel bars in pectus excavatum correction surgery, (Adapted from [18]).

Despite Co-Cr alloys exhibiting superior wear and corrosion resistance compared to stainless steel alloys, some contain high levels of nickel (Ni) [18]. Additionally, cobalt (Co) and chromium (Cr) pose potential concerns, with instances of metal allergies observed in patients even when the alloy contains less than 1% Ni [25].

Titanium alloys are categorized as α-, α+β-, and β-type alloys based on their room temperature microstructures [26]. The strength of α-type alloys does not increase with heat treatment, as they maintain stability at room temperature, a fundamental property distinguishing them from α+β- and β-type alloys [26]. Furthermore, β-type alloys offer superior cold-forming ability compared to α-β-type alloys [26], leading to reduced production costs associated with their use [27].

As previously mentioned, titanium alloys exhibit favorable biocompatibility characteristics due to their protective surface oxide layer [18]. These alloys have been favored to mitigate adverse tissue reactions such as necrosis post-implantation. However, one challenge with this class of alloys is the potential formation of fibrous tissue at the bone/implant interface, which may result in implant loosening due to the increased compliance of the fibrous tissue [28, 29]. Moreover, this fibrous tissue can impede bone growth by isolating the implant from the surrounding bone tissue [18]. Strategies to minimize fibrous tissue formation include preventing excessive micromotion of the implant and promoting osseointegration, such as by applying a bone-like apatite layer directly onto the implant surface to facilitate bonding with the surrounding bone tissue [18].

Further discussion on methods to enhance bonding between implants and bone, such as alkali heat treatment, acidic procedures, anodic oxidation, hydrogen peroxide, plasma spray, sandblasting, and sol-gel techniques, will be provided later in the dissertation.

The corrosion resistance of implants is a crucial consideration. When corrosion and the dissolution of surface films occur, metal ions are released from the implants into the physiological environment. This extensive release of metal ions can trigger adverse biological reactions, potentially leading to complete implant failure [20]. Research has shown that the corrosion resistance of metals can be enhanced through anodic oxidation using electrochemical techniques. This enhancement is primarily attributed to the formation of stable, adherent, and protective oxide films on the surface during the anodization process [18].

Despite the formation of an oxide layer on the metal substrate and its ability to self-heal when damaged, small amounts of titanium may still be detected in tissues adjacent to implant prostheses [18]. The incorporation of alloying elements such as niobium (Nb), zirconium (Zr), and tantalum (Ta) into titanium alloys improves their corrosion resistance by stabilizing the surface oxide films [30].

2.2. Bioceramics

As previously indicated, one strategy for mitigating the formation of fibrous tissue involves the incorporation of a bone-like apatite layer onto the implant surface. Bioceramics have emerged as a fascinating subset of ceramics specifically engineered for the repair or replacement of diseased or damaged components within the musculoskeletal system. This category of materials has evolved to encompass three distinct classifications: inert bioceramics, renowned for their robustness, particularly in terms of compression and wear resistance; active bioceramics, which establish direct chemical bonds with bone or soft tissue within living organisms; and resorbable bioceramics, which actively engage in the metabolic processes of the organism [13, 31]. Notably, aluminum oxide (Al_2O_3) and zirconium dioxide (ZrO_2) are acknowledged for their bioinert properties [2, 13]. Conversely, HA, TCP, and select bioactive glasses are considered bioactive and demonstrate bioresorbable characteristics [2, 13, 31, 32]. Through numerous *in vitro* and *in vivo* assessments, bioceramics have gained recognition within the medical community as a viable class

of materials for biomedical applications, particularly in the realm of orthopedic and dental implants [13]. Table 1 illustrates various biomedical applications of bioceramics, encompassing procedures such as knee, tooth, and hip replacements, correction of chronic spinal curvature, treatment of congenital deformities, and mandibular reconstruction.

Table 1. Biomedical applications of bioceramics, (Adapted from [13]).

Devices	Function	Biomaterial
Artificial total hip, knee, shoulder, elbow, wrist	Rebuild arthritic or fractured joints	High density Al_2O_3, metal bioglass coatings
Bone plates, screws, wires	Repair fractures	Bioglass-metal fiber composite, polysulfone-carbon fiber composite
Intramedullary nails	Align fractures	Bioglass-metal fiber composite, polysulfone-carbon fiber composite
Permanently implanted artificial limbs	Replace missing extremities	Bioglass-metal fiber composite, polysulfone-carbon fiber composite
Harrington rods	Correct chronic spinal curvature	Bioglass-metal fiber composite, polysulfone-carbon fiber composite
Vertebrae Spacers and extensors	Correct congenital deformity	Al_2O_3
Spinal fusion	Immobilize vertebrae to protect spinal cord	Bioglass
Alveolar bone replacements, mandibular reconstruction	Restore the alveolar ridge to improve denture fit	Polytetra fluro ethylene (PTFE) – carbon composite, Porous Al_2O_3, bioglass, dense-apatite
End osseous tooth replacement implants	Replace diseased, damaged, or loosened teeth	Al_2O_3, bioglass, dense HA, vitreous carbon
Orthodontic anchors	Provide posts for stress application required to change deformities	Bioglass-coated Al_2O_3, bioglass coated vitallium

2.2.1. Inert bioceramics

Inert bioceramics, by virtue of their inability to form biochemical bonds with surrounding tissues, offer significant advantages in biomedical applications as they do not trigger reactions within the organism. Their paramount characteristic lies in their ability to maintain their properties throughout their duration within the body. This longevity is attributed to their versatility, which allows them to be utilized across a wide range of medical conditions without age restrictions. Their exceptional biocompatibility makes them especially valuable in scenarios involving patients with weakened immune systems and in pediatric treatment [31].

ZrO_2 stands as a prime example of inert bioceramics. It's extensively studied and applied across various fields due to its diverse array of physical, chemical, and mechanical characteristics. These encompass remarkable compressive strength, resistance to wear and corrosion, notable hardness, and an elasticity modulus comparable to steel. With a thermal expansion coefficient like iron and exceptional fracture toughness, ZrO_2 maintains stability even in physiological environments. These traits render invaluable for crafting orthopedic and dental prostheses [2, 33]. Moreover, under different temperature conditions, ZrO_2 can exhibit various polymorphic phases, including cubic, tetragonal, or monoclinic structures [34], as presented in Figure 3.

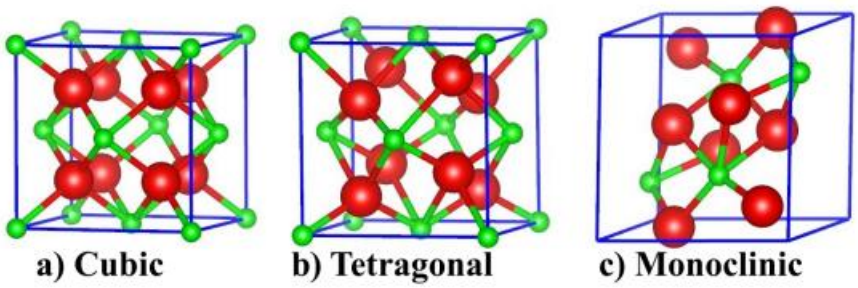

Figure 3. Schematic representation of the unit cells of the crystalline phases of ZrO2: **a)** cubic; **b)** tetragonal; **c)** monoclinic (Adapted from [35]).

At standard room temperature and in its pure form, ZrO_2 adopts a monoclinic crystal structure, maintaining stability until reaching 1170°C. Beyond this threshold, it undergoes a transition to a tetragonal structure, which remains stable until 2370°C. Above this temperature, it transforms into a cubic phase [33, 34]. Depending on the temperature conditions, one can observe the presence of m-ZrO_2, t-ZrO_2, and/or c-ZrO_2. The tetragonal and cubic phases offer superior mechanical, thermal, and optical properties compared to the monoclinic phase, particularly in terms of toughness and fracture resistance [36].

m-ZrO_2 isn't ideal for high-temperature uses as it expands in volume during the transition from t-ZrO_2 to m-ZrO_2, called martensitic transformation [34, 36, 37]. This expansion, around 4.5% upon cooling, negatively impacts ZrO_2's mechanical properties, causing stress-induced crack

formation [34, 37]. To prevent this transformation, the high-temperature phases of ZrO_2 need to be stabilized at room temperature. This stabilization involves adding substances like magnesium oxide (MgO), yttrium oxide (Y_2O_3), calcium oxide (CaO), and scandium oxide III (Sc_2O_3), resulting in partially stabilized zirconia [34, 36, 38]. Y_2O_3 is highly efficient in stabilizing ZrO_2 and improving its toughness, which is why it's widely used as a stabilizer [38, 39]. By replacing some Zr^{+4} atoms with Y^{+3} atoms, Y_2O_3 stabilizes the polymorphic changes in ZrO_2 at high temperatures, preventing volume fluctuations during phase transitions [40]. When ZrO_2 is stabilized with Y_2O_3, it's known as yttria-stabilized zirconia [38].

α-Al_2O_3, recognized for its exceptional density and purity surpassing 99.5%, was among the earliest bioceramics widely employed in clinical applications [39]. It boasts a range of characteristics such as biocompatibility, substantial resistance to wear and corrosion, chemical inertness, and remarkable hardness, rendering it particularly suitable for use in bone and dental implants [13, 41]. The mechanical properties of Al_2O_3, such as flexural strength and compressive strength, are affected by grain size, with smaller grain sizes demonstrating better mechanical performance [41]. Various studies have demonstrated the biocompatibility of Al_2O_3, showing minimal rejection and tissue growth around implanted materials in animal models [13, 42].

2.2.2. Active bioceramics

Has previously mentioned, Active bioceramics can bond with surrounding tissue and gradually degrade as new tissue develops [43].

Materials derived from calcium phosphate have attracted considerable attention in scientific circles due to their chemical similarity to bone mineral, table 2, the inorganic component of bone tissue [11]. These materials offer the potential to replace and regenerate damaged bone tissue [13]. Calcium phosphate ceramics, notably HA and TCP, find applications in various biomedical fields, including injectable bone cements, coatings for metallic prostheses to promote bone growth, solid components for bone repair, orthopedic and dental implants, structures facilitating bone regeneration, and as carriers for controlled drug delivery [43-45].

The key characteristics of calcium phosphates are their ability to be absorbed by the body and their bioactivity, both inherent traits of these materials. These features are largely dynamic and heavily influenced by biological factors. Upon contact with living tissues, these biomaterials initiate various interactions [13].

Table 2. Chemical composition of the bone (Adapted from [8]).

Element	Ca^{2+}	P^{3+}	Na^{+}	Mg^{2+}	K^{+}	F^{-}	Cl^{-}	CO_3^{2-}	$P_2O_7^{4-}$	H_2O	Sr^{2+}, Zn^{2+}, …
wt%	34.8	15.2	0.9	0.72	0.03	0.03	0.13	7.4	0.07	10	Traces

HA and TCP, having a solubility product lower than the ionic product of calcium phosphates in bodily fluids, prompt the formation of a calcium phosphate apatite layer on their surface from ions present in these fluids. This process begins with interaction with collagen, followed by the accumulation of proteins and cells on the material's surface, leading to material reabsorption and bone tissue formation. The crystal composition plays a crucial role, with a typically observed correlation between biomaterial reabsorption and solubility. Unlike bone minerals, which have small crystals but large surface areas, calcium phosphate-based biomaterials have reduced surface areas but strong crystal bonds [13]. The phenomenon of reabsorption is believed to arise from two separate processes: the disintegration of particles into crystals and the dissolution of the crystals themselves. During the dissolution phase, cellular activity is crucial; however, certain insoluble calcium phosphates, like apatite or calcium pyrophosphates, are not readily cleared by cells. The bioresorption of calcium phosphates varies due to disparities in breakdown rates, influenced by biomaterial properties and the strength of crystal-to-crystal bonds [13].

Bioceramics made from calcium phosphates can attract osteoblasts and osteoclasts, a phenomenon referred to as chemotaxis. This process involves mediators found in the bone matrix or bone fluid, which impact bone resorption or formation. It's believed that the initial step in this process is the adsorption of mediators onto the mineral surface. Several factors, including surface charge, microporosity, composition, and molecular composition variations, can affect this adsorption process [13].

Another type of active bioceramics, known as 45S5 bioactive glasses, also exhibit bioresorbable properties and can find numerous applications in the biomedical domain [31].

Baino et *al.* [46] created macroporous scaffolds that mimic bone structure, using a silicate bioactive glass called CEL2 as the primary material. The glass composition consists of 45% SiO_2, 3% P_2O_5, 26% CaO, 7% MgO, 15% Na_2O, and 4% K_2O [46]. Notably, this bioactive glass composition was initially developed by *Vitale-Brovarone* et *al.* [47] at the Polytechnic University of Turin.

The key condition for calcium phosphate-based materials to exhibit bioactivity and adhere to bone is the development of an apatite-like layer on their surface [13].

HA has attracted attention within the scientific community for its resemblance to human bone in terms of chemical composition, its capacity to promote bone growth, and its stability under physiological conditions like temperature, pH, and exposure to bodily fluids. However, its mechanical strength is relatively weak, and it tends to be brittle, which restricts its use in applications requiring higher mechanical stress [1, 5, 15].

Chemically, HA is denoted by $Ca_{10}(PO_4)6(OH)_2$, featuring a Ca/P ratio of 1.67 and possessing a hexagonal structure [13]. When it comes to bone minerals, the Ca/P ratio ranges between 1.37 and 1.87 mol%, suggesting that these minerals may include other ions in their composition, such as strontium (Sr^{2+}), zinc (Zn^{2+}), and carbonate (CO_3^{2-}), has shown in table 2 [48]. The crystal

structures and physical-chemical properties of HA influence its biological performance and can impact the behavior of bone cells. For instance, a rough surface promotes better interaction between the material and cells [49, 50].

TCP is thoroughly researched as a bioceramic and is commonly used in bone cements and implants for its bioactive, osteoinductive, and bioresorbable characteristics [51, 52]. As it can be absorbed by the body, some of the material dissolves, supplying resources for the growth and upkeep of new tissue, thereby aiding in the process of osteoconduction [43, 53].

Chemically, TCP is denoted by $Ca_3(PO_4)_2$ and has a Ca/P ratio of 1.5 [13]. Its structure can vary depending on the temperature: β-TCP remains stable at low temperatures (≤1150 ºC), α-TCP forms at higher temperatures (≈1150-1460 ºC), and α'-TCP remains stable at even higher temperatures (≥1460 ºC) [44, 54].

β-TCP, or β-whitlockite, shows an X-ray diffraction pattern that aligns with a hexagonal crystalline structure [13, 15], while α-TCP exists in the monoclinic phase and is associated with glaserite [44, 55].

The α'-TCP polymorph isn't highly valued in technology because it converts back to α-TCP upon cooling [44]. On the other hand, both β- and α-TCP are extensively researched for low-temperature applications, with α often persisting at room temperature in a metastable state [44, 56]. This irreversible nature poses a primary technological challenge during the consolidation of these bioceramic components, particularly in high-temperature processes [11, 44]. This transition from β to α affects sintering behavior and the final mechanical properties of TCP components. Due to the cell volume increase, the transition results in volumetric expansion (≈7%), which reduces shrinkage and prevents TCP from becoming denser [44, 57].

Monma et al. [58] conducted a study on the transformation from β to α phase in pure TCP. They found that this phase shift follows a first-order kinetics pattern, involving a complete reorganization of the crystal structure with an apparent activation energy of 250 kcal/mol. The reversal from α to β phase is slowed down by cooling, allowing α-TCP to remain in a metastable state even during gradual cooling at 10°C/min. Additionally, they explored the kinetics of α to β reversion during an isothermal hybridization process using pure α-TCP powders. They observed that a peak transformation rate temperature of approximately 870°C facilitates complete reversion within 2 hours. Furthermore, they noted that this transformation could be induced by subjecting the initial α-TCP sample to stress through grinding [44, 58].

The distinct structural characteristics of α- and β-TCP elicit varied biological responses. α-TCP, due to its high solubility at 25°C, is deemed inappropriate for surgical implants and is often utilized in bone cements [44, 54]. Conversely, β-TCP, characterized by its slow degradation, is considered ideal for bone substitutes as it promotes bone growth [15, 43].

2.2.3. TCP doping

Given the characteristics discussed in the preceding sections, it is evident that β-TCP stands out as the most effective bioceramic for bone substitution among the various options. It is crucial to emphasize that while TCP can be used independently, the enhanced properties achieved through doping it with specific metal ions, particularly those found naturally in bone composition as detailed in Table 2, significantly elevate its efficacy in clinical applications.

Many ions have been investigated for their potential to enhance TCP through doping, including magnesium (Mg^{2+}), manganese (Mn^{2+}), zinc (Zn^{2+}), zirconia (Zr^{4+}), iron III (Fe^{3+}), silver (Ag+), lithium (Li^{+}), sodium (Na^{+}), potassium (K^{+}), silicon (Si^{4+}), copper (Cu^{2+}), fluoride (F^{-}), aluminum (Al^{3+}), strontium (Sr^{2+}), and tantalum (Ta^{5+}). Each ion serves different functions, and researchers often combine multiple ions to complement and optimize the final properties of TCP.

Magnesium ions will replace the TCP Ca^{2+} ions, can take the place of TCP Ca^{2+} ions, facilitating the elevation of the β to α phase transformation temperature. This aids in stabilizing β-TCP, enhancing mechanical strength, promoting improved osteoblastic function, and fostering biocompatibility [51, 59-62]. H. S. Ryu *et al.* [63] conducted *in vivo* testing on biphasic components consisting of HA/β-TCP doped with magnesium oxide (MgO), with a Mg^{2+} content of around 9.5 mol%. Their study showed excellent biodegradability without any signs of cytotoxicity or inflammation.

Manganese ions are employed to enhance the mechanical properties and corrosion resistance of TCP, like the role of Magnesium [51, 60]. L. Sinusaite *et al.* [64] conducted a study investigating the impact of manganese (Mn) doping on the synthesis of α- and β-TCP polymorphs. By incorporating Mn ions into the TCP crystal lattice, they observed a reduction in the α- to β-TCP phase transition temperature. The study revealed that Mn doping induced structural modifications in the TCP crystal lattice, resulting in the stabilization of the β-TCP phase at lower temperatures. Furthermore, cytotoxicity tests indicated no adverse effects of Mn ions, even at higher concentrations, suggesting improved biocompatibility of the Mn-doped TCP samples [64].

Zinc ions have improved osteoblast function, corrosion resistance, and conferred bactericidal action [65-68]. K. P. Ananth *et al.* [65] created a bioactive bilayer coating of porous manganese substituted hydroxyapatite on zinc oxide (Mn-HAp/ZnO). The inclusion of zinc led to enhanced mechanical strength, and analysis of leaching showed a decreased rate of metal ion dissolution. Furthermore, *in vitro* bioactivity tests revealed well-defined apatite growth on the coating.

Like the other two ions mentioned earlier, zirconia enhances the mechanical properties of TCP, including strength, toughness, and hardness. Additionally, the presence of zirconia aids in achieving biomimicry with human bone composition [69]. In a study by V. M. Ferro *et al.* [69], the use of zirconia reinforcement, particularly in tetragonal and cubic phases, in TCP composites was investigated. They found that adding zirconia notably enhanced the strength of TCP, leading to a significant increase in mechanical resistance of up to 55%.

The addition of iron ions enhances osseointegration while maintaining the structural stability of TCP [69, 70]. In a study by S. Vahabzadeh *et al.* [70], the effects of iron and its concentration in β-TCP on physicomechanical properties, as well as *in vitro* proliferation and differentiation of osteoblasts, were investigated. The findings revealed that increased iron concentration inhibits the β-TCP to α-TCP phase transformation. Additionally, after 3 days of culture, the samples containing iron were fully covered by osteoblast cells.

Utilizing silver as a dopant offers several advantages, including enhanced antibacterial activity, cell viability, and overall improvements in bone regeneration [71, 72]. M. Mabrouk *et al.* [71], conducted a study with the objective to improve the physicochemical properties, antibacterial activity, and cell viability of biphasic calcium phosphate materials (BCP) by incorporating silver and zirconium. Their research shows that the materials co-doped with silver displayed robust bactericidal effects, enhanced bioactivity properties, and improved cell viability.

Adding lithium, sodium, or potassium as dopants has a positive impact by enhancing thermal stability, structural stabilization, and overall properties [73-75]. Additionally, findings from B. Singh *et al.* [76] indicate that potassium influences physical properties such as ionic conductivity and optical absorption. In a study by N. Matsumoto *et al.* [73], which aimed to evaluate how these dopant ions affect the formation ratio of α-tricalcium phosphate and the rate constant for β–α transformation in β-TCP, it was revealed that the presence of these dopants led to the improvements mentioned earlier.

Silicon plays a crucial role in bone formation, exerting a significant influence [77]. It stimulates cellular activities such as the proliferation and differentiation of osteoblast-like cells, along with mineralization processes [77, 78]. A study conducted by A. Bandyopadhyay et al. [79] explored the effects of co-doping silicon and strontium on the mechanical properties, strength degradation, and *in vitro* interaction with bone cells of TCP. The addition of silicon aimed to customize the degradation properties. The research indicated that co-doping silicon and strontium improved the interaction between cells and the material, influenced apatite growth, and potentially enhanced the mechanical stability of TCP.

Copper, a crucial trace element in human development, contributes to the cross-linking of collagen and elastin in bone formation. It has been noted for its direct stimulatory effect on osteoblastic cells in laboratory settings and is believed to inhibit bone resorption by osteoclasts in living organisms [72]. In a study by N. Matsumoto et al. [80], the co-doping of copper with silver was investigated. The inclusion of copper ions enhanced the antimicrobial properties of TCP, showcasing its potential benefits in combating microbial activity.

Doping TCP with fluoride presents several intriguing advantages. It can stimulate osteoblastic activity [81, 82], delay mineralization (beneficial for improved bone quality, bone growth regulation, enhanced bone healing, and prevention of mineralization disorders), alter mineral-organic interfacial bonding, reduce solubility, and decrease the degradation of calcium

phosphates due to its high resistance to acidity. This enhancement in stability contributes to improved mechanical properties [81, 83]. A study by A. Tahmasebifar and Z. Evis [81] investigated the effects of doping TCP with aluminum and fluoride ions. They found that aluminum doping negatively affected the mechanical properties due to a highly porous structure, while fluoride doping improved them. Co-doping with aluminum and fluoride led to varying effects on microstructure and mechanical characteristics. Similarly, M. Turkoz *et al.* [82] conducted a study but replaced aluminum with silver. In addition to evaluating mechanical properties and microstructure, they assessed the antibacterial activity stemming from silver ions. They discovered that fluoride presence increased microhardness values, and co-doping with aluminum fluoride showed promising results in terms of mechanical strength and antibacterial properties.

In addition to the drawbacks mentioned earlier regarding aluminum doping, there are potential benefits. M. A. Goldberg *et al.* [84] studied the effects of aluminum doping on TCP and observed the formation of a whitlockite-like phase. This phase has implications for enhancing TCP properties and could lead to improved thermal stability and phase composition, offering potential advancements in materials for bone tissue engineering applications.

Strontium, an alkaline earth metal, shares similarities with calcium, allowing it to integrate into the bone's mineral phase [85]. Recent research, both *in vitro* and *in vivo*, has demonstrated the beneficial impact of strontium on bone health. Its presence promotes various aspects of bone formation, including enhanced osteoblast function, bone formation itself, inhibition of bone resorption, increased pre-osteoblast cell proliferation, and collagen synthesis [61, 62, 69, 72, 79, 85, 86]. Strontium Ranelate (SrRan) has been approved for osteoporosis treatment in several European countries since 2004 [85]. However, its usage is restricted due to reported adverse effects like diarrhea, headache, and nausea [87]. Despite these drawbacks, the positive effects of strontium on bone homeostasis suggest its potential to reduce healing periods associated with osseointegrating implants [85].

S. S. Banerjee *et al.* conducted a study [61] examining how combining strontium and magnesium affects both the mechanical and biological aspects of TCP. Their research unveiled several benefits when these ions were used together. These advantages include preventing a transition from β to α phase, enhancing sintered densities, and improving strength compared to the standard TCP. *In vivo* experiments demonstrated superior cell attachment, proliferation, and faster bone formation in doped samples compared to the control. In a subsequent study [62], the same researchers added silicon ions to the existing binary combination. Interestingly, while both the control group and the Sr/Si doped TCP experienced a significant drop in compressive strength, the Mg/Sr/Si doped TCP retained its strength over 16 weeks. Only the Mg/Sr doped TCP showed a gradual decrease in compressive strength, but it still maintained significant strength after 16 weeks. Overall, the addition of silicon did not yield optimal results, with Mg/Sr doped TCP showing the most promising outcomes for bone tissue engineering. Later, the authors replaced magnesium with zinc to investigate its influence on strength degradation and mechanical properties [79]. The

results indicated that samples with Sr/Zn and Sr/Si exhibited the highest weight gain, suggesting good apatite growth. Moreover, the compressive strength of these samples remained relatively constant over an 8-week period. This suggests that depending on the specific element used, the degradation properties of TCP can be tailored accordingly.

Tantalum is also considered a promising candidate due to its excellent corrosion resistance, high fracture toughness, and prominent biocompatibility. Moreover, tantalum demonstrates no remarkable inflammatory response and possesses the ability to support the attachment, growth, and differentiation of osteoblasts [86, 88, 89].

Prior to investigating how tantalum could enhance TCP through doping, it was initially hypothesized that tantalum would not interact in the same way as other ions previously mentioned. This assumption was based on tantalum's larger atomic mass (u) compared to calcium, approximately 180.95 u versus 87.62 u respectively [90], and its higher charge density. Due to these distinctions, it was considered that tantalum would remain isolated within the TCP matrix rather than replacing calcium ions. However, this perspective shifted upon encountering the work of C. Cai et al. [88], their investigation demonstrated that tantalum can indeed replace calcium in TCP. They explored the effects of sintering atmospheres and temperatures on HA/Ta ceramic composites, discovering that tantalum reacts with HA to form $CaTa_2O_6$ and/or $Ca_2Ta_2O_7$ (calcium ditantalate and calcium tantalate, respectively). This formation can be attributed to the diffusion of calcium from HA. Although the possibility of calcium oxide (CaO) from HA decomposition reacting with tantalum oxide (Ta_2O_5) exists, the absence of a CaO pattern in their findings supports the former explanation. Additionally, S. Ligot *et al.* [91] observed that tantalum can substitute calcium in the HA lattice up to concentrations of 4.5%. Beyond this threshold, deviations from the stoichiometric composition were detected, revealing the emergence of unwanted phases.

While these ions offer promising benefits when incorporated into a bioceramic, excessive doses can lead to toxicity [92]. Table 3 outlines each ion mentioned, its respective effects upon addition and the potential consequences when concentration exceeds recommended levels.

Table 3. Effects, safe dose/concentration and symptoms associated with overuse of each ion.

Ions	Effects	Safe dose/concentration	Symptoms
Mg^{2+}	Stabilizes β-phase, enhances mechanical strength, and promotes improved osteoblastic function.	< 1.1 mM [93].	Hypermagnesemia, triggering symptoms like nausea, vomiting, lethargy, headache, flushing, heart defects, progressing to coma, asystole, and ultimately, death [93].
Mn^{2+}	Enhance the mechanical properties and corrosion resistance.	< 5 mg/m^3 [92].	Polycythemia, dystonia, hepatic cirrhosis, and Parkinson's disease [92].
Zn^{2+}	improves osteoblast function, corrosion resistance, and confers bactericidal action.	< 15 mg per day [92, 94].	Cardiovascular, respiratory, renal, and hepatobiliary failure [92, 94].
Zr^{2+}	Enhances the mechanical properties and aids in achieving biomimicry the human bone.	Limited exposure of 5 mg/m^3 over 8-hours, 10 mg/m^3 short term. At 25 mg/m^3 dangerous to life and health [95].	Excessive exposure to zirconium can lead to reactions in the lungs, increasing fibrogenic activity, and in the skin, it may cause granulomatous reactions and/or lesions [96].
$Fe^{2+/3+}$	Enhances osseointegration while maintaining structural stability.	<45 mg per day [97].	Induces osteoblast apoptosis through caspase 3 activation. Reduces the formation of mineralization nodes and hinders the growth of hydroxyapatite crystals. Associated with cirrhosis, liver carcinoma, heart failure, diabetes mellitus, and osteoporosis [92, 94].
Ag^{2+}	Enhanced antibacterial activity, cell viability, and overall improvements in bone regeneration.	lifetime consumption of ≈10g of silver has no adverse effects [98].	Extended exposure to silver compounds can lead to conditions like argyria and argyrosis [98].

Li^{+}	Enhancing thermal stability, structural stabilization, and overall properties.	< 1.5 mmol/L. [99, 100].	Symptoms may include nausea, vomiting, diarrhea, abdominal pain, bloating, delirium, tremors, difficulty with coordination, sudden muscle jerks, speech difficulties (dysarthria), and various other complications [99, 100].
Na^{+}	Enhancing thermal stability, structural stabilization, and overall properties.	<1500 mg/day ca [101].	Development of cardiovascular and chronic kidney diseases, osteoporosis, and cancer [101].
K^{+}	Enhancing thermal stability, structural stabilization, and overall properties.	<5.5 mmol/L [102].	Hyperkalemia, leading to symptoms such as abdominal pain, diarrhea, nausea, vomiting, chest pain, arrhythmia, and numbness in the limbs [102].
Si^{+4}	stimulates cellular activities.	Silicon is considered non-toxic [103, 104].	Inhalation of silicon particles can lead to chronic respiratory effects[103, 104].
$Cu^{+/2+}$	Enhances the antimicrobial properties.	< 1g of copper [94, 105].	Can lead to oxidative stress, Deoxyribonucleic acid (DNA) damage, and decreased cell proliferation. Can cause symptoms such as anemia, convulsions, dementia, organ failure, tremors, and other complications [94, 105].
F^{-}	Stimulates osteoblastic activity, delays mineralization, alters mineral-organic interfacial bonding, reduces solubility, and decreases the degradation of calcium phosphates.	<0.5 to 1 mg/L [106, 107].	Toxic effects, including oxidative stress, cell cycle arrest, and apoptosis, linked to the inhibition of proteins, disruption of organelles, changes in pH, and imbalances in electrolytes [106, 107].

Al^{3+}	formation of a whitlockite-like phase, which improves thermal stability and phase composition.	<100 mg/L [94, 108].	can lead to bone disorders like renal osteodystrophy, osteomalacia, and osteoporosis [94, 108].
Sr^{2+}	Enhances osteoblast function, bone formation itself, inhibits bone resorption, increases pre-osteoblast cell proliferation, and collagen synthesis.	< High doses [109, 110].	It can have negative effects on bone metabolism and mineralization. Oral exposure to high doses of strontium can lead to a condition known as "strontium rickets"[109, 110].
Ta^{5+}	Corrosion resistance, high fracture toughness, prominent biocompatibility, and support the attachment, growth, and differentiation of osteoblasts.	When ingested orally, tantalum is generally considered non-toxic as it is poorly absorbed by the body and quickly eliminated [111].	Inhaling tantalum oxide can lead to temporary bronchitis and interstitial pneumonitis with hyperemia, a condition characterized by inflammation in the lungs [111].

2.2.4. Porous bioceramics

To ensure the effectiveness of bone scaffolds or substitutes, porosity is essential for promoting bone growth within interconnected three-dimensional pores, as well as facilitating cell, tissue infiltration, and capillaries development [112]. A porous or rough surface further enhances functionality by acting as a template for cell attachment and offering temporary support at the defect site [112]. Moreover, the scaffold/substitute must exhibit mechanical properties similar to the native bone [113]. However, balancing porosity with sufficient mechanical strength remains a critical challenge in scaffold/substitute fabrication [112].

Out of the numerous alternative materials suggested for bone reconstruction, polymethyl methacrylate (PMMA) stands out as an ideal choice because of its desirable traits. These include ample strength for mechanical support, adaptability to fill intricate defects, cost-effectiveness, and Food and Drug Administration (FDA) approval [114, 115]. Given these qualities, this polymer has found extensive use as an adhesive in orthopedics, facilitating bonding between bone and implants or addressing bone defects resulting from conditions like osteoporosis or cancer [116, 117]. Its exceptional mechanical properties have also made it indispensable in load-bearing applications such as knee and hip replacement implants[116, 118]. Furthermore, it boasts clean and straightforward thermal removal at high temperatures and significant chemical dissolution with numerous solvents [119].

Nevertheless, it has been determined that PMMA possesses certain unfavorable characteristics. Its polymerization process generates heat, potentially causing thermal harm to nearby tissues [114]. Furthermore, its bioinert nature, lacking bioactivity, can result in fibrosis formation around the implanted biomaterial, hindering proper bone tissue adhesion to the material's surface and leading to eventual material loosening [120]. Additionally, PMMA's transparency makes it difficult to distinguish in X-ray images, rendering the interface between the surrounding bone and the implanted material indiscernible [116].

Consequently, researchers have shown interest in modifying this bone cement [114]. Additives like ZrO_2 or barium sulfate ($BaSO_4$), known for their high radiopacity, are frequently integrated into PMMA bone cements to enhance visibility in imaging. However, these additives exhibit limited osteoconductivity, rendering them less suitable for orthopedic clinical applications [121]. Conversely, in recent years, calcium phosphate ceramics have gained traction due to their outstanding biocompatibility and ability to support bone growth, serving as the primary raw material, with pore-forming agents like PMMA being added [122, 123]. Previous investigations [119] have utilized PMMA to fabricate the polymeric structure, leveraging its spherical form to regulate the dimensions, uniformity, and morphology of the polymer framework.

Implants designed with a gradient of porosity and adequate interconnections can closely mimic the functions and structure of both cortical and spongy bone. Their high porosity supports bone growth, while less dense regions provide load-bearing capabilities comparable to natural bone [119, 124].

The porous structure of the implant promotes osteoconduction, allowing new bone tissue to colonize the material. This creates a stable interface with connective tissues and serves as a scaffold for bone formation. To facilitate vascular and cellular penetration, which supports bone growth within the pores, the implant's porous architecture, including pore size and interconnections, must be precisely controlled [119]. However, most studies indicate that bone tissue growth and cell colonization happen only when macropore size are between 100–200 μm [5, 125, 126], and if the interconnectivity is greater than 50 μm [127].

Earlier research [113] showed that doping calcium phosphate ceramics with PMMA spheres effectively created micropores by removing the spheres, as showed in Figure 4a). The more spheres added, the higher the micropore fraction. High interconnected porosity levels facilitate blood, oxygen, and nutrient supply and promote cell growth, leading to faster bone regeneration [128].

Several synthetic methods can be used to create porous materials, including foam formation [5], the use of porogenic agents [119, 124], slip casting shaping [124], solid-state reactions [129], 3D prototyping [130], starch consolidation [131], burning the organic phase [132], and sponge replication [133].

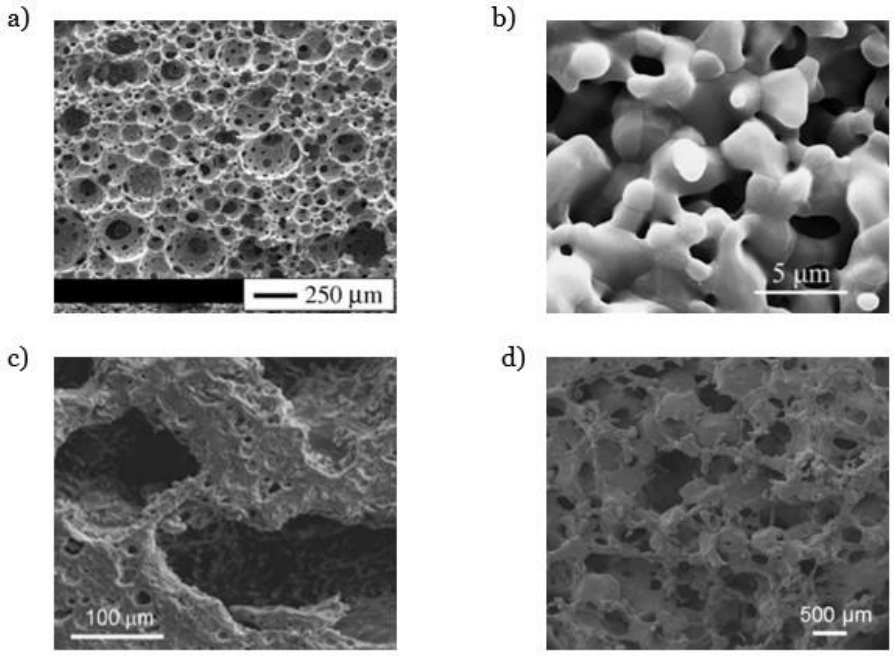

Figure 4. Examples of porous structures formulated using different methods: **a)** porogenic agent, **b)** 3D printing, **c)** burning the organic phase, and **d)** sponge replication. (Adapted from [123, 130, 132, 133], respectively).

2.3. Surface modification of titanium

The long-term performance of surgical implants is often limited by their surface properties. Titanium and its alloys have poor tribological properties, including low wear resistance, which reduces the service life of implants. This issue can largely be addressed by modifying the surface of the substrate [7].

Appropriate surface modification techniques preserve the excellent intrinsic properties of titanium alloys, including high fatigue strength, formability, machinability, and relatively low modulus. Moreover, they enhance the specific surface characteristics required for different clinical applications [134]. These methods include mechanical treatments, chemical processes, oxidation, carburization, ion implantation, and sol-gel techniques [134].

The primary objective of mechanical modification is to create surface roughness and topographies on the implant surface. Generally, mechanical treatments produce rough structures that increase the implant's surface area. This increased surface area is beneficial as it promotes biomineralization. Surface roughness enhances the attachment, proliferation, and differentiation of osteogenic cells, which is crucial for the osseous integration of metallic implants. Techniques for achieving this include machining, grinding, and blasting, with blasting being the most used method [28, 134].

Chemical methods include acid treatment, alkali treatment, oxidation, chemical vapor deposition (CVD), and biochemical modification, sol–gel [28, 134]. Acid treatment is a widely used surface treatment method for cleaning substrate surfaces by removing oxides and contaminants. A solution of mixed acids is often employed for this purpose [134, 135]. Alkali treatment involves a straightforward surface modification using an alkali solution, such as NaOH or KOH, to create a bioactive porous layer on substrate materials [134-136]. Simply put, oxidation is a chemical reaction where a metal interacts with oxygen to form an oxide. The oxidation behavior of a metal depends on various factors, and the reaction mechanism is typically quite complex [134, 137]. Thermal oxidation takes place when metals or alloys are heated in a highly oxidizing environment, such as air or oxygen. It is a cost-effective surface modification technique used to intentionally create a protective oxide layer on titanium alloys. The goal of thermal oxidation is to produce a ceramic coating, primarily focusing on forming a rutile structure [134]. Anodic oxidation is an electrochemical process that involves the diffusion of oxygen and metal ions. In this technique, an electric field drives the metal ions, resulting in the formation of an oxide layer on the surface of the anode [28, 134]. CVD is a process where chemical reactions between gas-phase chemicals and the sample surface result in the deposition of a non-volatile compound on the substrate. Unlike physical vapor deposition (PVD), which uses techniques like evaporation and sputtering without involving chemical reactions, CVD relies on chemical interactions. This method is widely used in the industry to produce organic and inorganic films on metals, semiconductors, and other materials [28]. Biochemical modification of biomaterials leverages biological and biochemical insights into cellular functions, adhesion, differentiation, and remodeling. The goal of this

modification is to induce specific cellular and tissue responses through surface-immobilized peptides, proteins, or growth factors. However, it's crucial that while enhancing the biocompatibility of the surface, the bulk properties of the material remain unaffected. To achieve this, the concept of a bio-mimetic surface has been introduced, which guides cell behavior using an ultrathin layer of bioactive molecules [28].

Sol-gel technology merges two fundamental concepts: sol and gel. A sol constitutes a colloidal suspension where minuscule solid particles are dispersed within a liquid medium, while a gel refers to a material characterized by a continuous solid structure enclosing a liquid phase. The sol-gel process encompasses five key stages [28, 134]:

1. Hydrolysis and polycondensation;
2. Gelation;
3. Aging;
4. Drying;
5. Densification and crystallization.

This technique employs two primary methods [28, 134]:

a. Spin coating technique: Specimens are rotated to evenly distribute the coating solution across the substrate through centrifugal force;
b. Dip coating technique: Specimens are directly immersed or submerged in the solution.

Sol-gel methodology is particularly favored for depositing thin (<10 μm) ceramic coatings [28]. It has emerged as a promising avenue in biomedical applications, capable of generating a variety of coatings such as titanium oxide (TiO_2), calcium phosphate (CaP), and TiO_2-CaP composites [134]. The sol-gel approach yields highly crystalline HA microstructures and superior chemical uniformity due to its capacity to blend calcium and phosphorus precursors at the molecular level. Compared to traditional thin layer oxidation processes, the sol-gel method offers several advantages [134]:

a. Lower densification temperatures;
b. Enhanced control over coating homogeneity, chemical composition, and crystalline structure;
c. Cost-effectiveness and simplified equipment requirements.

Table 4 summarizes all the titanium surface modification methods mentioned earlier, along with some additional methods not previously discussed. Although many other methods exist, the primary focus of this dissertation is not surface modification. Therefore, I have provided a general overview of various techniques and have explained the sol-gel method in more detail, as it will be used in the later stages of this work.

Table 4. Summary of surface modification methods used for titanium and its alloys implants (Adapted from [134]).

	Surface modification methods	Modified layer	Objective
Mechanical methods	Machining	Rough or smooth surface formed by subtraction process	Produce specific surface topographies; clean and roughen surface; improve adhesion in bonding
	Grinding		
	Polishing		
	Blasting		
Chemical methods	Acidic treatment	<10 nm of surface oxide layer	Remove oxide scales and contamination.
	Alkaline treatment	≈1 μm of sodium titanate gel	Improve biocompatibility, bioactivity, or bone conductivity.
	Hydrogen peroxide treatment	≈5 nm of dense inner oxide and porous outer layer	Improve biocompatibility, bioactivity, or bone conductivity.

Chemical methods	Sol-gel	≈10 μm of thin film, such as calcium phosphate, TiO_2 and silica	Improve biocompatibility, bioactivity, or bone conductivity.
	Anodic oxidation	≈10 nm to 40 μm of TiO_2 layer, adsorption, and incorporation of electrolyte anions	Produce specific surface topographies; improved corrosion resistance; improve biocompatibility, bioactivity, or bone conductivity
	CVD	≈1 μm of TiN, TiC, TiCN, diamond and diamond-like carbon thin film	Improve wear resistance, corrosion resistance and blood compatibility
	Biochemical methods	Modification through signalized titania, photochemistry, self-assembled monolayers, protein resistance, etc.	Induce specific cell and tissue response by means of immobilized surface peptides, proteins, or growth factors
Physical methods	Thermal spray	≈30 to 200 μm of coatings, such as titanium, HA, calcium silicate, Al_2O_3, ZrO_2, TiO_2	Improve wear resistance, corrosion resistance, and biological properties
	Flame spray		
	High velocity oxygen fuel (HVOF)		
	Detonation gun (DGUN)		
PVD	Evaporation	≈1 μm of TiN, TiC, TiCN, diamond and diamond-like carbon thin film	Improve wear resistance, corrosion resistance and blood compatibility
	Ion plating		
	Sputtering		

Ion implantation and deposition	Beam-line ion implantation	≈10 nm of surface modified layer and/or ≈µm of thin film	Modify surface composition; improve wear, corrosion resistance, and biocompatibility
	PIII		
	Glow discharge plasma treatment	≈1 nm to ≈100 nm of surface modified layer	Clean, sterilize, oxide, nitride surface; remove native oxide layer

3. Materials and methodology

In this chapter, the feedstock used in this study is introduced, the experimental planning of the mixtures is outlined, and the fabrication process of the bioceramic is described. Additionally, the various characterization methods employed are detailed, covering physical, mechanical, microstructural, and biological aspects. The chapter concludes with a discussion of the techniques used to characterize the properties of interest.

Furthermore, it is worth noting that the study is split into two sections: the first section focuses on creating disc-shaped bioceramic samples, while the second section is dedicated to producing sol-gel bioceramic.

3.1. Materials

3.1.1. Raw materials

As the topic of this dissertation was suggested by the co-adviser, the raw materials are derived from earlier studies [69, 86], and their methodologies will be utilized. This research involves doping TCP with 3wt% tantalum, 3wt% strontium, and a combination of 1.5/1.5wt% tantalum/strontium [86].

To accomplish this, Calcium Carbonate ($CaCO_3$, 98.5-100% pure, from PanReac AppliChem, CAS-No: 471-34-1), Ammonium phosphate, dibasic ($(NH_4)_3HPO_4$, 98% pure, from Thermo Scientific, CAS-No: 7783-28-0), Tantalum powder (Ta, 99.97% pure, from Alfa Aesar, CAS-No: 7440-25-7), and Strontium Carbonate ($SrCO_3$, ≥ 98% pure, from Fisher Chemical, CAS-No: 1633-05-2) were mixed in four different configurations, as detailed in table 5.

Table 5. Composition of each sample.

Samples	TCP (wt%)	Ta (wt%)	Sr (wt%)
Control	100	0	0
Ta 3%	97	3	0
Sr 3%	97	0	3
Ta/Sr 1.5%	97	1.5	1.5

3.1.2. Sample manufacturing

Initially, to enable the production of all the compositions, the various reagents (raw materials) were weighed using an analytical balance (Oertling, maximum capacity 200 g, resolution 0.0001 g). Following this, the reagents were mixed in a zirconia ceramic grinding vessel (Fritsch, maximum capacity 250 ml, Germany) along with 3 mm diameter YSZ (yttria-stabilized zirconia) balls (Fritsch, Germany), and isopropyl alcohol (Labchem, Portugal), this last two components serve to facilitate the mixture process. Each quantity goes by a ratio of 1:1:2 respectively. The grinding was performed using a high-energy ball mill (Fritsch, Pulverisette 6, Germany) at 500 rpm (rotations per minute) for five cycles of 30 minutes each, to prevent overheating of the contents inside the ceramic vessel. After the five cycles, the mixture was dried in an oven (Carbolite, NR200-F, UK) at 80°C for at least 24 hours. Subsequently, the mixture was sieved using various sieves (Filtra Vibración, Spain) with mesh sizes of 212 μm (Serial Number: 235033/1), 106 μm (Serial Number: 235032/1), and 63 μm (Serial Number: 235031/1) with the aid of a sieve shaker (Retsch, AS200, Germany). This process enabled the separation of the YSZ balls and the removal of any impurities and/or agglomerates in the mixture. The procedure described above was repeated four times, one for each composition of table 5.

Accordingly, all the previously sieved powder was placed in crucibles and calcined in an electric furnace (Termolab, MLR, Águeda, Portugal) at 1000°C for at least 10 hours. After calcination, the material was demolded and returned to the ceramic vessel with fresh YSZ balls, then grinded for 1 to 3 minutes at 500 rpm to eliminate any agglomerates formed. Finally, the powder was sieved using the sieve shaker and the same three sieves, and then properly stored.

Following these preparations, the particle size distribution (PSD) of each powder composition was analyzed using the laser diffraction method (Beckman Coulter, LS200, Brea, CA, USA).

To create disc-shaped bioceramics from each composition for later physical, mechanical, microstructural, and biological analysis, uniaxial pressing was utilized. This method involved compacting the mixture in a mold by applying uniaxial pressure with a universal electromechanical testing machine (Shimadzu Corporation, AGS-X, Serial Number: I3307 5130549CS, Japan), exemplified in Figure 6.

Each bioceramic disc, weighing between 0.6 and 0.65 g, with a diameter of approximately 13 mm and a thickness of 3 mm, was produced using a 13 mm diameter stainless steel mold. A uniaxial pressure of 50 MPa was applied for 10 seconds. An analytical balance ensured that all samples had a mass within the 0.6-0.65 g range. These values are based on the work of P. Jonson *et al.* [138], who determined that to ensure plane stress conditions, the ratio between thickness and diameter must be less than or equal to 0.25. They found that a mass between 0.6 to 0.65 g was optimal for achieving the best results. To study the influence of the 0.05 g difference, 15 discs for each composition were made, where 5 presented 0.6 g, 5 with 0.62 g, and the rest with 0.65 g.

J. L. Amorós Albaro [139] recommends a technique for sample formation that involves slightly raising the mold so that only the lower punch remains in contact. This method helps reduce the formation of chips and cracks in the sample. As shown in Figure 5 a), only the lower punch touches the base.

Subsequently, the samples were then sintered in an electric furnace (Termolab, Portugal) with a heating rate of 5°C per minute, starting from room temperature up to 1300°C. They were held at this sintering temperature for 120 minutes. Sintering is defined as a physical and chemical consolidation process where a material attains mechanical strength through atomic diffusion and merging at high temperatures. This process removes the voids between particles, producing a solid and dense structure [140], as illustrated in Figure 6. During sintering, specific thermochemical reactions take place, leading to changes in the material's dimensions. Therefore, a digital caliper (Powerfix Profi, Portugal, resolution: 0.01 mm) was used to measure each sample after the sintering process.

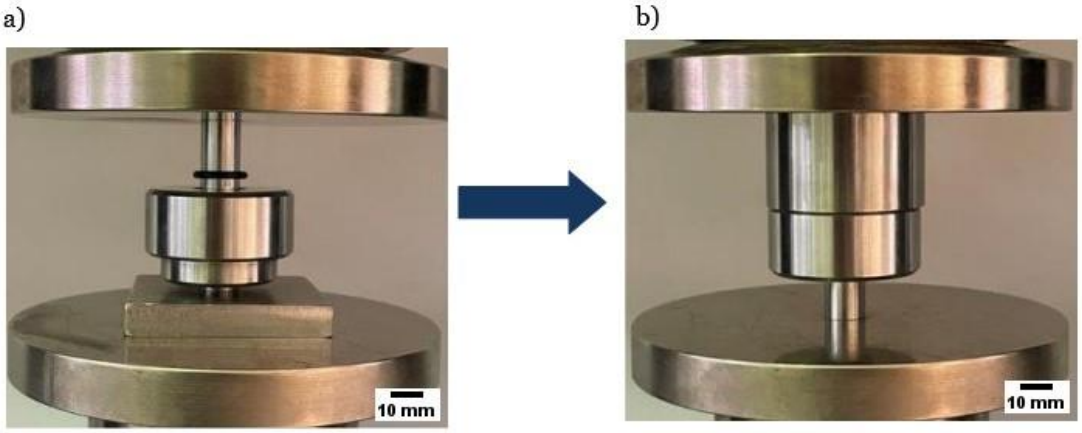

Figure 5. Illustration of the uniaxial pressing process, **a)** initial phase, formation of the disc-shaped sample, and **b)** final phase, removal of the sample from the mold.

Figure 6. Example of samples after the sintering process.

3.2. Physical properties

3.2.1. Diametral shrinkage

Physical and thermochemical reactions during sintering lead to changes in material dimensions. Thus, following ASTM C179-04 [141], diametral shrinkage, D_s, was assessed during sintering using equation (1), where D_f represents the final diameter and D_i the initial diameter, i.e., the mold's diameter.

$$D_s = \frac{D_f - D_i}{D_i} \times 100\% \quad (1)$$

3.2.2. Density, porosity, and water absorption

Porosity contributes to enhanced cellular adhesion on both the surface and within the material, facilitates cell and tissue infiltration, and promotes capillary formation. However, increased porosity can compromise mechanical properties, as high porosity tends to lower material strength. Despite this, highly porous structures offer specific functional advantages over their denser counterparts [112, 113].

Following the protocol outlined in ASTM C20-00 [142], and considering distilled water (1.0 g/cm^3) as medium, it was determined the following physical properties: bulk density, water absorption, and apparent porosity. The Oertling analytical balance was consistently used for all measurements.

After the sintering process, the dry mass of each sample was measured, ensuring no residual water remained inside. Subsequently, the samples were immersed in hot water for 24 hours. Water droplets on their surfaces were removed using paper, and the saturated mass was determined. To measure the immersed mass, the samples were submerged in water with the assistance of a copper wire positioned below the Oertling analytical balance, as depicted in Figure 7.

When materials are submerged, water gradually fills the pores, causing the reading on the balance to stabilize slowly. This measurement approach relies on Archimedes principle, which states that any object immersed in a fluid experience an upward force equal to the weight of the fluid displaced by the object [143]. Consequently, when submerged in a fluid, any object appears to weigh less than its actual weight, a concept referred to as apparent weight.

Figure 7. Illustration of the process for measuring the immersed mass of the sample.

Apparent density or bulk density, ρ_a, was calculated using the ratio of the dry mass, M_d, to the difference between the dry mass and the immersed mass, M_i, as shown in equation (2). This measurement accounts for both the volume of the material and the closed pores, and it is expressed in g/cm^3.

$$\rho_a = \frac{M_d}{M_d - M_i} \tag{2}$$

Water absorption, A_w, was determined using equation (3), which calculates the ratio of the difference between the saturated mass (M_s) and the dry mass to the dry mass. This measurement reflects the amount of water absorbed by the material's open pores, expressed as a percentage of the dry mass.

$$A_w = \frac{M_s - M_d}{M_d} \times 100\% \tag{3}$$

Apparent porosity, P_a, was calculated using equation (4), which involves the ratio of the difference between the saturated mass and the dry mass to the difference between the saturated mass and the immersed mass. This indicates the volume of open pores as a percentage of the total volume of the sample.

$$P_a = \frac{M_s - M_d}{M_s - M_i} \times 100\% \quad (4)$$

The relative density, ρ_r, was also calculated, using equation (5), which represents the ratio between the apparent density and the theoretical density (ρ_t). To calculate the relative density, the theoretical density (3.07 g/cm^3) of the XRD card number of #09–0169 for TCP was considered for all materials. Therefore, the relative density is equal to the ratio between bulk density and theoretical density of the TCP.

$$\rho_r = \frac{\rho_a}{\rho_t} \quad (5)$$

In all tests assessing physical properties, standard deviation was employed to evaluate any deviations or associated errors across the 15 measurements, ensuring a statistically significant sample size.

3.3. Mechanical properties

3.3.1. Ultimate strength test

Research on mechanical strength is highly important, especially for bone substitute applications, because these substitutes must be strong enough to endure the forces experienced during bone healing. Assessing the mechanical properties of brittle materials like ceramics is a challenging task due to their hardness and fragility, which make handling samples difficult [144]. The diametral compression test, or Brazilian test, can be used to measure the mechanical strength of these materials [145].

In the diametral compression test, a disc is compressed by two flat plates along its diameter until it breaks, as illustrated in Figure 8 a). The disc fractures along the diametral plane, resulting in two similar halves [145], as depicted in Figures 8 b), c), d), and e). This compression generates breaking stress perpendicular to the compressed diameter, which remains constant over a significant area near the disc's center [145].

When the material fractures, a decrease in load is seen on the force-displacement curve recorded during the test [138], as shown in Figure 9.

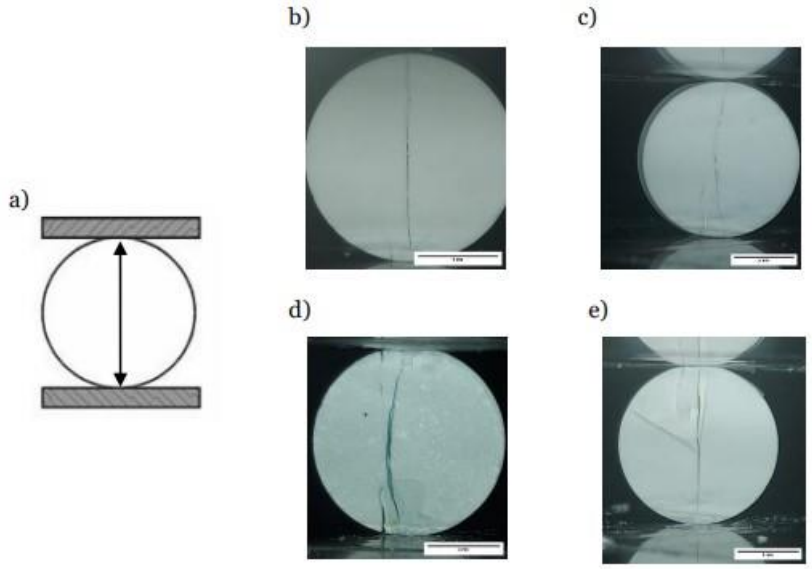

Figure 8. Example of ultimate strength test. **a)** illustration of diametral compression test, the double arrow indicates how the fracture should occur (Adapted from [145]); **b)** appearance of a valid control sample after diametral compression; **c)** appearance of a valid tantalum 3% sample after diametral compression; **d)** appearance of a valid strontium 3% sample after diametral compression; **e)** appearance of valid strontium/tantalum 1.5% sample after diametral compression.

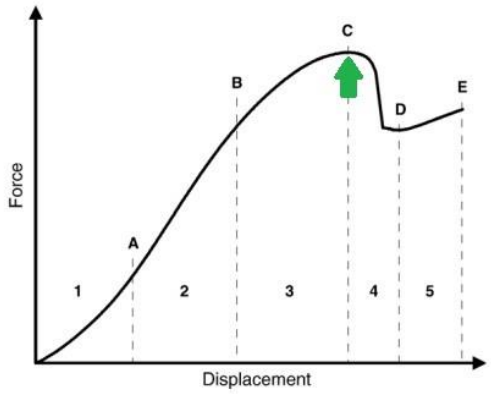

Figure 9. A typical force-displacement curve from the ultimate strength test, where the green arrow indicates the breaking point of ceramics, includes: **1)** a non-linear elastic region, **2)** a linear elastic region, **3)** the start of material fracture, **4)** the maximum force the material can withstand the point of fracture, and **5)** the end of the test, (Adapted from [138]).

Ultimate strength (or breaking stress) is determined by the fact that the break starts at the point of highest tensile stress, located at the center of the disc [138]. When specific conditions are met, the test is considered valid. The ultimate strength, denoted as σ_s, can then be calculated using equation (6). In this equation, P represents the maximum applied force, which is the maximum

stress the sample can endure before breaking; D is the diameter of the sample; and t is the thickness of the cylindrical sample.

$$\sigma_s = \frac{2P}{\pi D t} \tag{6}$$

A universal electromechanical testing machine (Shimadzu Corporation, AGS-X, Serial Number: I3307 5130549CS, Japan) equipped with a 10000 N load cell was used to perform the diametral compression test, operating at a crosshead speed of 0.5 mm/min.

For equation (6) to hold true, it is assumed that the ultimate strength is consistent across most of the diametral plane of the disc, and that failure occurs along this plane, splitting it into two equal parts. Data from fifteen valid tests were used to determine the Weibull parameters according to the ENV-843-5 procedure, which utilizes the simplest form of the Weibull function, given by equation (7).

$$P_f = 1 - exp\left[-\left(\frac{\sigma_s}{\sigma_0}\right)^m\right] \tag{7}$$

Here, P_f represents the cumulative probability of failure at the applied stress σ_s (as defined in equation (6)); σ_o is the characteristic strength, which corresponds to the stress level at which there is a 63.2% probability of failure; and mmm is the Weibull modulus, which describes the material's variability. To calculate the Weibull parameters, the probability of failure was assigned to the experimental values using equation (8):

$$P_f = \frac{n - 0.5}{N} \tag{8}$$

where N is the total number of specimens tested, and n is the rank of the specimens in ascending order of failure stress.

3.3.2. Vickers hardness test

After the ultimate strength test, one half of each composition was selected. These selected samples were embedded in Epofix resin (Struers, Cold setting embedding resin kit, USA). Subsequently, their surfaces were polished with diamond down to 1 μm (Struers, RotoPol-21, USA). The Vickers hardness and toughness were then assessed on the polished surfaces according to ASTM C-1327 standards. Measurements were conducted using a Vickers hardness testing machine (Mitutoyo AVK-C2, Japan) with an applied load of 2.0 kgf (19.62 N) for 10 seconds. Cracks emanating from the indentation vertices, as shown in Figure 10, were used to calculate the fracture toughness [146]. Although the machine provided the Vickers hardness (HV) values, the following equation (9) was utilized to convert it to GPa:

$$HV = 0.0018544\left(\frac{P}{d^2}\right) \tag{9}$$

where P is the applied load and d is the average length of the two diagonals of the indentation. The reported results are the averages of four valid determinations, with errors represented as standard deviations.

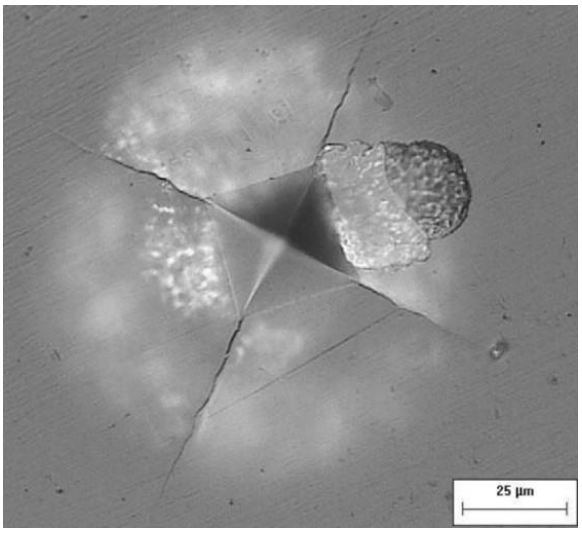

Figure 10. Example of a SEM image taken of a Vickers hardness test (Adapted from [147]).

3.4. Microstructural properties

3.4.1. X-ray diffraction

To verify that the doping reaction occurred, X-ray diffraction (XRD) tests were conducted on the four compositions. For this purpose, some remaining pieces of each composition disc were ground back into powder using a mortar and pestle.

XRD is a versatile, fast, and non-destructive analysis technique primarily used for the quantitative and qualitative analysis of crystalline phases present in a wide variety of samples [148].

When the atoms in a crystalline material like ceramics are irradiated with an X-ray beam at a specific angle, the radiation scatters in all directions. The scattered X-ray waves from different crystal planes interfere with each other, leading to either constructive or destructive interference. Constructive interference increases the wave's intensity, while destructive interference reduces or even eliminates it. Diffraction occurs due to constructive interference of the scattered X-rays. This only happens when Bragg's law is satisfied, which states that the path difference between the two waves diffracted by atoms A and B must be an integer multiple of the wavelength. Bragg's law, expressed in equation (10), links the angle of incident radiation, θ, the distance between crystal planes with Miller indices, d_{hkl}, the wavelength of the incident radiation, λ, and the order of diffraction, n [148]. Figure 11 shows a schematic example of the associated geometry to XRD.

$$n\lambda = AB + BC = 2d_{hkl}sin(\theta) \quad (10)$$

When samples are exposed to X-rays with a specific λ, a diffractogram can be obtained that shows the intensity of the diffracted radiation as a function of the diffraction angle 2θ. At the point of maximum diffraction, where Bragg's law is satisfied, the interplanar distances of the crystalline phases in the sample can be determined. Each crystalline substance has unique interplanar distances, allowing for their identification by comparing these distances with tabulated values [148].

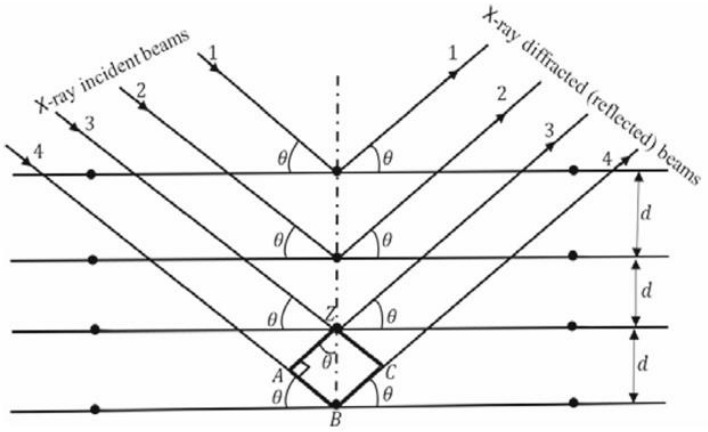

Figure 11. Illustrative example of a XRD geometry (Adapted from [148]).

XRD tests were conducted with an X-ray diffractometer (DMAX III/C, Rigaku, Japan) configured with horizontal Bragg-Brentano geometry ($\theta/2\theta$). The X-ray tube functioned at 40 kV and 30 mA, utilizing CuKα radiation. The X-ray diffracted radiation intensity as a function of the diffraction angle 2θ was measured across a range from 5º to 90º. Diffractograms obtained from this technique were compared against theoretical reference cards available in the ICDD (International Centre for Diffraction Data) database within the MDI/JADE 6 analysis software. Specific references include #04-0788 for Ta, #15-0305 for Sr, #09-0432 for HA, #09-0169 for β-TCP, #09-0348 for α-TCP, and #44-1008 for $Ca_2Ta_2O_7$.

3.4.2. Scanning electron microscope

Scanning electron microscope (SEM) is a highly effective method for examining surfaces and studying their shape, texture, and internal structure. It can reveal details like the size of grains, the presence of pores, and various phases within the material. SEM works by directing a beam of electrons over the sample's surface. The interaction between the electrons and the material generates extensive data, which, when processed, produces highly detailed images of the sample's surface [149].

The samples that were broken during the diametral compression test were examined using SEM to confirm that the fractures were not due to severe local crushing near the areas where the load was applied [1].

Due to the non-conductive nature of the bioceramics, their surface was coated with carbon, and their fracture with platinum using a High-vacuum coating equipment (Leica EM ACE600, Leica Microsystems). Both surface and fracture images of the samples were taken with an ampliation of 500x and 2000x, by a Field Emission Scanning Electron Microscope (FESEM, Carl Zeiss, MERLIN™) with an electron high tension (EHT) of 5 kV.

Moreover, image analysis was performed using the ImageJ software.

3.5. Biological properties

3.5.1. Cytocompatibility tests

Following the procedure from earlier research [1], the same methods were used to assess the biological properties of the bioceramics. To test the cytocompatibility of these samples, a cell line was cultured and multiple trypsinizations were carried out to ensure the cells remained stable and alive.

To achieve this, the materials used for the biological characterization included a hOB cell line, (Cell Applications, Inc., San Diego, United States of America (USA)), 75 cm^3 cell culture flasks (Orange Scientific, Braine-l'Alleud, Belgium), Dulbecco's Modified Eagle Medium/Nutrient Mixture F-12 (DMEM-F12, from Sigma-Aldrich, Sintra, Portugal), sodium bicarbonate ($NaHCO_3$, from Labchem, Santo Antão do Tojal, Portugal), ultrapure water (obtained using a Milli-Q Advantage A10 ultrapure water purification system, filtered at 0.22 µm and 18.2 MΩ cm at 25 ºC), fetal bovine serum (FBS, Biochrom AG, Berlin, Germany), trypsin and resazurin (Sigma-Aldrich, Sintra, Portugal), and a SpectraMax Gemini EM spectrofluorometer (Molecular Devices, San Jose, California (CA), USA).

The hOB cell line was cultured in a 75 cm^3 t-flask with 10 ml of DMEM-F12 medium, which was supplemented with $NaHCO_3$, doubly deionized water, 10% FBS, and 1% antibiotics. The flask was then incubated at 37 ºC with 5% CO_2. To ensure the cells remain healthy and to prevent overgrowth, multiple trypsinizations were conducted.

Trypsin was employed by adding 5 ml of it to the t-flask containing the cells, allowing it to work for 5 minutes at 37 ºC with 5% CO_2. Trypsin is an enzyme that breaks down proteins, and its function here was to separate the cells from each other and from the t-flask [150]. After trypsinization, the cells are suspended and take on a rounded shape, which can be seen under a microscope. Prolonged exposure to trypsin can harm the cells by stripping away surface proteins, leading to cell death [150]. To prevent this, the enzyme's activity is halted by adding an equal amount of DMEM-F12 medium.

To assess how compatible the sample is with cells, the resazurin assay was performed [151]. After trypsinizing the cells, the mixture (5 ml of trypsin + 5 ml of DMEM-F12 + suspended cells) was placed in a sterile 50 ml Falcon tube and centrifuged at 1500 rpm for 5 minutes at 25 ºC. The

liquid above the cell pellet was removed, and the pellet was then mixed with 1 ml of fresh medium. Next, 20 µl of this solution was moved to an Eppendorf tube, and 180 µl of trypan blue dye was added for cell counting with a Neubauer chamber. The cells were then plated at concentrations of 15000, 10000, and 1500 cells per well in three and incubated at 37 ºC for 24 hours to facilitate cell adhesion. After the incubation period, the medium was removed, and the cells were treated with the samples (10% of material relative to the well area [152]). Then, 300 µl of fresh medium was added to each well. Each sample composition and the negative control (k^-) were tested in 5 wells, resulting in a total of 25 wells per plate, as shown in Figure 12. Additionally, a plate was also set up for positive control (k^+), with bleach added to each well, ensuring cell death.

It's important to note that before incubating the cells with the materials, the materials were sterilized using ultraviolet (UV) irradiation for 1 hour [1]. After incubation periods of 1, 3, and 10 days, the medium was removed, and the hOB cells were treated with 220 µl of 10% (v/v) resazurin solution [151].

Alamar Blue is a commonly used reagent in cell viability tests. It contains resazurin, a non-toxic, non-fluorescent blue dye that can penetrate cells. Resazurin acts as a redox indicator, changing color when it is metabolically reduced by cells. The reduced form, resorufin, is pink and highly fluorescent, with the fluorescence intensity corresponding to the number of live cells present [151, 153].

After incubating the cells with resazurin for 4 hours, cell viability was assessed by measuring the fluorescence of resorufin using excitation and emission wavelengths of 545 nm and 590 nm, respectively [151, 153]. This was done using the SpectraMax Gemini EM spectrofluorimeter. For the measurement, 80 µl from each well of the 48-well plates was transferred to a black 96-well plate with a clear bottom, which is suitable for these readings.

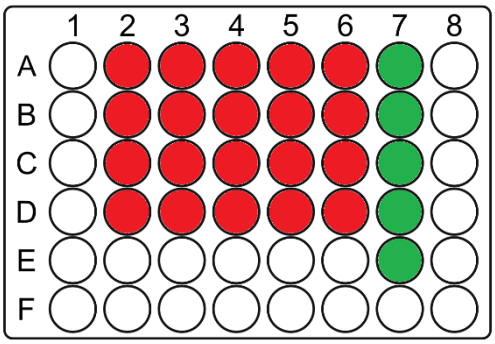

Figure 12. Representation of the layout for a 48-well plate, with rows A, B, C, and D (red wells) representing the control, Ta 3%, Sr 3%, Ta/Sr 1.5%, respectively, and column 7 (green wells) representing the negative control. (Adapted and modified from [154]).

3.5.2. Statistical analysis

The results were statistically analyzed using GraphPad Prism version 8.0 (trial version, GraphPad Software, CA, USA). The data are shown as the mean ± standard deviation. To compare the different groups, a one-way ANOVA followed by the Student-Newman-Keuls test was employed. A p-value of less than 0.05 was deemed statistically significant [153].

4. Results and discussion

This chapter details the experimental results derived from the methodologies described in Chapter 3. These results were systematically analyzed and compared with each other, as well as with those reported in the existing literature.

4.1. Physical properties

4.1.1. Particle size distribution

The PSD of the powders for each composition are presented in Figure 13 a). All compositions exhibited unimodal PSD. The control sample had a d_{50} of 10.78 µm and a d_{90} of 17.18 µm. The Ta 3% sample had a d_{50} of 10.78 µm and a d_{90} of 17.18 µm. The Sr 3% sample showed a d_{50} of 10.78 µm and a d_{90} of 17.18 µm, while the Ta/Sr 1.5% sample had a d_{50} of 9.82 µm and a d_{90} of 15.65 µm. Here, d_{50} and d_{90} indicates that 50% and 90% of the particles are smaller than the respective value, respectively [155]. In [69], despite being HA instead of TCP, a similar behavior in the PSD can be observed.

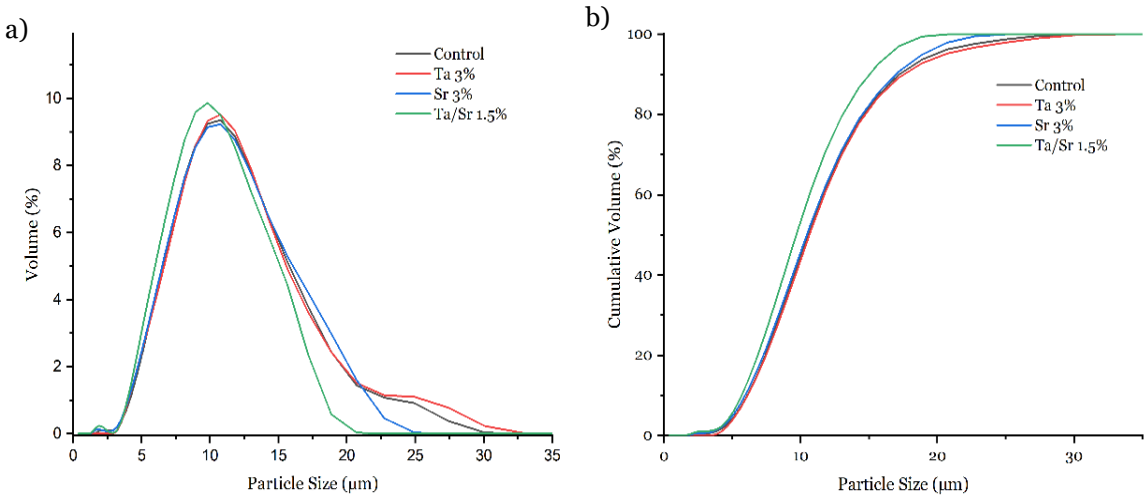

Figure 13. Particle size distribution of the powders compositions: **a)** differential volume; **b)** cumulative volume.

4.1.2. Diametral shrinkage

Figure 14 presents the results of the diametral shrinkage for each composition in a graphical format. These results were obtained as described in Section 3.2. The figure displays the average values derived from 15 samples for each composition.

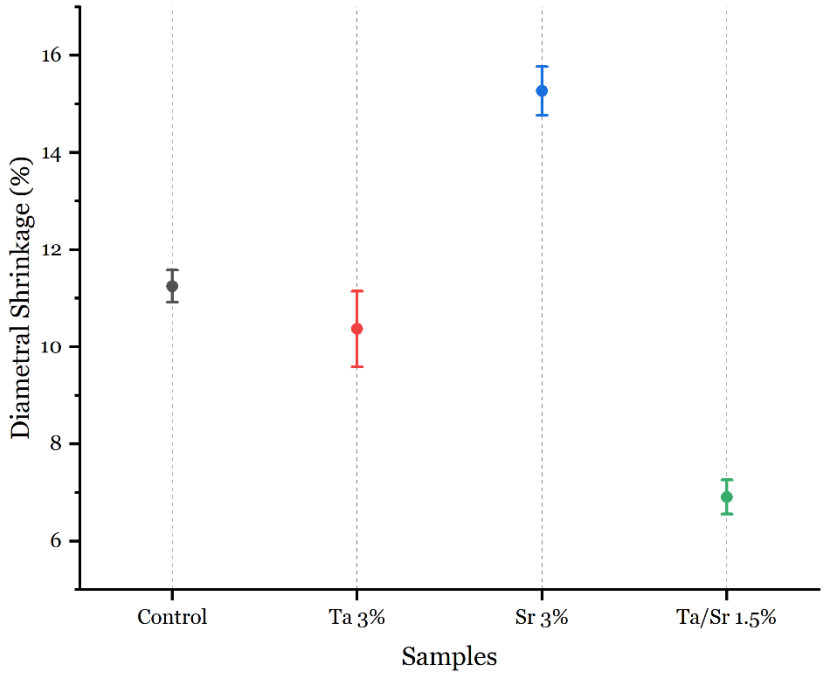

Figure 14. Samples average of diametral shrinkage rate for each composition.

During the sintering process, the samples exhibited diametral shrinkages of 11.25% for the control, 10.37% for Ta 3%, 15.27% for Sr 3%, and 6.91% for Ta/Sr 1,5%. When comparing the control sample with the others, it can be observed that the addition of Ta, despite being minor (0.88%), resulted in a reduction of diametral shrinkage, whereas the incorporation of Sr led to an increase in diametral shrinkage (4.9%). Notably, the sample containing both ions showed a significant reduction in diametral shrinkage (3.46%).

Regarding the standard deviation, while the control sample exhibited the lowest value at ±0.33%, and the Ta/Sr 1,5% sample followed closely at ±0.35%, with Ta 3% and Sr 3% showing higher values of approximately ±0.78% and ±0.5%, respectively, it is important to note that all fifteen samples from the four compositions displayed consistent behavior, with no significant extremes in size differences.

Also, as noted in Section 3.1.2, the differences in initial mass used during the fabrication process (0.6 g, 0.62 g, and 0.65 g) did not lead to consistent changes after sintering. Some discs that initially weighed 0.6 g ended up having a greater mass after sintering than some discs that initially weighed 0.65 g.

4.1.3. Density, porosity and water absorption

All the results presented in the form of graphs were obtained following the procedures outlined in Section 3.2.

Figure 15 displays the apparent density results, illustrating the average values from the fifteen samples of each composition.

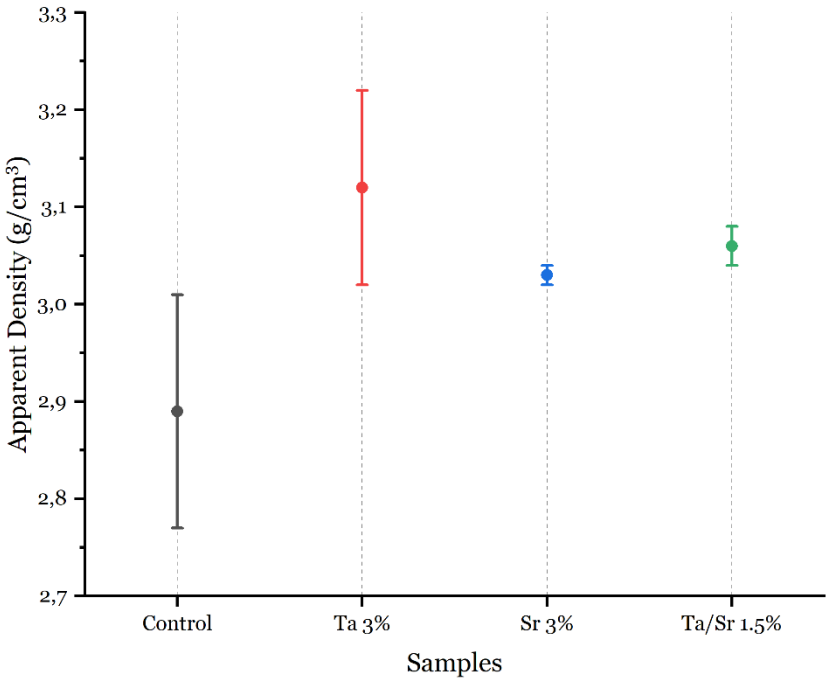

Figure 15. Samples average of apparent density for each composition.

The graph shows that the three ion-doped compositions exhibit higher apparent densities than the control. Specifically, the control has an apparent density of 2.89 g/cm³, Ta 3% has 3.12 g/cm³, Sr 3% has 3.03 g/cm³, and Ta/Sr 1,5% has 3.06 g/cm³, with the Ta 3% composition being the densest.

The standard deviations are ±0.12 g/cm³ for the control, ±0.1 g/cm³ for Ta 3%, ±0.01 g/cm³ for Sr 3%, and ±0.02 g/cm³ for Ta/Sr 1,5%.

Figure 16 displays the water absorption results, illustrating the average values from the fifteen samples of each composition. This test was conducted to assess the hydrophilicity of the samples.

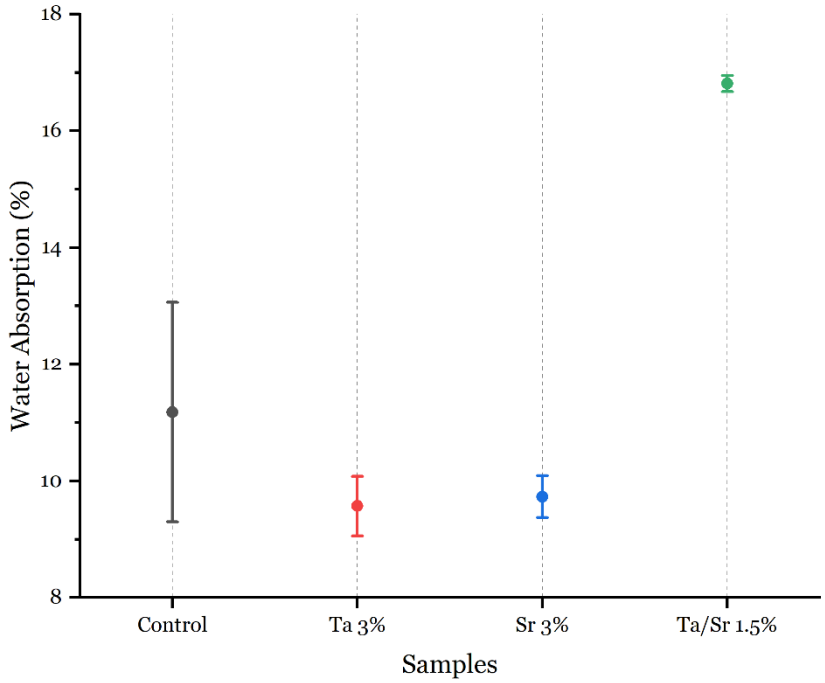

Figure 16. Samples average of water absorption rate for each composition.

Analyzing the results and comparing them to the control sample, the Ta/Sr 1.5% composition exhibited the highest water absorption percentage at 16.81%. In contrast, the Ta 3% and Sr 3% compositions showed lower water absorption levels, at 9.57% and 9.73%, respectively, which are even lower than the control sample's absorption rate of 11.18%.

Regarding the standard deviation, the control sample had a higher value of ±1.88%, whereas the Ta 3%, Sr 3%, and Ta/Sr 1.5% samples had lower standard deviations of ±0.51%, ±0.36%, and ±0.14%, respectively.

Figure 17 shows the apparent porosity results, illustrating the average values from the fifteen samples of each composition.

Like the water absorption results, the Ta/Sr 1.5% composition displayed the highest apparent porosity at 34%, exceeding the control porosity of 24.32%. The Ta 3% and Sr 3% samples exhibited lower porosity values, 22.95% and 22.73% respectively, both of which were less than control.

A similar trend was observed in the standard deviation values, with the control composition showing the highest standard deviation at ± 3.32%. This was followed by the Ta 3% composition with a standard deviation of ± 1.05%, the Sr 3% composition at ±0.69%, and finally, the Ta/Sr 1.5% composition with the lowest standard deviation at ± 0.21%.

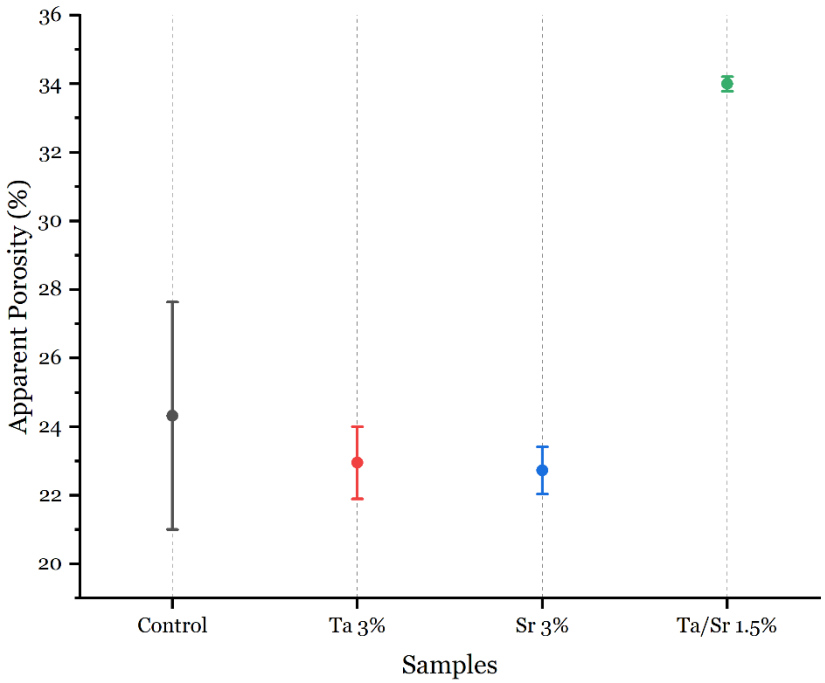

Figure 17. Samples average of apparent porosity for each composition.

For the relative density, in Figure 18, the average values from the fifteen samples for each composition are displayed.

The graph reveals that the doped compositions exhibit higher relative densities than the control sample, which has a relative density of 94%. Specifically, the Ta 3% composition achieved the highest relative density at 101%, indicating a notable increase over the control. This is followed closely by the Ta/Sr 1.5% composition, which has a relative density of 100%, and the Sr 3% composition, which recorded a relative density of 99%.

When examining the standard deviations, the control sample shows the highest variability, with a standard deviation of approximately ± 3.8%. This is higher than that of the Ta 3% composition, which has a standard deviation of ± 3.2%. The Ta/Sr 1.5% and Sr 3% compositions exhibit much lower standard deviations, at ± 0.49% and ± 0.47%, respectively. The lower standard deviations in the doped samples suggest a more consistent measurement of relative density across the samples compared to the control.

It is important to emphasize that some of the relative density values exceed 100%. This occurrence is explained in Section 3.2, where it is noted that the theoretical density used for calculations only accounts for the density of TCP. The densities of the dopants, tantalum and strontium, are not included in the theoretical density values, which can lead to these apparent exceedances. This discrepancy highlights the need for a more comprehensive theoretical density model that includes

the contributions of all components in the material system to achieve more accurate relative density measurements.

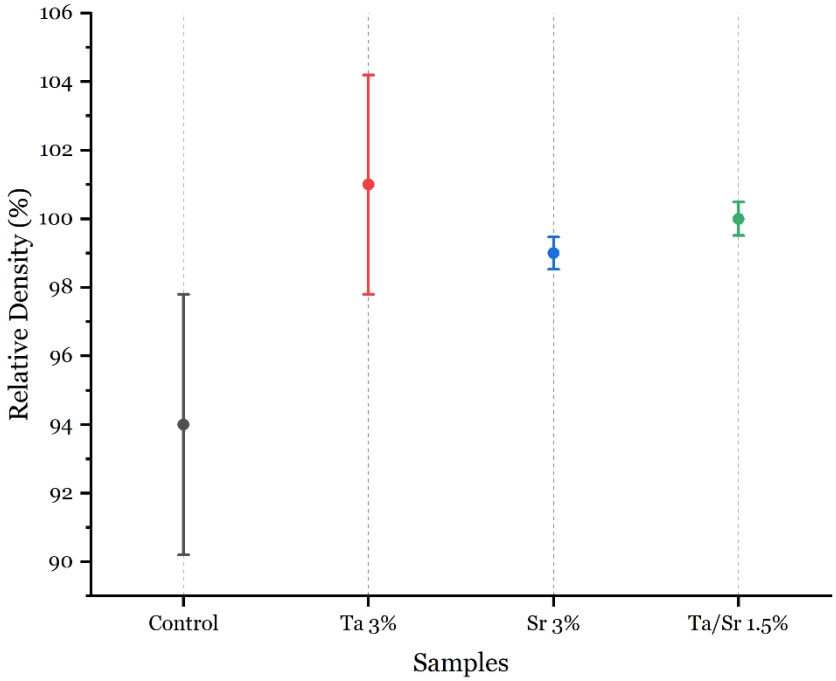

Figure 18. Samples average of relative density for each composition.

4.2. Mechanical properties

4.2.1. Ultimate strength test

All the results presented in graphical form were obtained in accordance with the methodologies and procedures described in Section 3.3.

Figure 19 presents the cumulative probability distributions, for the experimental data and using equation (8) and the Weibull plots.

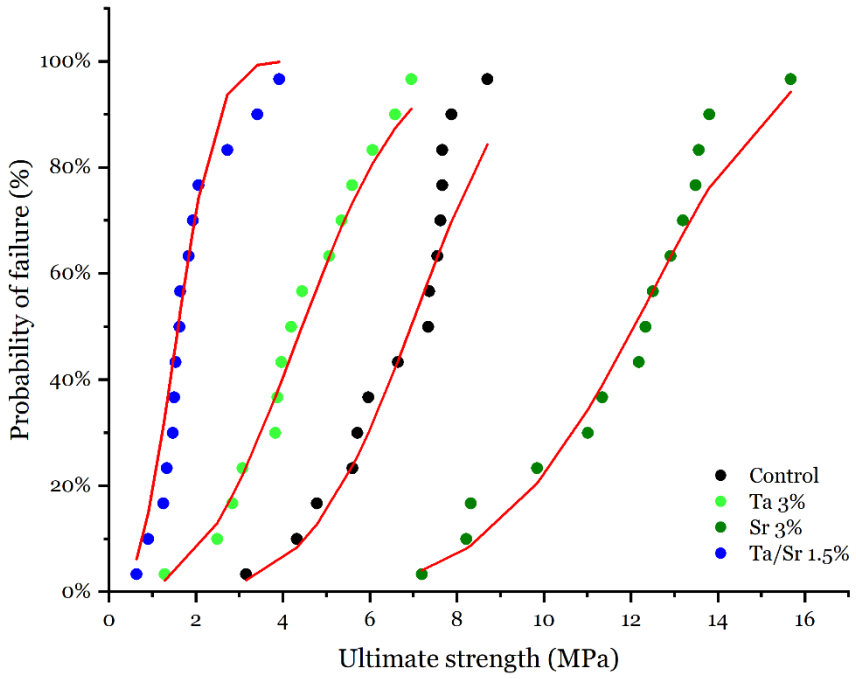

Figure 19. Weibull plots of probability of failure as a function of ultimate strength for each composition. Symbols represent the probability of failure for the experimental data and the continuous red lines are the cumulative distributions calculated using Weibull parameters.

Based on the graph, it is evident that among all compositions, the Sr 3% sample exhibits the highest ultimate strength resistance. At an approximately 63.2% probability of failure, the Sr 3% sample demonstrated a characteristic strength of 12.91 MPa, significantly exceeding the control composition, which showed a characteristic strength of 7.55 MPa at a similar failure probability. In contrast, the Ta 3% and Ta/Sr 1.5% compositions displayed lower characteristic strength values compared to the control, with measurements of 5.35 MPa and 1.83 MPa, respectively.

The differences in characteristic strength observed between the Sr 3% and Ta/Sr 1.5% samples can be explained using data from sections 4.1.2 and 4.1.3. In terms of diametral shrinkage, Sr 3% exhibited the highest value, indicating a greater degree of densification, while Ta/Sr 1.5% showed the lowest shrinkage, suggesting less densification. Although both compositions had similar

apparent densities, they differed significantly in apparent porosity: Ta/Sr 1.5% had the highest porosity, whereas Sr 3% had the lowest. This suggests that the Sr 3% sample, being more compact and less porous, was more resistant to ultimate strength. In contrast, the Ta/Sr 1.5% sample, with its greater size and higher porosity, had weaker compaction, resulting in lower resistance to ultimate strength, despite the similar density.

Ta 3% sample exhibited lower strength compared to the control sample, despite having the highest apparent density and lowest porosity. This outcome can be attributed to several factors, including the nature of densification and the distribution of dopants within the ceramic matrix.

The similar diametral shrinkage between the Ta 3% and control samples suggests comparable levels of densification. However, the Ta 3% sample's higher density indicates that it is more compact, which typically would lead to higher strength. The discrepancy here could be due to microstructural factors. While the material is denser, the distribution of tantalum atoms might not be uniform, potentially leading to areas of localized stress concentration or brittleness, reducing overall strength.

The higher atomic mass of tantalum could play a role in how the material densifies. Heavier atoms may lead to a less uniform grain structure during sintering, with larger tantalum atoms potentially disrupting the lattice or creating regions with different mechanical properties. This can result in increased brittleness or reduced toughness, thus lowering the characteristic strength despite high density and low porosity.

4.2.2. Vickers hardness test

The characteristic Vickers imprints and associated cracks for each composition are shown in Figure 20. In all cases, the imprints cover a considerable area of the specimens, encompassing multiple grains. The impressions are symmetrical, with clear and well-defined edges, and no evidence of grain pull-out was observed. Consequently, these imprints were deemed suitable for accurately determining the Vickers hardness. More detailed images can be found in the appendix.

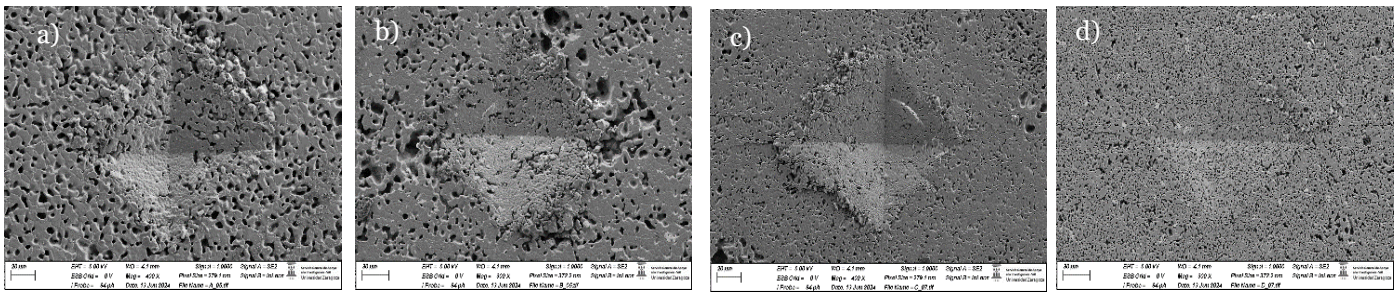

Figure 20. Results from Vickers hardness test for each composition, **a)** control, **b)** Ta 3%, **c)** Sr 3%, and **d)** Ta/Sr 1.5%.

Figure 21 presents the graphical results of the Vickers hardness test, depicting the average values obtained from four measurements for each composition.

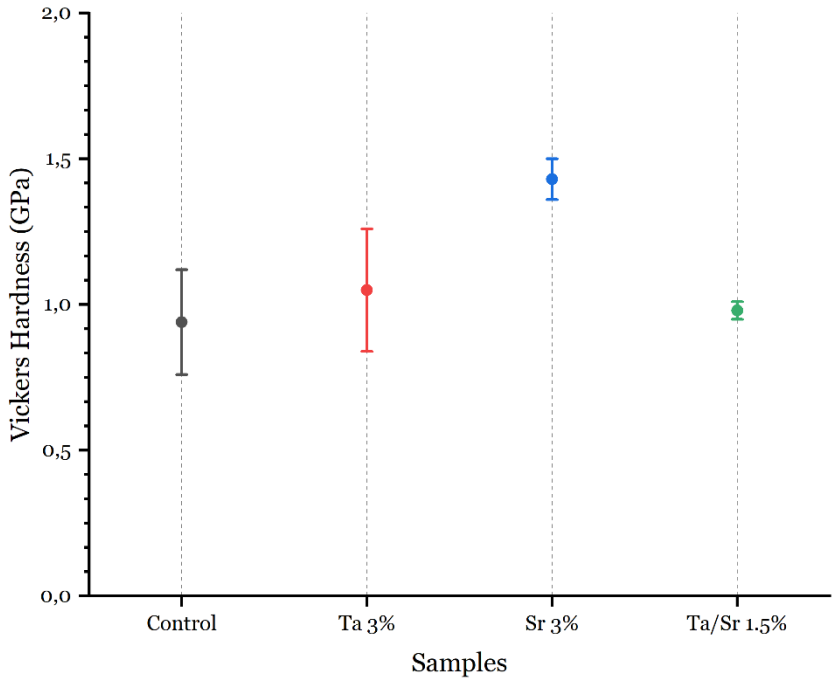

Figure 21. Samples average of Vickers hardness test for each composition.

Analyzing the results and comparing them to the control sample, it is evident that all doped compositions exhibit higher Vickers hardness than the control. The control sample has a Vickers hardness of 0.94 GPa, while the Ta 3%, Sr 3%, and Ta/Sr 1.5% samples show values of 1.05 GPa, 1.43 GPa, and 0.98 GPa, respectively, with Sr 3% having the highest value. The higher value of HV than control indicates that doped samples are more resistant to indentation and wear.

Regarding standard deviation, the control sample has a standard deviation of ±0.18 GPa, Ta 3% has ±0.21 GPa, Sr 3% has ±0.07 GPa, and Ta/Sr 1.5% has ±0.03 GPa. The control and Ta 3% samples exhibit the highest standard deviation values, indicating more variability, whereas Sr 3% and Ta/Sr 1.5% show lower standard deviations, suggesting more consistent hardness measurements.

When comparing the control sample with the literature [147], the results show a lower value. This discrepancy could be due to variations in the applied load, as the article does not specify the load used in their testing.

A consistent pattern of standard deviation values is observed across most graphs, except for the diametral shrinkage data, with the control and Ta 3% samples consistently showing the highest variability.

4.3. Microstructural properties

4.3.1. X-ray diffraction

To verify the incorporation of Ta^{5+} and Sr^{2+} ions into the TCP lattice during calcination and sintering, X-ray diffraction (XRD) analyses were performed. Figure 22 displays the diffraction patterns of the various compositions, illustrating the intensity of diffracted radiation as a function of the 2θ angle. These experimental patterns are compared with theoretical standard patterns from reference cards #09-432 (HA), #09-348 (α-TCP), #09-169 (β-TCP), #04-0788 (Ta), #44-1008 ($Ca_2Ta_2O_7$), and #15-0305 (Sr) to aid in phase identification.

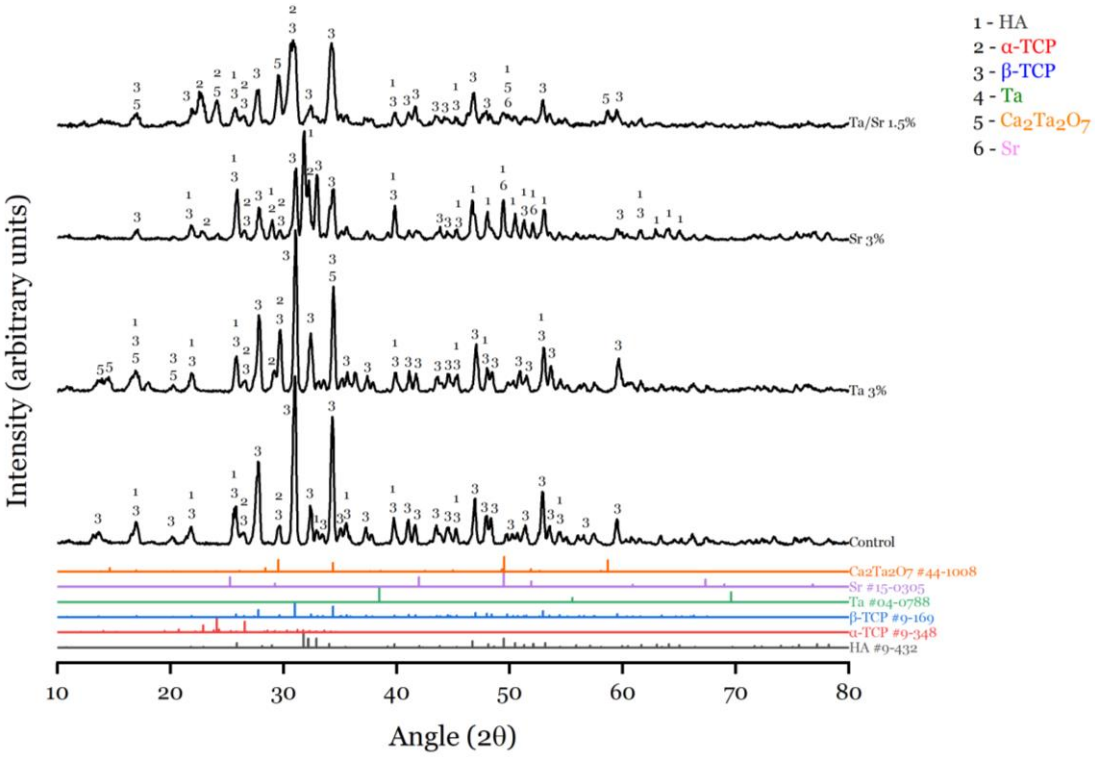

Figure 22. X-ray diffraction patterns of the studied compositions compared with theoretical standard patterns.

Upon analyzing Figure 22 for the control sample, seven primary peaks with high intensity (394 or above) are observed at 2θ values of 25.8°, 27.75°, 31°, 32.35°, 34.3°, 46.95°, and 52.9°. These peaks correspond to β-TCP, except for the peak at 25.8°, which can correspond to either β-TCP or HA, as it coincides with both standards. This sample predominantly features β-TCP, but the presence of HA and α-TCP cannot be ruled out due to corresponding peaks. Also, comparing to the study [147], the control sample exhibits a similar peak behavior.

The Ta 3% sample displays eight primary peaks with high intensity at 2θ values of 25.85°, 27.8°, 29.7°, 31.05°, 32.4°, 34.4°, 47.05°, and 53°. These peaks correspond to β-TCP, except for those at 27.8° and 53°, which could correspond to either β-TCP or HA, and the peak at 31.05°, which

could indicate either β-TCP or α-TCP. Like the control sample, this sample predominantly exhibits β-TCP. No peaks corresponding to tantalum were detected, suggesting that most of the Ta ions have been incorporated into the lattice. However, the peaks at 2θ = 14.55°, 16.90°, 20.25°, and 34.40° likely correspond to a newly formed compound, identified as $Ca_2Ta_2O_7$. According to the study in [88], this compound was observed during their research on HA doped with Tantalum

The Sr 3% sample exhibits eight primary peaks with high intensity at 2θ values of 25.9°, 31.1°, 31.85°, 32.25°, 32.95°, 34.4°, 46.7°, and 49.45°. The peak at 25.9° can correspond to either HA or β-TCP, while the peaks at 31.1°, 32.95°, and 34.4° correspond to β-TCP. The peaks at 31.85° and 46.7° correspond to HA, and the peak at 49.45° can correspond to either HA or Sr. The last primary peak and an additional minor peak both suggest the possible presence of Sr outside the TCP lattice.

The Ta/Sr 1.5% sample exhibits five primary peaks with high intensity at 2θ values of 22.55°, 27.65°, 29.5°, 30.7°, and 34.25°. The peak at 22.55° corresponds to α-TCP, 29.5° corresponds to $Ca_2Ta_2O_7$, while the peak at 30.7° correspond to either α-TCP or β-TCP. The peak 34.25° correspond to β-TCP. Comparing these results with the Sr 3% sample, the presence of a strontium peak in the Sr 3% sample suggests that the higher amount of strontium (3 wt%) may have led to lattice oversaturation of Sr ions.

4.3.2. Scanning electron microscopy

Figure 23 displays the surfaces of each composition, captured using SEM at magnifications of 500x and 2000x. More detailed images can be found in the appendix.

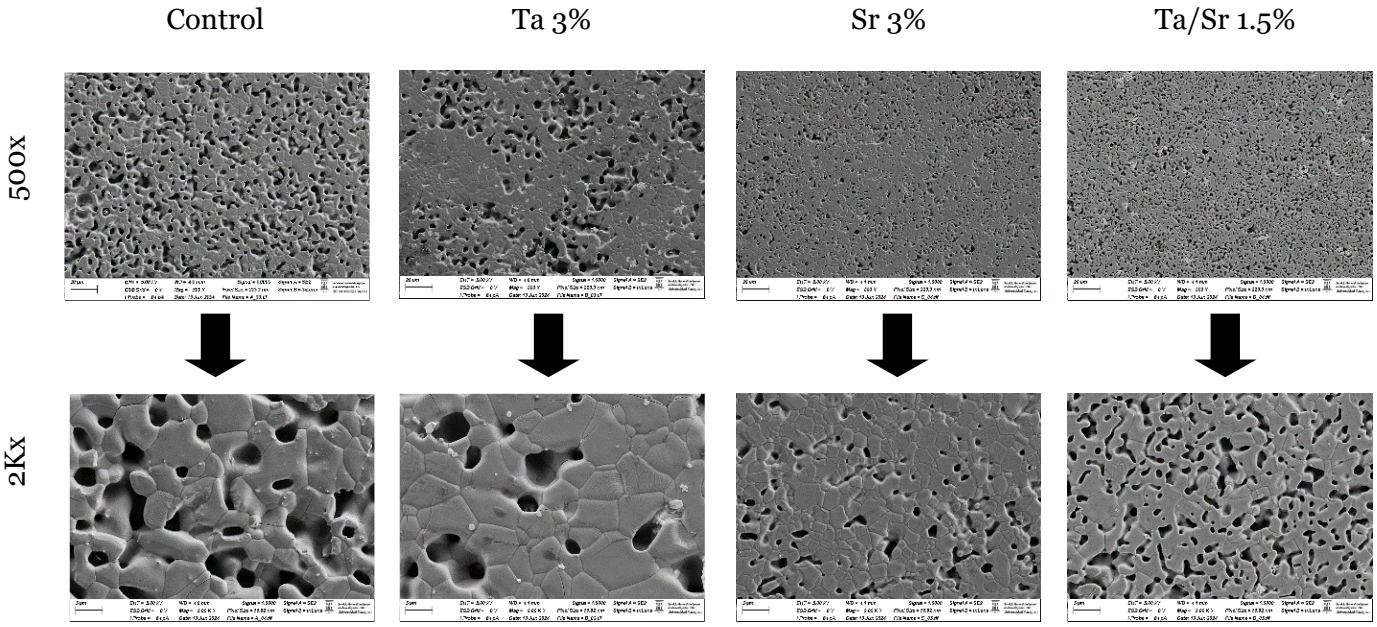

Figure 23. SEM images of the surfaces of each composition at 500x and 2000x magnifications.

At 500x magnification, the control, Sr 3%, and Ta/Sr 1.5% samples demonstrate a homogeneous distribution of pores and grain sizes in the TCP structure. In contrast, the Ta 3% sample displays a non-uniform pore distribution, with some regions showing an absence of pores. Moreover, when compared to the control, both the Sr 3% and Ta/Sr 1.5% samples have a higher number of pores, though these pores are of smaller dimensions. With these images, both experimental results of density and porosity are confirmed.

At a magnification of 2000x, it is possible to measure the chord length and determine the shapes of the pores and grains. In the control sample, pore sizes range from approximately 1.59 µm to 7.67 µm, while grain sizes vary from 2.28 µm to 13.93 µm. In the Ta 3% sample, pores range from about 1.89 µm to 7.01 µm, and grain sizes span from 0.72 µm to 15.97 µm. The Sr 3% sample features smaller pores, ranging from 0.35 µm to 4.27 µm, with grains between 0.29 µm and 7.67 µm. For the Ta/Sr 1.5% sample, pores vary from 0.28 µm to 4.36 µm, while grain sizes are between 1.44 µm and 9.44 µm. These porous sizes are related to the experimental mechanical results.

In terms of shape, all samples exhibit pores with a generally regular form, predominantly rounded and occasionally cylindrical. For the grains, all compositions except Ta/Sr 1.5% display a regular shape, with most being faceted and occasionally circular or cylindrical. The grains in the Ta/Sr 1.5% sample appear irregular, the grains look like they melted which each other, which makes their outlines difficult to distinguish.

Except for the Sr 3% sample, the 2000x magnification reveals the presence of fracture lines in some samples. These lines may have been caused by the ultimate strength test or by the sintering process, as these SEM images were taken from the best-performing samples in the test.

Figure 24 shows the fracture surfaces of each composition, captured using SEM at the same magnifications. More detailed images can be found in the appendix.

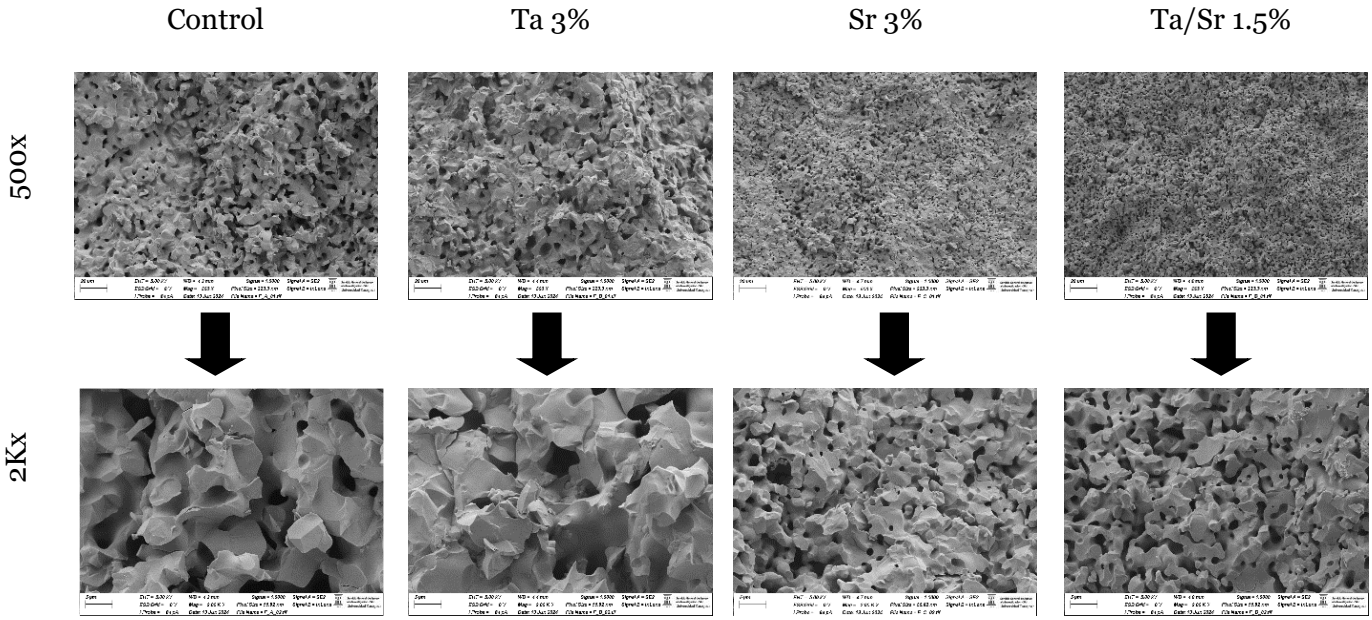

Figure 24. SEM images of the fracture surfaces of each composition at 500x and 2000x magnifications.

Observing Figure 24, it is evident that all samples exhibit different fracture surfaces, the majority being transgranular and sporadically some intergranular fractures, as shown in the detailed images provided in the appendix. Transgranular fractures occur when cracks propagate through the grains, while intergranular fractures occur along the grain boundaries [63].

Regarding porosity, in addition to the characteristics described earlier in Figure 23, the presence of an interconnected porosity network is also evident.

4.4. Biological properties

4.4.1. Cytocompatibility tests

The cytocompatibility test results for the compositions, depicted in Figure 25, were derived following the procedure outlined in section 3.5. The graph illustrates the cell viability of hOBs incubated with samples from the four compositions over periods of 1, 3, and 10 days.

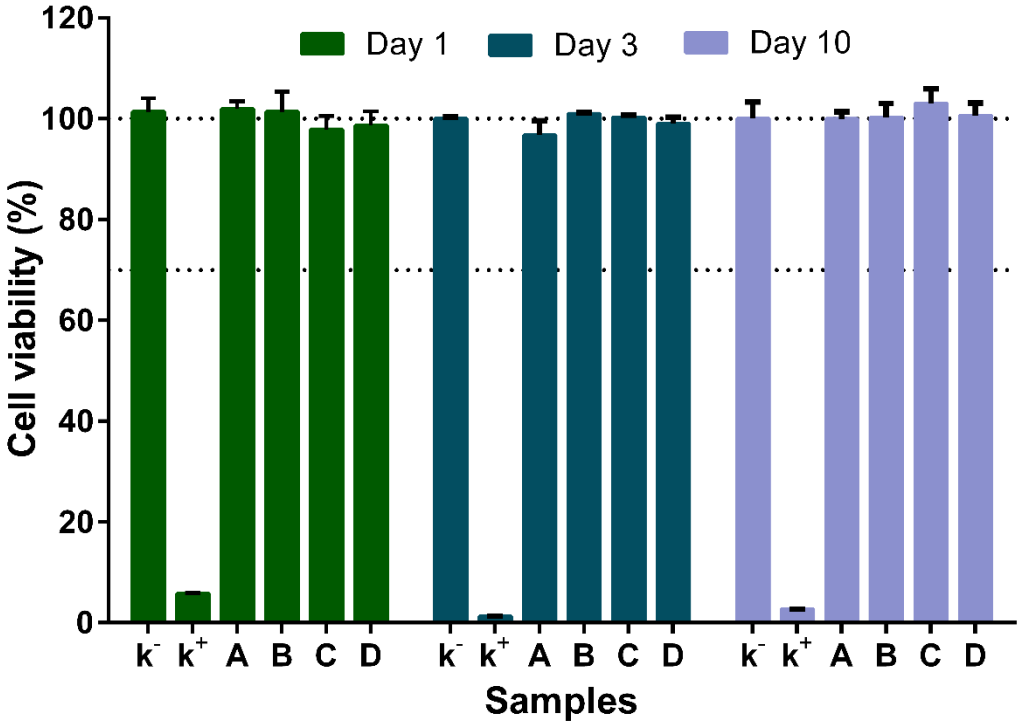

Figure 25. Evaluation of the cytocompatibility of the samples, with **A** representing the control sample, **B** representing Ta 3% sample, **C** representing Sr 3% sample, and **D** representing Ta/Sr 1.5% sample.

The samples biocompatibility was assessed through the resazurin assay. In this study, hOB cells were utilized as a 2D model due to their critical role in the production and remodeling of the bone matrix [156], a key factor in the osseointegration process.

As shown in Figure 25, after 10 days of incubation, the hOB cells remained metabolically active when exposed to the samples, with cell viability significantly exceeding 70%. This high level of cell viability was anticipated, as both tantalum and strontium are documented in the literature as non-toxic to cells [61, 62, 85-89].

5. Proof of concept

This short chapter demonstrates the use of tantalum- and strontium-doped bioceramic as a coating. It provides a concise explanation of the reasons for its implementation, outlines the materials and production methods used for the coating, and concludes with a visual analysis that illustrates its feasibility, this chapter was based of the investigation [86].

5.1. Reason

The use of bioceramic coatings, as previously discussed, is intended to prevent cellular fibrosis at the bone-prosthesis interface. For successful outcomes, it is essential to use materials that closely resemble bone properties and are non-toxic. Ta- and Sr-doped TCP is a promising candidate for this application due to its similarity to bone, lack of toxicity, and ability to promote bone formation, as outlined earlier.

5.2. Materials and methodology

To create the coating, the sol-gel method was chosen due to its simplicity and effective results. The sol-gel was prepared using the same powder utilized for disc formation, mixed with distilled water at a ratio of 45% wt of powder to water. To ensure the stability of the colloidal solution and facilitate its formation, a few drops of Dolapix CE 54 dispersant (Hans Barnstorf & C^{a} Lda.) were added. The solution was in continuous agitation for 2 hours at approximately 50 ºC.

Titanium discs with the alloy TI-6Al-4V, having a diameter of 8 mm and a thickness of 1.8 mm, were chosen as the substrate. This titanium alloy was selected because of its prevalent application in biomedical implants, which is attributed to its outstanding biocompatibility, robust mechanical properties, and resistance to corrosion, as previously mentioned. The substrate underwent no pre-treatment other than alcohol cleaning and polishing.

To apply the sol-gel coating to the substrate, the dip-coating method was employed. The sol-gel solution was maintained in constant agitation while the substrate was submerged for a few seconds before being placed in an oven to dry. This dipping and drying process was repeated multiple times to ensure an even and consistent coating. Subsequently, the sol-gel-coated substrates were sintered in a controlled stepwise manner: starting at 100 ºC for 1 hour, followed by 350 ºC for 2 hours, and finally reaching 500 ºC for 15 minutes to prevent cracks in the crystallization. This procedure was conducted twice to achieve two layers of coating for each composition type (control, Ta 3%, Sr 3%, and Ta/Sr 1.5%).

As this section serves as a proof of concept, only the microstructure of each sample was examined. The microstructural analysis of the sintered samples was conducted using SEM imaging (Hitachi S-3400 N, Japan). Before imaging, the sample surfaces were coated with a thin gold layer using a turbomolecular-pumped coater (Quorum Technologies Q150R ES, United Kingdom). SEM

images were obtained in backscattered electron (BSE) 3D mode at an accelerating voltage of 15 kV.

5.3. Microstructure analysis and discussion

Figure 26 shows the SEM images of each composition at magnifications of 1000x and 5000x. More detailed images can be found in the appendix.

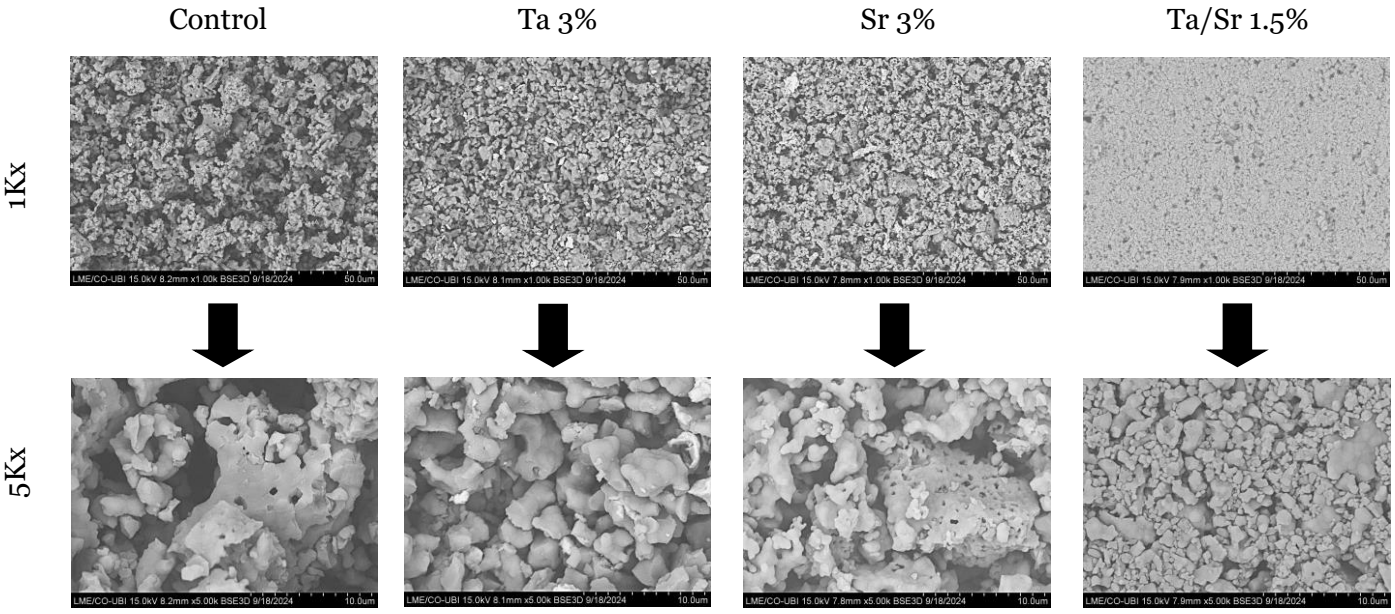

Figure 26. SEM images of the sol-gel coating surface for each composition at magnifications of 1000x and 5000x.

At a magnification of 1000x, all samples exhibit a relatively homogeneous surface. The control, Ta 3%, and Sr 3% samples show larger empty spaces, whereas the Ta/Sr 1.5% sample has smaller ones. This rough surface is a promising indicator for cell adhesion.

When magnified to 5000x, we observe that in all samples, some grains are interconnected while others appear loose. This looseness is most pronounced in the Ta/Sr 1.5% sample, where most grains are detached, with only occasional connections. Furthermore, during the acquisition of SEM images, it was observed that the interaction of the electron beams with the surface induced movement in the grains. This suggests that the sintering temperature was not optimal for fully bonding the grains. To solve this problem, an optimization in the process of sintering must be acquired.

This analysis suggests that the Ta/Sr 1.5% composition displays the least advantageous microstructure, mainly due to the significant presence of loose grains. Conversely, the Sr 3% composition appears to possess the most favorable structure, characterized by a higher density of sintered grains and enhanced interconnectivity among them.

In comparison to the study in [86], on which this section is based, the microstructures exhibit similar features: a rough surface with some grains interconnected and others loose, even though the base materials differ (their study used HA).

It is important to emphasize that due to the recent nature of this study, there is a lack of sufficient research for comparison with the obtained results. Existing studies either involve doping with different ions or utilizing alternative base materials. This challenge is present in both areas of investigation, whether related to bone substitution or coatings.

6. Final remarks

This chapter summarizes the key findings from the research on TCP samples doped with Ta and Sr, exploring their use as bone substitutes and coatings. Additionally, future directions for this field are outlined.

6.1. Conclusions

As life expectancy continues to rise, aging brings about various health challenges, especially in terms of bone regeneration. Therefore, it is crucial to identify effective solutions that enhance well-being and support a healthier life.

When using biomaterials as bone substitutes, it is essential not only to evaluate their physical and mechanical properties but also to perform a thorough biological characterization. For this purpose, analyses were conducted on the following compositions: TCP, TCP doped with Ta 3% wt, TCP doped with Sr 3% wt, and TCP doped with both Ta and Sr, each 1.5% wt.

Samples exhibiting potential for biocompatibility were developed, as they demonstrated no signs of cytotoxicity following 10 days of exposure to human osteoblast hOB cells.

The particle size distribution analysis revealed that all compositions exhibited comparable particle sizes, with no significant variations observed between them. This suggests a consistent particle size profile across the different samples.

Regarding the physical properties, doping TCP with Ta 3% increases apparent density while reducing porosity and water absorption compared to the control (pure TCP). It also decreases diametral shrinkage, helping the material retain more of its original size. Similarly, Sr 3% doping raises density and reduces porosity and water absorption, but unlike Ta 3%, it leads to greater diametral shrinkage. When both Ta 1.5% and Sr 1.5% are co-doped into TCP, the behavior shifts: while diametral shrinkage is still lower, all other properties, (density, porosity, and water absorption), are higher than in the control.

With respect to mechanical properties, the Sr 3% sample demonstrated an increased ultimate strength compared to the control, whereas both Ta 3% and Ta/Sr 1.5% exhibited reduced ultimate strengths. In the Vickers hardness test, all doped samples achieved higher hardness values than the control; however, the Ta/Sr 1.5% sample's hardness was notably closer to that of the control. Based on the results, the addition of Ta and Sr to TCP had a significant impact on the material's properties.

Concerning the microstructural properties, the XRD analysis reveals that the diffraction peaks are generally consistent across all compositions, predominantly identifying β-TCP and HA. Additionally, in the Ta 3% sample, several peaks corresponding to a new compound ($Ca_2Ta_2O_7$)

were detected. In the Sr 3% sample, peaks indicative of Sr was observed, while in the Ta/Sr 1.5% sample, some peaks may correspond to Sr and/or the new compound.

The SEM analysis included two types of images: the surface morphology and the fracture surface of each composition. All compositions displayed a homogeneous distribution of pores and grain sizes, except for the Ta 3% sample, which exhibited a non-uniform pore distribution. The introduction of ions led to a decrease in pore size and an increase in grain size; however, when co-doped, both pore and grain sizes decreased compared to the control sample. Regarding pore shape, most exhibited a regular rounded form, occasionally appearing cylindrical. The grains, except for those in the Ta/Sr 1.5% sample, which appeared to have melted together, were predominantly regular and faceted. The fracture surface analysis revealed a notable presence of transgranular fractures, with some intergranular fractures observed, along with an evident interconnected porosity network.

To verify the feasibility of producing these compositions via a sol-gel method for coating metallic prostheses, microstructural analyses were performed. The results showed that each composition exhibited a relatively rough, homogeneous surface, which is a promising indicator for cell adhesion. All samples displayed a combination of interconnected and loose grains, with the Ta/Sr 1.5% sample showing a higher degree of grain looseness. This suggests that the sintering temperature may not have been optimal for achieving full grain bonding in this composition.

In conclusion, this study confirmed the possibility to produce bone substitute with Ta and Sr doped TCP with 3% of wt and 1.5% wt. Also, it confirmed that the same composition can be implemented in a sol-gel method but needs optimization in the process of fabrication for better results.

6.2. Future perspectives

To enhance the understanding of the behavior of the compositions developed in this master's dissertation, which demonstrate significant potential for use as bone substitutes and prosthetic coatings, the following recommendations for future research are proposed:

For the bulk samples:

- Conduct further analyses, such as X-ray photoelectron spectroscopy (XPS), to gain more detailed information about the chemical composition of the TCP lattice;
- Acquire SEM images to observe the behavior of hOB cells on the surface of each composition;
- Determine the maximum concentrations of tantalum and strontium that can be doped into the TCP and compare the resultant behavior with the findings of this study;

- Conduct tests to assess ionic release and bioactivity in simulated body fluid (SBF), evaluate degradation and dissolution rates, examine osteogenic differentiation and mineralization, perform angiogenesis assays, and ultimately undertake *in vivo* studies.

For the coating:

- Implement appropriate pre-treatment procedures for the substrate;
- Optimize the sol-gel formation process by adjusting the quantities of each powder, temperature, coating method (e.g., dip or spin), and the number of layers to be applied;
- Optimize the sintering process by testing various temperatures and subsequently comparing the results;
- Perform a precise cutting and/or polishing to reveal the interface between the bioceramic and substrate, followed by analysis using SEM images;
- Conduct hOB viability tests to evaluate the compatibility of the bioceramic, followed by SEM imaging to observe cellular behavior;
- Perform tests to evaluate ionic release and bioactivity in SBF, assess degradation and dissolution rates, examine osteogenic differentiation and mineralization, conduct angiogenesis assays, and ultimately undertake *in vivo* studies.

7. Bibliographic references

[1] M. F. Vassal, J. Nunes-Pereira, S. P. Miguel, I. J. Correia, and A. P. Silva, "Microstructural, mechanical and biological properties of hydroxyapatite - $CaZrO_3$ biocomposites," *Ceramics International,* vol. 45, no. 7, Part A, pp. 8195-8203, May. 2019, doi: https://doi.org/10.1016/j.ceramint.2019.01.122.

[2] V. P. Mantripragada, B. Lecka-Czernik, N. A. Ebraheim, and A. C. Jayasuriya, "An overview of recent advances in designing orthopedic and craniofacial implants," *Journal of Biomedical Materials Research Part A,* vol. 101, no. 11, pp. 3349-3364, Jun. 2013, doi: https://doi.org/10.1002/jbm.a.34605.

[3] U. Tarantino *et al.*, "Hip Osteoarthritis and Osteoporosis: Clinical and Histomorphometric Considerations," *International Journal of Endocrinology,* vol. 2014, no. 1, p. 372021, Apr. 2014, doi: https://doi.org/10.1155/2014/372021.

[4] Institute for Health Metrics and Evaluation (IHME). "WHO Rehabilitation Need Estimator." IHME, University of Washington. https://vizhub.healthdata.org/rehabilitation/ (accessed Nov. 23, 2023).

[5] T. M. Volkmer and L. A. d. Santos, "Influência do tempo de indução nas propriedades de hidroxiapatita porosa obtida por gelcasting de espumas," *Cerâmica,* vol. 53, no. 328, pp. 429-435, Oct. 2007, doi: https://doi.org/10.1590/S0366-69132007000400015.

[6] D. F. Williams, "On the nature of biomaterials," *Biomaterials,* vol. 30, no. 30, pp. 5897-5909, Oct. 2009, doi: https://doi.org/10.1016/j.biomaterials.2009.07.027.

[7] M. Geetha, A. K. Singh, R. Asokamani, and A. K. Gogia, "Ti based biomaterials, the ultimate choice for orthopaedic implants – A review," *Progress in Materials Science,* vol. 54, no. 3, pp. 397-425, May. 2009, doi: https://doi.org/10.1016/j.pmatsci.2008.06.004.

[8] W. Suchanek and M. Yoshimura, "Processing and properties of hydroxyapatite-based biomaterials for use as hard tissue replacement implants," *Journal of Materials Research,* vol. 13, no. 1, pp. 94-117, Jan. 1998, doi: https://doi.org/10.1557/JMR.1998.0015.

[9] S. Andrey, R. Maria, and M. Živko, "To Build or Not to Build: The Interface of Bone Graft Substitute Materials in Biological Media from the View Point of the Cells," in *Biomaterials Science and Engineering*, P. Rosario Ed. Rijeka: IntechOpen, 2011, ch. 14, pp. 287-308.

[10] D. F. Macedo, A. F. Cunha, J. F. Mano, M. B. Oliveira, and A. P. Silva, "Tricalcium phosphate doped with Mg^{2+} and combinations of Mn^{2+}, Zn^{2+} and Fe^{3+}: A DoE study on

sintering, mechanical, microstructural and biological properties," *Ceramics International,* vol. 48, no. 14, pp. 20467-20477, Jul. 2022, doi: https://doi.org/10.1016/j.ceramint.2022.04.004.

[11] E. Champion, "Sintering of calcium phosphate bioceramics," *Acta Biomaterialia,* vol. 9, no. 4, pp. 5855-5875, Apr. 2013, doi: https://doi.org/10.1016/j.actbio.2012.11.029.

[12] N. Eliaz and N. Metoki, "Calcium Phosphate Bioceramics: A Review of Their History, Structure, Properties, Coating Technologies and Biomedical Applications," *Materials,* vol. 10, no. 4, p. 334, Mar. 2017, doi: https://doi.org/10.3390/ma10040334.

[13] T. V. Thamaraiselvi and S. Rajeswari, "Biological Evaluation of Bioceramic Materials - A Review," *Trends in biomaterials & artificial organs,* vol. 18, 2004. [Online]. Available: https://api.semanticscholar.org/CorpusID:31120404.

[14] R. F. Bonan, P. R. F. Bonan, A. U. D. Batista, J. E. Oliveira, R. R. Menezes, and E. S. Medeiros, "Métodos de reforço microestrutural da hidroxiapatita," *Cerâmica,* vol. 60, no. 355, pp. 402-410, Jul. 2014, doi: https://doi.org/10.1590/S0366-69132014000300012.

[15] S. J. Kalita, A. Bhardwaj, and H. A. Bhatt, "Nanocrystalline calcium phosphate ceramics in biomedical engineering," *Materials Science and Engineering: C,* vol. 27, no. 3, pp. 441-449, Apr. 2007, doi: https://doi.org/10.1016/j.msec.2006.05.018.

[16] B. D. Ratner, A. S. Hoffman, F. J. Schoen, and J. E. Lemons, "Metals," in *Biomaterials Science: An Introduction to Materials in Medicine*, 2 ed.: Elsevier Science, 2004, ch. 2.9, pp. 137-152.

[17] L. Rony, R. Lancigu, and L. Hubert, "Intraosseous metal implants in orthopedics: A review," *Morphologie,* vol. 102, no. 339, pp. 231-242, Dec. 2018, doi: https://doi.org/10.1016/j.morpho.2018.09.003.

[18] B. D. Rattier, A. S. Hoffman, F. J. Schoen, and J. E. Lemons, "Biomaterials Science: An Introduction to Materials in Medicine," *Journal of Clinical Engineering,* vol. 22, no. 1, p. 26, 1997. [Online]. Available: https://journals.lww.com/jcejournal/fulltext/1997/01000/biomaterials_science__an_introduction_to_materials.9.aspx.

[19] A. Bekmurzayeva, W. J. Duncanson, H. S. Azevedo, and D. Kanayeva, "Surface modification of stainless steel for biomedical applications: Revisiting a century-old material," *Materials Science and Engineering: C,* vol. 93, pp. 1073-1089, Dec. 2018, doi: https://doi.org/10.1016/j.msec.2018.08.049.

[20] A. Biesiekierski, J. Wang, M. Abdel-Hady Gepreel, and C. Wen, "A new look at biomedical Ti-based shape memory alloys," *Acta Biomaterialia,* vol. 8, no. 5, pp. 1661-1669, May. 2012, doi: https://doi.org/10.1016/j.actbio.2012.01.018.

[21] Y. Okazaki and E. Gotoh, "Comparison of metal release from various metallic biomaterials in vitro," *Biomaterials,* vol. 26, no. 1, pp. 11-21, Jan. 2005, doi: https://doi.org/10.1016/j.biomaterials.2004.02.005.

[22] D. Beyersmann and A. Hartwig, "Carcinogenic metal compounds: recent insight into molecular and cellular mechanisms," *Archives of Toxicology,* vol. 82, no. 8, pp. 493-512, Aug. 2008, doi: https://doi.org/10.1007/s00204-008-0313-y.

[23] B. Shah *et al.*, "High rates of metal allergy amongst Nuss procedure patients dictate broader pre-operative testing," *Journal of Pediatric Surgery,* vol. 49, no. 3, pp. 451-454, Mar 2014, doi: https://doi.org/10.1016/j.jpedsurg.2013.07.014.

[24] M. Zhubrak and T. Bar-David, "Systemic Nickel Allergy after Internal Fixation of a Bunionectomy," *The Journal of Foot and Ankle Surgery,* vol. 53, no. 4, pp. 466-467, Jul. 2014, doi: https://doi.org/10.1053/j.jfas.2014.03.006.

[25] X. Gao, R.-x. He, S.-g. Yan, and L.-d. Wu, "Dermatitis Associated With Chromium Following Total Knee Arthroplasty," *The Journal of Arthroplasty,* vol. 26, no. 4, pp. 665.e13-665.e16, Jun. 2011, doi: https://doi.org/10.1016/j.arth.2010.06.002.

[26] G. Welsch, R. Boyer, and E. W. Collings, "Classification of Titanium Alloys," in *Materials Properties Handbook: Titanium Alloys*: ASM International, 1993, ch. 2, sec. 1, pp. 5-11.

[27] M. Abdel-Hady Gepreel and M. Niinomi, "Biocompatibility of Ti-alloys for long-term implantation," *Journal of the Mechanical Behavior of Biomedical Materials,* vol. 20, pp. 407-415, Apr. 2013, doi: https://doi.org/10.1016/j.jmbbm.2012.11.014.

[28] X. Liu, P. K. Chu, and C. Ding, "Surface modification of titanium, titanium alloys, and related materials for biomedical applications," *Materials Science and Engineering: R: Reports,* vol. 47, no. 3, pp. 49-121, Dec. 2004, doi: https://doi.org/10.1016/j.mser.2004.11.001.

[29] S. R. Frenkel, W. L. Jaffe, F. Dimaano, K. Iesaka, and T. Hua, "Bone response to a novel highly porous surface in a canine implantable chamber," *Journal of Biomedical Materials Research Part B: Applied Biomaterials,* vol. 71B, no. 2, pp. 387-391, Nov. 2004, doi: https://doi.org/10.1002/jbm.b.30104.

[30] Y. Okazaki, T. Tateishi, and Y. Ito, "Corrosion Resistance of Implant Alloys in Pseudo Physiological Solution and Role of Alloying Elements in Passive Films," *Materials*

Transactions, JIM, vol. 38, no. 1, pp. 78-84, 1997, doi: https://doi.org/10.2320/matertrans1989.38.78.

[31] V. A. Dubok, "Bioceramics – Yesterday, Today, Tomorrow," *Powder Metallurgy and Metal Ceramics,* vol. 39, no. 7, pp. 381-394, Jul. 2000, doi: https://doi.org/10.1023/A:1026617607548.

[32] L. L. Hench, "The story of Bioglass®," *Journal of Materials Science: Materials in Medicine,* vol. 17, no. 11, pp. 967-978, Nov. 2006, doi: https://doi.org/10.1007/s10856-006-0432-z.

[33] M. Hisbergues, S. Vendeville, and P. Vendeville, "Zirconia: Established facts and perspectives for a biomaterial in dental implantology," *Journal of Biomedical Materials Research Part B: Applied Biomaterials,* vol. 88B, no. 2, pp. 519-529, Jun. 2009, doi: https://doi.org/10.1002/jbm.b.31147.

[34] P. Christel, A. Meunier, M. Heller, J. P. Torre, and C. N. Peille, "Mechanical properties and short-term in vivo evaluation of yttrium-oxide-partially-stabilized zirconia," *Journal of Biomedical Materials Research,* vol. 23, no. 1, pp. 45-61, Jan. 1989, doi: https://doi.org/10.1002/jbm.820230105.

[35] A. G. Gebresilassie, "Atomic scale simulations in zirconia: Effect of yttria doping and environment on stability of phases," PhD Thesis, Doctoral school of materials of Lyon, University of Lyon, Villeurbanne, France, 2019. [Online]. Available: https://www.sudoc.fr/24109320

[36] K. Boobalan, R. Vijayaraghavan, K. Chidambaram, U. M. K. Mudali, and B. Raj, "Preparation and Characterization of Nanocrystalline Zirconia Powders by the Glowing Combustion Method," *Journal of the American Ceramic Society,* vol. 93, no. 11, pp. 3651-3656, Nov. 2010, doi: https://doi.org/10.1111/j.1551-2916.2010.03947.x.

[37] J. R. Kelly and I. Denry, "Stabilized zirconia as a structural ceramic: An overview," *Dental Materials,* vol. 24, no. 3, pp. 289-298, Mar. 2008, doi: https://doi.org/10.1016/j.dental.2007.05.005.

[38] R. F. L. d. Santos, "Síntese de nanopartículas de zircónia por estratégias SSP (soft solution processing," Master Dissertation, Chemical Engineering, University of Coimbra, Coimbra, Portugal, 2014. [Online]. Available: https://estudogeral.sib.uc.pt/bitstream/10316/40228/1/Sintese%20de%20nanoparticulas%20de%20zirconia%20por%20estrategias%20de%20processamento%20em%20solucao.pdf

[39] J. Vleugels, Z. X. Yuan, and O. Van Der Biest, "Mechanical properties of Y_2O_3/Al_2O_3-coated Y-TZP ceramics," *Journal of the European Ceramic Society,* vol. 22, no. 6, pp. 873-881, Jun. 2002, doi: https://doi.org/10.1016/S0955-2219(01)00389-2.

[40] B. S. Vasile *et al.*, "Microstructure and electrical properties of zirconia and composite nanostructured ceramics sintered by different methods," *Ceramics International,* vol. 39, no. 3, pp. 2535-2543, Apr. 2013, doi: https://doi.org/10.1016/j.ceramint.2012.09.013.

[41] L. L. Hench, "Bioceramics," *Journal of the American Ceramic Society,* vol. 81, no. 7, pp. 1705-1728, Jul. 1998, doi: https://doi.org/10.1111/j.1151-2916.1998.tb02540.x.

[42] A. Noiri, F. Hoshi, H. Murakami, K. Sato, S. I. Kawai, and K. Kawai, "Biocompatibility of a mobile alumina-ceramic orbital implant," *Folia Ophthalmologica Japonica,* vol. 53, pp. 476-480, Jan. 2002. [Online]. Available: https://www.researchgate.net/publication/289131406_Biocompatibility_of_a_mobile_alumina-ceramic_orbital_implant.

[43] C. S. Delfino, C. Ribeiro, G. F. Vieira, A. H. A. Bressiani, and M. L. Turbino, "Uso de novos materiais para o capeamento pulpar (hidroxiapatita - HAp e fosfato tricálcico - β-TCP)," *Cerâmica,* vol. 56, no. 340, pp. 381-388, Dec. 2010, doi: https://doi.org/10.1590/S0366-69132010000400011.

[44] M. Frasnelli and V. M. Sglavo, "Effect of Mg^{2+} doping on beta–alpha phase transition in tricalcium phosphate (TCP) bioceramics," *Acta Biomaterialia,* vol. 33, pp. 283-289, Mar. 2016, doi: https://doi.org/10.1016/j.actbio.2016.01.015.

[45] S. V. Dorozhkin, "Self-Setting Calcium Orthophosphate Formulations: Cements, Concretes, Pastes and Putties," *International Journal of Materials and Chemistry,* vol. 1, no. 1, pp. 1-48, 2011, doi: https://doi.org/10.5923/j.ijmc.20110101.01.

[46] F. Baino, S. Caddeo, G. Novajra, and C. Vitale-Brovarone, "Using porous bioceramic scaffolds to model healthy and osteoporotic bone," *Journal of the European Ceramic Society,* vol. 36, no. 9, pp. 2175-2182, Aug. 2016, doi: https://doi.org/10.1016/j.jeurceramsoc.2016.01.011.

[47] C. Vitale-Brovarone *et al.*, "Development of glass–ceramic scaffolds for bone tissue engineering: Characterisation, proliferation of human osteoblasts and nodule formation," *Acta Biomaterialia,* vol. 3, no. 2, pp. 199-208, Mar. 2007, doi: https://doi.org/10.1016/j.actbio.2006.07.012.

[48] S. Wu, X. Liu, K. W. K. Yeung, C. Liu, and X. Yang, "Biomimetic porous scaffolds for bone tissue engineering," *Materials Science and Engineering: R: Reports,* vol. 80, pp. 1-36, Jun. 2014, doi: https://doi.org/10.1016/j.mser.2014.04.001.

[49] J. Ran *et al.*, "Comparisons among Mg, Zn, Sr, and Si doped nano-hydroxyapatite/chitosan composites for load-bearing bone tissue engineering applications," *Materials Chemistry Frontiers,* 10.1039/C6QM00192K vol. 1, no. 5, pp. 900-910, May. 2017, doi: https://doi.org/10.1039/C6QM00192K.

[50] H. Yuan *et al.*, "Osteoinductive ceramics as a synthetic alternative to autologous bone grafting," *Proceedings of the National Academy of Sciences,* vol. 107, no. 31, pp. 13614-13619, Jul. 2010, doi: https://doi.org/doi:10.1073/pnas.1003600107.

[51] D. F. Macedo and A. P. Silva, "Analysis of the effect of doped metal ions in the tricalcium phosphate bioceramic," *Journal of Physics: Conference Series,* vol. 1960, no. 1, p. 012014, Jun. 2021, doi: https://doi.org/10.1088/1742-6596/1960/1/012014.

[52] S.-H. Kwon, Y.-K. Jun, S.-H. Hong, and H.-E. Kim, "Synthesis and dissolution behavior of β-TCP and HA/β-TCP composite powders," *Journal of the European Ceramic Society,* vol. 23, no. 7, pp. 1039-1045, Jun. 2003, doi: https://doi.org/10.1016/S0955-2219(02)00263-7.

[53] M. Alcaide, M.-C. Serrano, R. Pagani, S. Sánchez-Salcedo, M. Vallet-Regí, and M.-T. Portolés, "Biocompatibility markers for the study of interactions between osteoblasts and composite biomaterials," *Biomaterials,* vol. 30, no. 1, pp. 45-51, Jan. 2009, doi: https://doi.org/10.1016/j.biomaterials.2008.09.012.

[54] M. Yashima and A. Sakai, "High-temperature neutron powder diffraction study of the structural phase transition between α and α′ phases in tricalcium phosphate $Ca_3(PO_4)_2$," *Chemical Physics Letters,* vol. 372, no. 5, pp. 779-783, May. 2003, doi: https://doi.org/10.1016/S0009-2614(03)00505-0.

[55] M. Mathew, L. W. Schroeder, B. Dickens, and W. E. Brown, "The crystal structure of α-$Ca_3(PO_4)_2$," *Acta Crystallographica Section B,* vol. 33, no. 5, pp. 1325-1333, May. 1977, doi: https://doi.org/doi:10.1107/S0567740877006037.

[56] N. Döbelin, L. Galea, U. Eggenberger, J. M. d. F. Ferreira, and M. Bohner, "Recrystallization of Amorphized α-TCP," *Key Engineering Materials,* vol. 493-494, pp. 219-224, Oct. 2012, doi: https://doi.org/10.4028/www.scientific.net/KEM.493-494.219.

[57] H.-S. Ryu, H.-J. Youn, K. Sun Hong, B.-S. Chang, C.-K. Lee, and S.-S. Chung, "An improvement in sintering property of β-tricalcium phosphate by addition of calcium pyrophosphate," *Biomaterials,* vol. 23, no. 3, pp. 909-914, Feb. 2002, doi: https://doi.org/10.1016/S0142-9612(01)00201-0.

[58] H. Monma and M. Goto, "Behavior of the α⇄β phase transformation in tricalcium phosphate," 1983. [Online]. Available: https://api.semanticscholar.org/CorpusID:102481630.

[59] R. Enderle, F. Götz-Neunhoeffer, M. Göbbels, F. A. Müller, and P. Greil, "Influence of magnesium doping on the phase transformation temperature of β-TCP ceramics examined by Rietveld refinement," *Biomaterials,* vol. 26, no. 17, pp. 3379-3384, Jun. 2005, doi: https://doi.org/10.1016/j.biomaterials.2004.09.017.

[60] D. Arcos and M. Vallet-Regí, "Substituted hydroxyapatite coatings of bone implants," *Journal of Materials Chemistry B,* 10.1039/C9TB02710F vol. 8, no. 9, pp. 1781-1800, Feb 2020, doi: https://doi.org/10.1039/C9TB02710F.

[61] S. S. Banerjee, S. Tarafder, N. M. Davies, A. Bandyopadhyay, and S. Bose, "Understanding the influence of MgO and SrO binary doping on the mechanical and biological properties of β-TCP ceramics," *Acta Biomaterialia,* vol. 6, no. 10, pp. 4167-4174, Oct. 2010, doi: https://doi.org/10.1016/j.actbio.2010.05.012.

[62] S. Bose, S. Tarafder, S. S. Banerjee, N. M. Davies, and A. Bandyopadhyay, "Understanding in vivo response and mechanical property variation in MgO, SrO and SiO_2 doped β-TCP," *Bone,* vol. 48, no. 6, pp. 1282-1290, Jun. 2011, doi: https://doi.org/10.1016/j.bone.2011.03.685.

[63] H.-S. Ryu *et al.*, "Magnesia-doped HA/β-TCP ceramics and evaluation of their biocompatibility," *Biomaterials,* vol. 25, no. 3, pp. 393-401, Feb. 2004, doi: https://doi.org/10.1016/S0142-9612(03)00538-6.

[64] L. Sinusaite *et al.*, "Effect of Mn doping on the low-temperature synthesis of tricalcium phosphate (TCP) polymorphs," *Journal of the European Ceramic Society,* vol. 39, no. 10, pp. 3257-3263, Aug. 2019, doi: https://doi.org/10.1016/j.jeurceramsoc.2019.03.057.

[65] K. P. Ananth, J. Sun, and J. Bai, "An Innovative Approach to Manganese-Substituted Hydroxyapatite Coating on Zinc Oxide–Coated 316L SS for Implant Application," *International Journal of Molecular Sciences,* vol. 19, no. 8, p. 2340, Aug. 2018, doi: https://doi.org/doi:10.3390/ijms19082340.

[66] Y.-J. Chou, H. S. Ningsih, and S.-J. Shih, "Preparation, characterization and investigation of antibacterial silver-zinc co-doped β-tricalcium phosphate by spray pyrolysis," *Ceramics International,* vol. 46, no. 10, Part B, pp. 16708-16715, Jul. 2020, doi: https://doi.org/10.1016/j.ceramint.2020.03.245.

[67] A. V. Lyasnikova, O. A. Dudareva, V. N. Lyasnikov, O. A. Markelova, and I. P. Grishina, "Comparative Analysis of Plasma Bioceramic Coatings Based on Zinc-Substituted Hydroxyapatite and Tricalcium Phosphate," *Glass and Ceramics,* vol. 75, no. 3, pp. 163-167, Jul. 2018, doi: https://doi.org/10.1007/s10717-018-0048-z.

[68] M. Mirak, M. Alizadeh, M. Ghaffari, and M. N. Ashtiani, "Characterization, mechanical properties and corrosion resistance of biocompatible Zn-HA/TiO_2 nanocomposite

coatings," *Journal of the Mechanical Behavior of Biomedical Materials,* vol. 62, pp. 282-290, Sep. 2016, doi: https://doi.org/10.1016/j.jmbbm.2016.05.016.

[69] V. M. Ferro, B. C. Silva, D. F. Macedo, N. F. Fernandes, and A. P. Silva, "TCP Doped with Metal Ions Reinforced with Tetragonal and Cubic Zirconia," *Biomimetics,* vol. 8, no. 8, p. 599, Dec. 2023, doi: https://doi.org/doi:10.3390/biomimetics8080599.

[70] S. Vahabzadeh and S. Bose, "Effects of Iron on Physical and Mechanical Properties, and Osteoblast Cell Interaction in β-Tricalcium Phosphate," *Annals of Biomedical Engineering,* vol. 45, no. 3, pp. 819-828, Feb. 2017, doi: https://doi.org/10.1007/s10439-016-1724-1.

[71] M. Mabrouk, S. M. Mousa, W. A. A. ElGhany, M. T. Abo-elfadl, and G. T. El-Bassyouni, "Bioactivity and cell viability of Ag+- and Zr4+-co-doped biphasic calcium phosphate," *Applied Physics A,* vol. 127, no. 12, p. 948, Nov. 2021, doi: https://doi.org/10.1007/s00339-021-05051-1.

[72] C. F. Marques *et al.*, "Biocompatibility and antimicrobial activity of biphasic calcium phosphate powders doped with metal ions for regenerative medicine," *Ceramics International,* vol. 43, no. 17, pp. 15719-15728, Dec. 2017, doi: https://doi.org/10.1016/j.ceramint.2017.08.133.

[73] N. Matsumoto, K. Yoshida, K. Hashimoto, and Y. Toda, "Thermal stability of β-tricalcium phosphate doped with monovalent metal ions," *Materials Research Bulletin,* vol. 44, no. 9, pp. 1889-1894, Sep. 2009, doi: https://doi.org/10.1016/j.materresbull.2009.05.012.

[74] C. Q. Zhao *et al.*, "Doping lithium element to enhance compressive strength of β-TCP scaffolds manufactured by 3D printing for bone tissue engineering," *Journal of Alloys and Compounds,* vol. 814, p. 152327, Jan. 2020, doi: https://doi.org/10.1016/j.jallcom.2019.152327.

[75] L. Obadia *et al.*, "Na-doped β-tricalcium phosphate: physico-chemical and in vitro biological properties," *Journal of Materials Science: Materials in Medicine,* vol. 22, no. 3, pp. 593-600, Mar. 2011, doi: https://doi.org/10.1007/s10856-010-4219-x.

[76] B. Singh, S. Kumar, B. Basu, and R. Gupta, "Conductivity Studies of Silver-, Potassium-, and Magnesium-Doped Hydroxyapatite," *International Journal of Applied Ceramic Technology,* vol. 12, no. 2, pp. 319-328, Aug. 2015, doi: https://doi.org/10.1111/ijac.12167.

[77] P. S. Gomes, C. Botelho, M. A. Lopes, J. D. Santos, and M. H. Fernandes, "Effect of silicon-containing hydroxyapatite coatings on the human in vitro osteoblastic response," *Bone,* vol. 44, p. S267, Jun. 2009, doi: https://doi.org/10.1016/j.bone.2009.03.464.

[78] J. R. Jones, O. Tsigkou, E. E. Coates, M. M. Stevens, J. M. Polak, and L. L. Hench, "Extracellular matrix formation and mineralization on a phosphate-free porous bioactive glass scaffold using primary human osteoblast (HOB) cells," *Biomaterials,* vol. 28, no. 9, pp. 1653-1663, Mar. 2007, doi: https://doi.org/10.1016/j.biomaterials.2006.11.022.

[79] A. Bandyopadhyay, J. Petersen, G. Fielding, S. Banerjee, and S. Bose, "ZnO, SiO_2, and SrO doping in resorbable tricalcium phosphates: Influence on strength degradation, mechanical properties, and in vitro bone–cell material interactions," *Journal of Biomedical Materials Research Part B: Applied Biomaterials,* vol. 100B, no. 8, pp. 2203-2212, Nov. 2012, doi: https://doi.org/10.1002/jbm.b.32789.

[80] N. Matsumoto, K. Sato, K. Yoshida, K. Hashimoto, and Y. Toda, "Preparation and characterization of β-tricalcium phosphate co-doped with monovalent and divalent antibacterial metal ions," *Acta Biomaterialia,* vol. 5, no. 8, pp. 3157-3164, Oct. 2009, doi: https://doi.org/10.1016/j.actbio.2009.04.010.

[81] A. Tahmasebifar and Z. Evis, "Structural and mechanical characteristics of hydroxyapatite and tri-calcium phosphates doped with Al^{3+} and F^- ions," *Journal of Ceramic Processing Research.,* vol. 14, pp. 549-556, 08/01 2013. [Online]. Available: https://www.researchgate.net/publication/267607149_Structural_and_mechanical_characteristics_of_hydroxyapatite_and_tri-calcium_phosphates_doped_with_Al3_and_F-_ions.

[82] M. Turkoz, A. O. Atilla, and Z. Evis, "Silver and fluoride doped hydroxyapatites: Investigation by microstructure, mechanical and antibacterial properties," *Ceramics International,* vol. 39, no. 8, pp. 8925-8931, Dec. 2013, doi: https://doi.org/10.1016/j.ceramint.2013.04.088.

[83] I. Kutbay, B. Yilmaz, Z. Evis, and M. Usta, "Effect of calcium fluoride on mechanical behavior and sinterability of nano-hydroxyapatite and titania composites," *Ceramics International,* vol. 40, no. 9, Part B, pp. 14817-14826, Nov. 2014, doi: https://doi.org/10.1016/j.ceramint.2014.06.075.

[84] M. A. Goldberg *et al.*, "The enhancement of hydroxyapatite thermal stability by Al doping," *Journal of Materials Research and Technology,* vol. 9, no. 1, pp. 76-88, Jan. 2020, doi: https://doi.org/10.1016/j.jmrt.2019.10.032.

[85] O. Z. Andersen *et al.*, "Accelerated bone ingrowth by local delivery of strontium from surface functionalized titanium implants," *Biomaterials,* vol. 34, no. 24, pp. 5883-5890, Aug. 2013, doi: https://doi.org/10.1016/j.biomaterials.2013.04.031.

[86] V. K. Dommeti, S. Roy, S. Pramanik, A. Merdji, A. Ouldyerou, and M. Özcan, "Design and Development of Tantalum and Strontium Ion Doped Hydroxyapatite Composite Coating

on Titanium Substrate: Structural and Human Osteoblast-like Cell Viability Studies," *Materials,* vol. 16, no. 4, p. 1499, Feb. 2023, doi: https://doi.org/doi:10.3390/ma16041499.

[87] R. Rizzoli and J.-Y. Reginster, "Adverse drug reactions to osteoporosis treatments," *Expert Review of Clinical Pharmacology,* vol. 4, no. 5, pp. 593-604, Sep. 2011, doi: https://doi.org/10.1586/ecp.11.42.

[88] C. Cai *et al.*, "Fabrication of Hydroxyapatite/Tantalum Composites by Pressureless Sintering in Different Atmosphere," *ACS Omega,* vol. 6, no. 19, pp. 12831-12840, May. 2021, doi: https://doi.org/10.1021/acsomega.1c01205.

[89] S. Baradaran, B. Nasiri-Tabrizi, F. S. Shirazi, S. Saber-Samandari, S. Shahtalebi, and W. J. Basirun, "Wet chemistry approach to the preparation of tantalum-doped hydroxyapatite: Dopant content effects," *Ceramics International,* vol. 44, no. 3, pp. 2768-2781, Feb. 2018, doi: https://doi.org/10.1016/j.ceramint.2017.11.016.

[90] T. Gray, N. Mann, and M. Whitby. "Atomic Radius of the elements." periodictable.com. https://periodictable.com/Properties/A/AtomicRadius.v.html (accessed May. 10, 2024).

[91] S. Ligot, T. Godfroid, D. Music, E. Bousser, J. M. Schneider, and R. Snyders, "Tantalum-doped hydroxyapatite thin films: Synthesis and characterization," *Acta Materialia,* vol. 60, no. 8, pp. 3435-3443, May. 2012, doi: https://doi.org/10.1016/j.actamat.2012.02.024.

[92] M. A. Zoroddu, J. Aaseth, G. Crisponi, S. Medici, M. Peana, and V. M. Nurchi, "The essential metals for humans: a brief overview," *Journal of Inorganic Biochemistry,* vol. 195, pp. 120-129, Jun. 2019, doi: https://doi.org/10.1016/j.jinorgbio.2019.03.013.

[93] J. H. F. de Baaij, J. G. J. Hoenderop, and R. J. M. Bindels, "Magnesium in Man: Implications for Health and Disease," *Physiological Reviews,* vol. 95, no. 1, pp. 1-46, Jan. 2015, doi: https://doi.org/10.1152/physrev.00012.2014.

[94] J. Rodríguez and P. M. Mandalunis, "A Review of Metal Exposure and Its Effects on Bone Health," *Journal of Toxicology,* vol. 2018, no. 1, p. 4854152, Dec. 2018, doi: https://doi.org/10.1155/2018/4854152.

[95] The National Institute for Occupational Safety and Health (NIOSH). "Zirconium compounds (as Zr)." Centers for Disease Control and Prevention (CDC). https://www.cdc.gov/niosh/npg/npgd0677.html (accessed Sep. 29, 2024).

[96] D. B. N. Lee, M. Roberts, C. G. Bluchel, and R. A. Odell, "Zirconium: Biomedical and Nephrological Applications," *ASAIO Journal,* vol. 56, no. 6, pp. 550-556, Nov. 2010, doi: https://doi.org/10.1097/MAT.0b013e3181e73f20.

[97] WebMD. "Iron - Uses, Side Effects, and More." WebMD. https://www.webmd.com/vitamins/ai/ingredientmono-912/iron (accessed Sep. 29, 2024).

[98] K. Mijnendonckx, N. Leys, J. Mahillon, S. Silver, and R. Van Houdt, "Antimicrobial silver: uses, toxicity and potential for resistance," *BioMetals,* vol. 26, no. 4, pp. 609-621, Aug. 2013, doi: https://doi.org/10.1007/s10534-013-9645-z.

[99] S. L. Gaetani, A. M. Amaducci, D. Fikse, and A. L. Koons, "Lithium Toxicity: A Case Report of Toxicity Resulting in a Third-degree Heart Block," *Clinical Practice and Cases in Emergency Medicine,* vol. 8, no. 1, Jan. 2024, doi: https://doi.org/10.5811/cpcem.1442.

[100] Cleveland Clinic. "Lithium Toxicity." Cleaveland Clinic. https://my.clevelandclinic.org/health/diseases/25207-lithium-toxicity (accessed May. 17, 2024).

[101] Harvard School of Public Health. "Salt and Sodium." Harvard School of Public Health. https://nutritionsource.hsph.harvard.edu/salt-and-sodium/ (accessed May. 17, 2024).

[102] Cleveland Clinic. "Hyperkalemia (High Potassium)." Cleveland Clinic. https://my.clevelandclinic.org/health/diseases/15184-hyperkalemia-high-blood-potassium (accessed May. 17, 2024).

[103] N. Douard, R. Detsch, R. Chotard-Ghodsnia, C. Damia, U. Deisinger, and E. Champion, "Processing, physico-chemical characterisation and in vitro evaluation of silicon containing β-tricalcium phosphate ceramics," *Materials Science and Engineering: C,* vol. 31, no. 3, pp. 531-539, Apr. 2011, doi: https://doi.org/10.1016/j.msec.2010.11.008.

[104] Lenntech. "Silicon - Si." Lenntech. https://www.lenntech.com/periodic/elements/si.htm (accessed May. 17, 2024).

[105] T. Bazin *et al.*, "Sintering and biocompatibility of copper-doped hydroxyapatite bioceramics," *Ceramics International,* vol. 47, no. 10, Part A, pp. 13644-13654, May. 2021, doi: https://doi.org/10.1016/j.ceramint.2021.01.225.

[106] N. R. Johnston and S. A. Strobel, "Principles of fluoride toxicity and the cellular response: a review," *Archives of Toxicology,* vol. 94, no. 4, pp. 1051-1069, Apr. 2020, doi: https://doi.org/10.1007/s00204-020-02687-5.

[107] D. M. O'Mullabe *et al.*, "Fluoride and Oral Health," *Community Dental Health,* vol. 33, no. 2, pp. 69-99, Jun. 2016, doi: https://doi.org/10.1922/CDH_3707O'Mullane31.

[108] M. R. Rahimzadeh, M. R. Rahimzadeh, S. Kazemi, R. J. Amiri, M. Pirzadeh, and A. A. Moghadamnia, "Aluminum Poisoning with Emphasis on Its Mechanism and Treatment of Intoxication," *Emergency Medicine International,* vol. 2022, no. 1, p. 1480553, Jan. 2022, doi: https://doi.org/10.1155/2022/1480553.

[109] W. Zhang *et al.*, "Effects of strontium in modified biomaterials," *Acta Biomaterialia,* vol. 7, no. 2, pp. 800-808, Feb. 2011, doi: https://doi.org/10.1016/j.actbio.2010.08.031.

[110] R. Amata, L. G. Diamond, A. Dorsey, and E. M. Fransen, "Toxicological Profile for Strontium," U.S. Dept. of Health and Human Services, Public Health Service, Agency for Toxic Substances and Disease Registry, Atlanta, GA, Apr. 2004. [Online]. Available: https://stacks.cdc.gov/view/cdc/6550/cdc_6550_DS1.pdf

[111] S. C. Kerwien, "Toxicity of Tungsten, Molybdenum, and Tantalum and the Environmental and Occupational Laws Associated with their Manufacture, Use, and Disposal," Army Armament Research Development and Engineering Center Picatinny Arsenal N J Armament Engineering Directorate, Picatinny Arsenal, NJ, Jun. 1996. [Online]. Available: https://apps.dtic.mil/sti/pdfs/ADA310298.pdf

[112] Q. Fu, E. Saiz, M. N. Rahaman, and A. P. Tomsia, "Toward Strong and Tough Glass and Ceramic Scaffolds for Bone Repair," *Advanced Functional Materials,* vol. 23, no. 44, pp. 5461-5476, Nov. 2013, doi: https://doi.org/10.1002/adfm.201301121.

[113] Y.-H. Lee, J.-W. Lee, S.-Y. Yang, H. Lee, Y.-H. Koh, and H.-E. Kim, "Dual-scale porous biphasic calcium phosphate gyroid scaffolds using ceramic suspensions containing polymer microsphere porogen for digital light processing," *Ceramics International,* vol. 47, no. 8, pp. 11285-11293, Apr. 2021, doi: https://doi.org/10.1016/j.ceramint.2020.12.254.

[114] Y. Sa, F. Yang, J. R. de Wijn, Y. Wang, J. G. C. Wolke, and J. A. Jansen, "Physicochemical properties and mineralization assessment of porous polymethylmethacrylate cement loaded with hydroxyapatite in simulated body fluid," *Materials Science and Engineering: C,* vol. 61, pp. 190-198, Apr. 2016, doi: https://doi.org/10.1016/j.msec.2015.12.040.

[115] M. Shi *et al.*, "Antibiotic-releasing porous polymethylmethacrylate constructs for osseous space maintenance and infection control," *Biomaterials,* vol. 31, no. 14, pp. 4146-4156, May. 2010, doi: https://doi.org/10.1016/j.biomaterials.2010.01.112.

[116] I.-G. Kang, C.-I. Park, H. Lee, H.-E. Kim, and S.-M. Lee, "Hydroxyapatite Microspheres as an Additive to Enhance Radiopacity, Biocompatibility, and Osteoconductivity of Poly(methyl methacrylate) Bone Cement," *Materials,* vol. 11, no. 2, p. 258, Feb. 2018, doi: https://doi.org/doi:10.3390/ma11020258.

[117] M. Jäger and A. Wilke, "Comprehensive biocompatibility testing of a new PMMA-HA bone cement versus conventional PMMA cement in vitro," *Journal of Biomaterials Science, Polymer Edition,* vol. 14, no. 11, pp. 1283-1298, Jan. 2003, doi: https://doi.org/10.1163/156856203322553491.

[118] S. Saha and S. Pal, "Mechanical properties of bone cement: A review," *Journal of Biomedical Materials Research,* vol. 18, no. 4, pp. 435-462, Apr. 1984, doi: https://doi.org/10.1002/jbm.820180411.

[119] M. Descamps *et al.*, "Manufacture of macroporous β-tricalcium phosphate bioceramics," *Journal of the European Ceramic Society,* vol. 28, no. 1, pp. 149-157, Jan. 2008, doi: https://doi.org/10.1016/j.jeurceramsoc.2007.05.025.

[120] A. Sugino, T. Miyazaki, G. Kawachi, K. Kikuta, and C. Ohtsuki, "Relationship between apatite-forming ability and mechanical properties of bioactive PMMA-based bone cement modified with calcium salts and alkoxysilane," *Journal of Materials Science: Materials in Medicine,* vol. 19, no. 3, pp. 1399-1405, Mar. 2008, doi: https://doi.org/10.1007/s10856-007-3257-5.

[121] M. P. Ginebra *et al.*, "Mechanical performance of acrylic bone cements containing different radiopacifying agents," *Biomaterials,* vol. 23, no. 8, pp. 1873-1882, Apr. 2002, doi: https://doi.org/10.1016/S0142-9612(01)00314-3.

[122] G. V. Franks, C. Tallon, A. R. Studart, M. L. Sesso, and S. Leo, "Colloidal processing: enabling complex shaped ceramics with unique multiscale structures," *Journal of the American Ceramic Society,* vol. 100, no. 2, pp. 458-490, Feb. 2017, doi: https://doi.org/10.1111/jace.14705.

[123] P. Colombo, "Conventional and novel processing methods for cellular ceramics," *Philosophical Transactions of the Royal Society A: Mathematical, Physical and Engineering Sciences,* vol. 364, no. 1838, pp. 109-124, Jan. 2006, doi: https://doi.org/doi:10.1098/rsta.2005.1683.

[124] X. Xiao *et al.*, "The promotion of angiogenesis induced by three-dimensional porous beta-tricalcium phosphate scaffold with different interconnection sizes via activation of PI3K/Akt pathways," *Scientific Reports,* vol. 5, no. 1, p. 9409, Mar. 2015, doi: https://doi.org/10.1038/srep09409.

[125] B. Flautre, M. Descamps, C. Delecourt, M. C. Blary, and P. Hardouin, "Porous HA ceramic for bone replacement: Role of the pores and interconnections – experimental study in the rabbit," *Journal of Materials Science: Materials in Medicine,* vol. 12, no. 8, pp. 679-682, Aug. 2001, doi: https://doi.org/10.1023/A:1011256107282.

[126] J. J. Klawitter, J. G. Bagwell, A. M. Weinstein, B. W. Sauer, and J. R. Pruitt, "An evaluation of bone growth into porous high density polyethylene," *Journal of Biomedical Materials Research,* vol. 10, no. 2, pp. 311-323, Mar. 1976, doi: https://doi.org/10.1002/jbm.820100212.

[127] J. X. Lu *et al.*, "Role of interconnections in porous bioceramics on bone recolonization in vitro and in vivo," *Journal of Materials Science: Materials in Medicine,* vol. 10, no. 2, pp. 111-120, Feb 1999, doi: https://doi.org/10.1023/A:1008973120918.

[128] T. M. Freyman, I. V. Yannas, and L. J. Gibson, "Cellular materials as porous scaffolds for tissue engineering," *Progress in Materials Science,* vol. 46, no. 3, pp. 273-282, Jan. 2001, doi: https://doi.org/10.1016/S0079-6425(00)00018-9.

[129] S. Pollick, E. C. Shors, R. E. Holmes, and R. A. Kraut, "Bone formation and implant degradation of coralline porous ceramics placed in bone and ectopic sites," *Journal of Oral and Maxillofacial Surgery,* vol. 53, no. 8, pp. 915-922, Aug. 1995, doi: https://doi.org/10.1016/0278-2391(95)90281-3.

[130] S. Tarafder, N. M. Davies, A. Bandyopadhyay, and S. Bose, "3D printed tricalcium phosphate bone tissue engineering scaffolds: effect of SrO and MgO doping on in vivo osteogenesis in a rat distal femoral defect model," *Biomaterials Science,* https://doi.org/10.1039/C3BM60132C vol. 1, no. 12, pp. 1250-1259, Aug. 2013, doi: 10.1039/C3BM60132C.

[131] C. Vitale-Brovarone, S. D. Nunzio, O. Bretcanu, and E. Verné, "Macroporous glass-ceramic materials with bioactive properties," *Journal of Materials Science: Materials in Medicine,* vol. 15, no. 3, pp. 209-217, Mar. 2004, doi: https://doi.org/10.1023/B:JMSM.0000015480.49061.e1.

[132] F. Baino, E. Verné, and C. Vitale-Brovarone, "3-D high-strength glass–ceramic scaffolds containing fluoroapatite for load-bearing bone portions replacement," *Materials Science and Engineering: C,* vol. 29, no. 6, pp. 2055-2062, Aug. 2009, doi: https://doi.org/10.1016/j.msec.2009.04.002.

[133] F. Baino and C. Vitale-Brovarone, "Mechanical properties and reliability of glass–ceramic foam scaffolds for bone repair," *Materials Letters,* vol. 118, pp. 27-30, Mar. 2014, doi: https://doi.org/10.1016/j.matlet.2013.12.037.

[134] S. Izman *et al.*, "Surface Modification Techniques for Biomedical Grade of Titanium Alloys: Oxidation, Carburization and Ion Implantation Processes," in *Titanium Alloys*, A. K. M. N. Amin Ed. Rijeka: IntechOpen, 2012, p. Ch. 9.

[135] M. Takeuchi, Y. Abe, Y. Yoshida, Y. Nakayama, M. Okazaki, and Y. Akagawa, "Acid pretreatment of titanium implants," *Biomaterials,* vol. 24, no. 10, pp. 1821-1827, May. 2003, doi: https://doi.org/10.1016/S0142-9612(02)00576-8.

[136] G. W. Critchlow and D. M. Brewis, "Review of surface pretreatments for titanium alloys," *International Journal of Adhesion and Adhesives,* vol. 15, no. 3, pp. 161-172, Jul. 1995, doi: https://doi.org/10.1016/0143-7496(95)91627-I.

[137] M. Yan, C.-T. Kao, J.-S. Ye, T.-H. Huang, and S.-J. Ding, "Effect of preoxidation of titanium on the titanium–ceramic bonding," *Surface and Coatings Technology,* vol. 202, no. 2, pp. 288-293, Nov. 2007, doi: https://doi.org/10.1016/j.surfcoat.2007.05.056.

[138] P. Jonsén, H. Å. Häggblad, and K. Sommer, "Tensile strength and fracture energy of pressed metal powder by diametral compression test," *Powder Technology,* vol. 176, no. 2, pp. 148-155, Jul. 2007, doi: https://doi.org/10.1016/j.powtec.2007.02.030.

[139] J. L. A. Albaro, "A Operação de Prensagem: Considerações Técnicas e sua Aplicação Industrial. Parte V: Descrição da Etapa de Prensagem," *Cerâmica Industrial,* vol. 6, no. 3, pp. 26-32, 2001. [Online]. Available: https://www.ceramicaindustrial.org.br/article/5876570c7f8c9d6e028b4649.

[140] F. Thümmler and W. Thomma, "The sintering process," *Metallurgical Reviews,* vol. 12, no. 1, pp. 69-108, Jan. 1967, doi: https://doi.org/10.1179/mtlr.1967.12.1.69.

[141] *Standart Test Method for Drying and Firing Linear Change of Refractory Plastic and Ramming Mix Specimens*, ASTM, 2004. [Online]. Available: https://www.astm.org/c0179-04.html

[142] *Standard Test Methods for Apparent Porosity, Water Absorption, Apparent Specific Gravity, and Bulk Density of Burned Refractory Brick and Shapes by Boiling Water*, ASTM, 2004. [Online]. Available: https://www.astm.org/c0179-04.html

[143] M. Ferreira, "Impulsão e Lei de Arquimedes," *Revista de ciência elementar,* vol. 2, no. 4, p. 2, Dec. 2014, doi: http://doi.org/10.24927/rce2014.074.

[144] E. Martin, D. Leguillon, O. Sevecek, and R. Bermejo, "Understanding the tensile strength of ceramics in the presence of small critical flaws," *Engineering Fracture Mechanics,* vol. 201, pp. 167-175, Oct. 2018, doi: https://doi.org/10.1016/j.engfracmech.2018.06.021.

[145] V. P. Efimov, "Brazilian Tensile Strength Testing," *Journal of Mining Science,* vol. 57, no. 6, pp. 922-932, Nov. 2021, doi: https://doi.org/10.1134/S1062739121060053.

[146] G. R. Anstis, P. Chantikul, B. R. Lawn, and D. B. Marshall, "A Critical Evaluation of Indentation Techniques for Measuring Fracture Toughness: I, Direct Crack

Measurements," *Journal of the American Ceramic Society,* vol. 64, no. 9, pp. 533-538, Sep. 1981, doi: https://doi.org/10.1111/j.1151-2916.1981.tb10320.x.

[147] A. Tricoteaux *et al.*, "Influence of porosity on the mechanical properties of microporous β-TCP bioceramics by usual and instrumented Vickers microindentation," *Journal of the European Ceramic Society,* vol. 31, no. 8, pp. 1361-1369, Jul. 2011, doi: https://doi.org/10.1016/j.jeurceramsoc.2011.02.005.

[148] E. S. Ameh, "A review of basic crystallography and x-ray diffraction applications," *The International Journal of Advanced Manufacturing Technology,* vol. 105, no. 7, pp. 3289-3302, Dec. 2019, doi: https://doi.org/10.1007/s00170-019-04508-1.

[149] A. Abdullah and A. Mohammed, "Scanning Electron Microscopy (SEM): A Review," presented at the Proceedings of 2018 International Conference on Hydraulics and Pneumatics - HERVEX, Băile Govora, Romania Nov., 2019. [Online]. Available: https://www.researchgate.net/publication/330169176_Scanning_Electron_Microscopy_SEM_A_Review.

[150] T. Sipos and J. R. Merkel, "Effect of calcium ions on the activity, heat stability, and structure of trypsin," *Biochemistry,* vol. 9, no. 14, pp. 2766-2775, Jul. 1970, doi: https://doi.org/10.1021/bi00816a003.

[151] J. O'Brien, I. Wilson, T. Orton, and F. Pognan, "Investigation of the Alamar Blue (resazurin) fluorescent dye for the assessment of mammalian cell cytotoxicity," *European Journal of Biochemistry,* vol. 267, no. 17, pp. 5421-5426, Sep. 2000, doi: https://doi.org/10.1046/j.1432-1327.2000.01606.x.

[152] R. S. Sequeira, S. P. Miguel, C. S. D. Cabral, A. F. Moreira, P. Ferreira, and I. J. Correia, "Development of a poly(vinyl alcohol)/lysine electrospun membrane-based drug delivery system for improved skin regeneration," *International Journal of Pharmaceutics,* vol. 570, p. 118640, Oct. 2019, doi: https://doi.org/10.1016/j.ijpharm.2019.118640.

[153] N. Fernandes, C. F. Rodrigues, D. de Melo-Diogo, I. J. Correia, and A. F. Moreira, "Optimization of the GSH-Mediated Formation of Mesoporous Silica-Coated Gold Nanoclusters for NIR Light-Triggered Photothermal Applications," *Nanomaterials,* vol. 11, no. 8, p. 1946, Jul. 2021, doi: https://doi.org/doi:10.3390/nano11081946.

[154] V. Morath. "File:48-well-plate.svg." Volker-Morath. https://commons.wikimedia.org/wiki/File:48-well-plate.svg (accessed Jul. 15, 2024).

[155] Microtrac. "Analysis of particules size distribution." Microtrac Particle Characterization. https://www.microtrac.pt/pt/base-de-conhecimento/particle-size-distribution/ (accessed Jul. 24, 2024).

[156] T. Albrektsson and C. Johansson, "Osteoinduction, osteoconduction and osseointegration," *European Spine Journal,* vol. 10, no. 2, pp. S96-S101, Oct. 2001, doi: https://doi.org/10.1007/s005860100282.

8. Appendix

To maintain consistency with the structure of the work, the following images are presented at higher magnification and with greater detail, allowing the reader to closely follow and visually correlate with the descriptions provided in the text.

List of Figures

8.1. Musculoskeletal disorders graphics

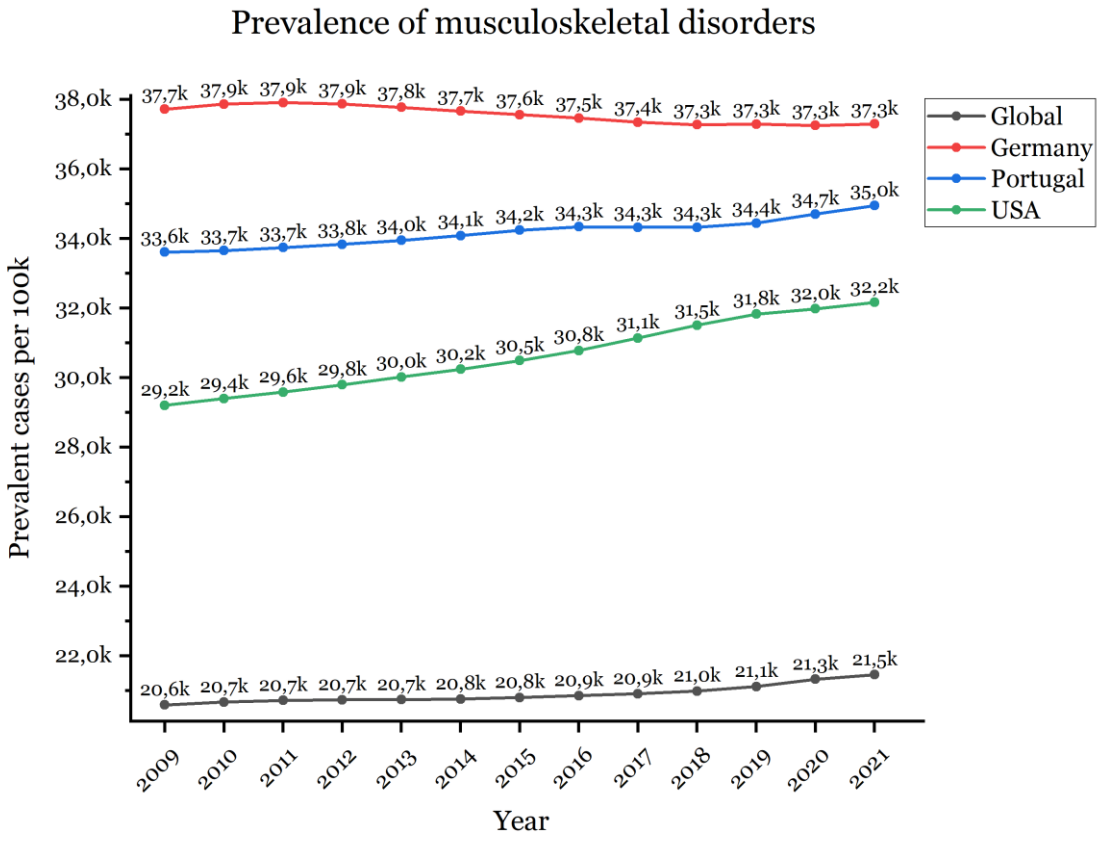

Figure 0.1. Medium of prevalence of musculoskeletal disorders per 100 thousand individuals.

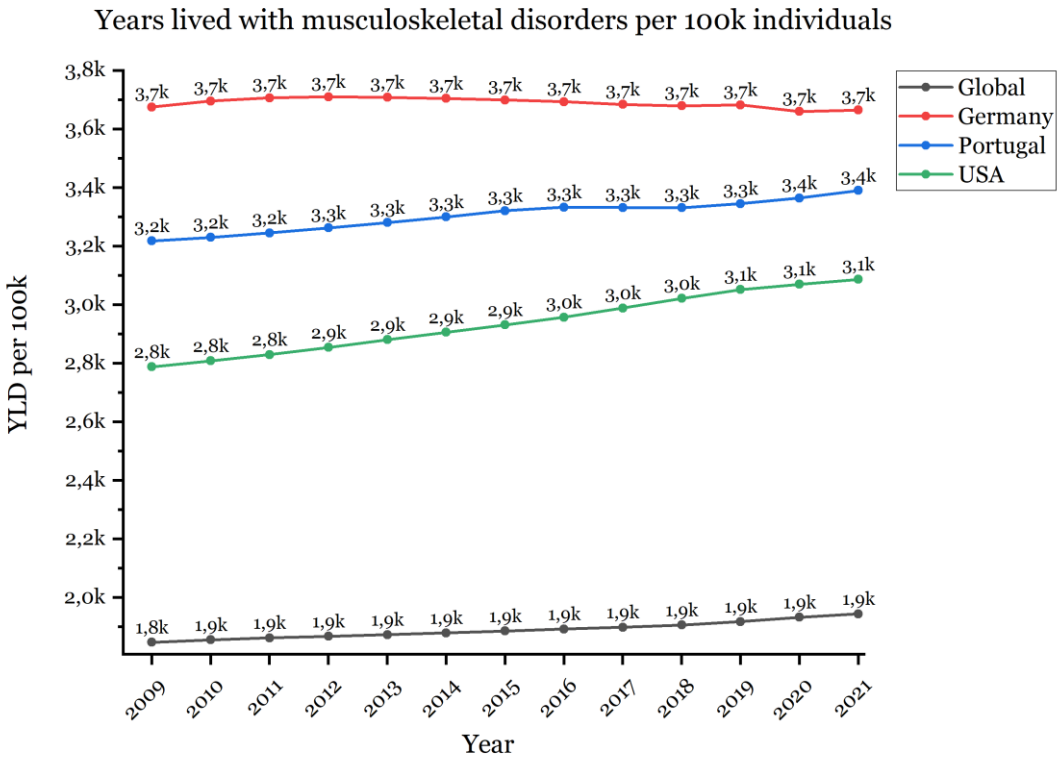

Figure 0.2. Medium of years lived with musculoskeletal disorders per 100 thousand individuals.

8.2. Samples images during ultimate strength test

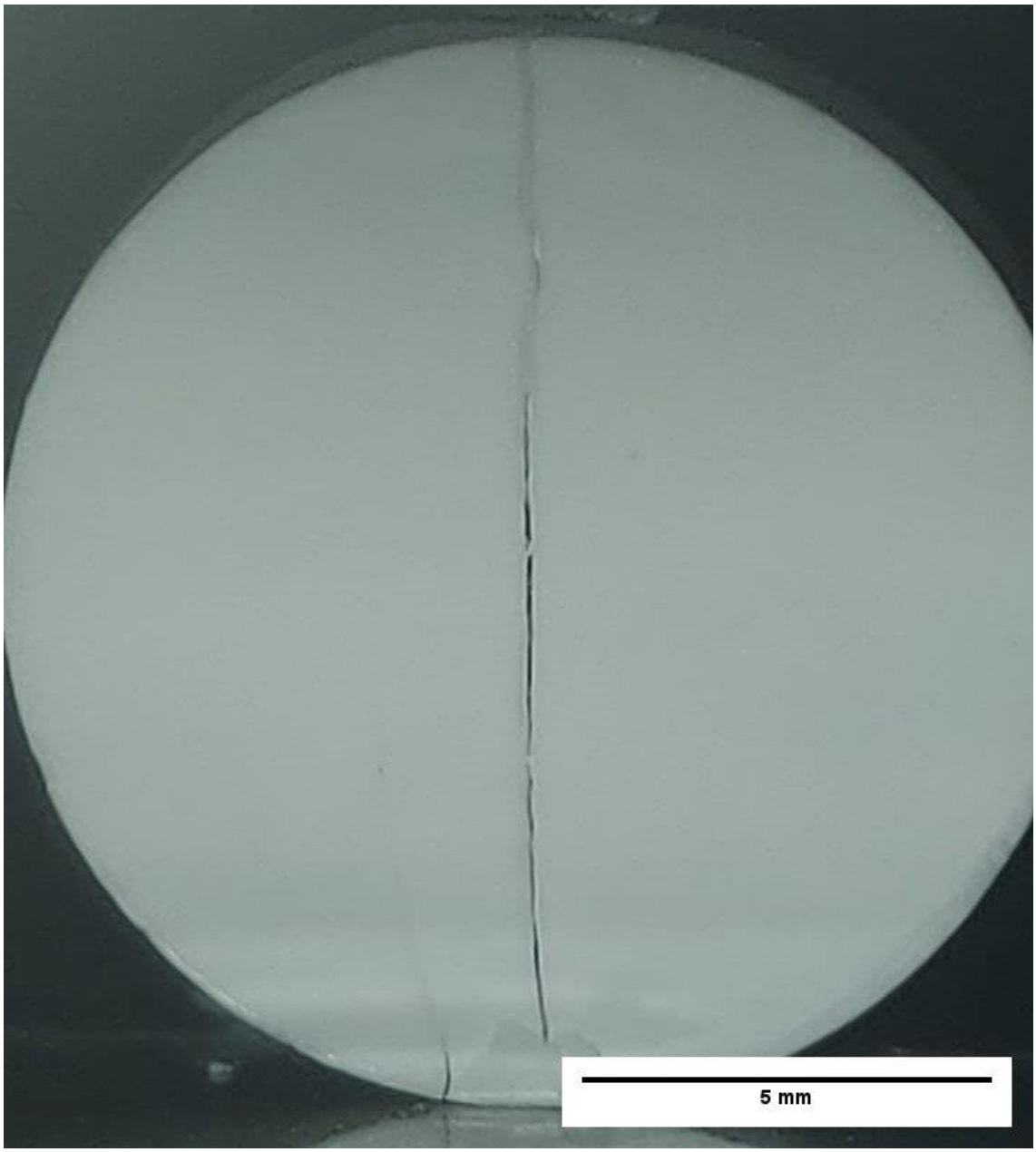

Figure 0.3. Appearance of a valid control sample after diametral compression.

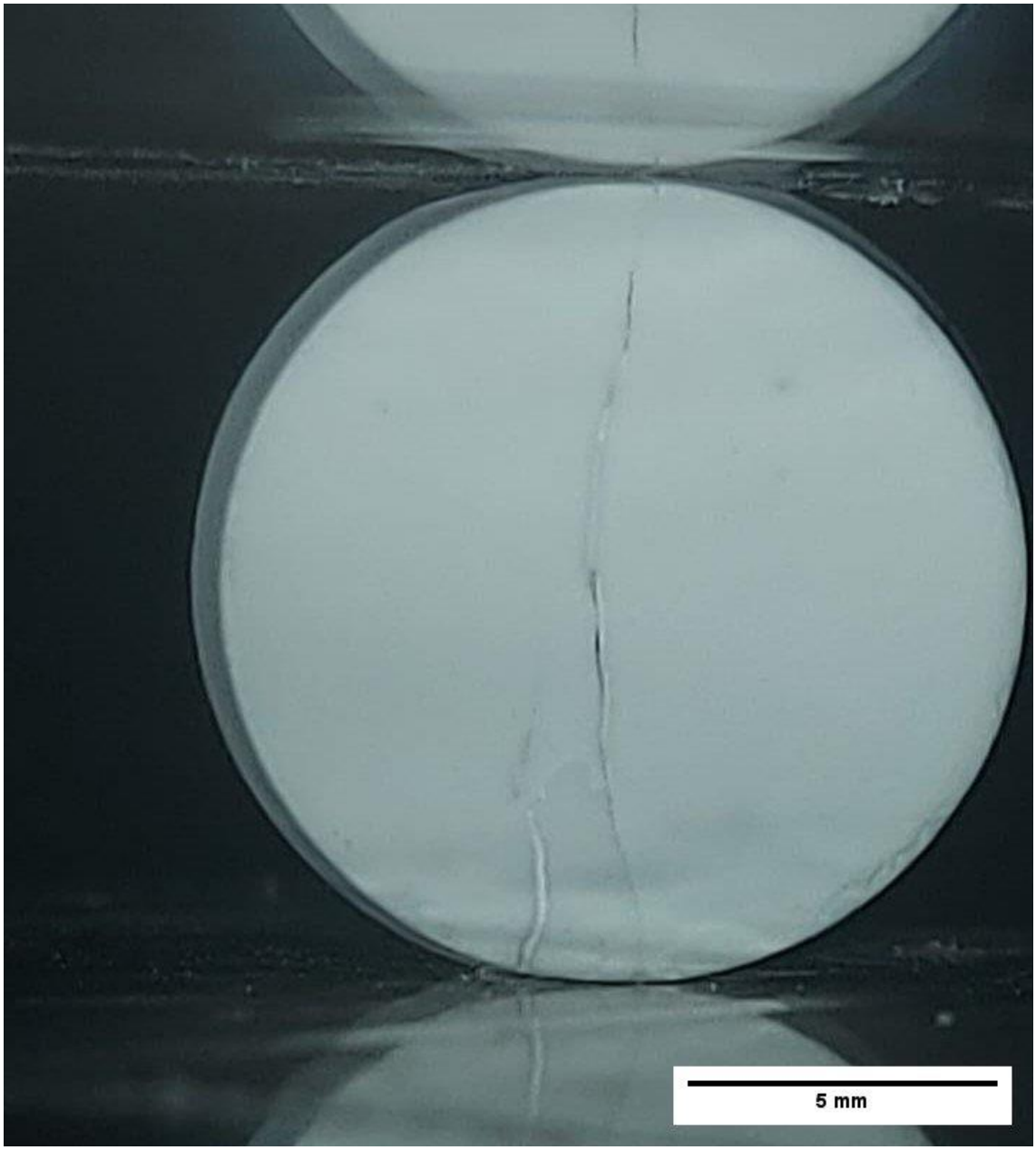

Figure 0.4. Appearance of a valid tantalum 3% sample after diametral compression.

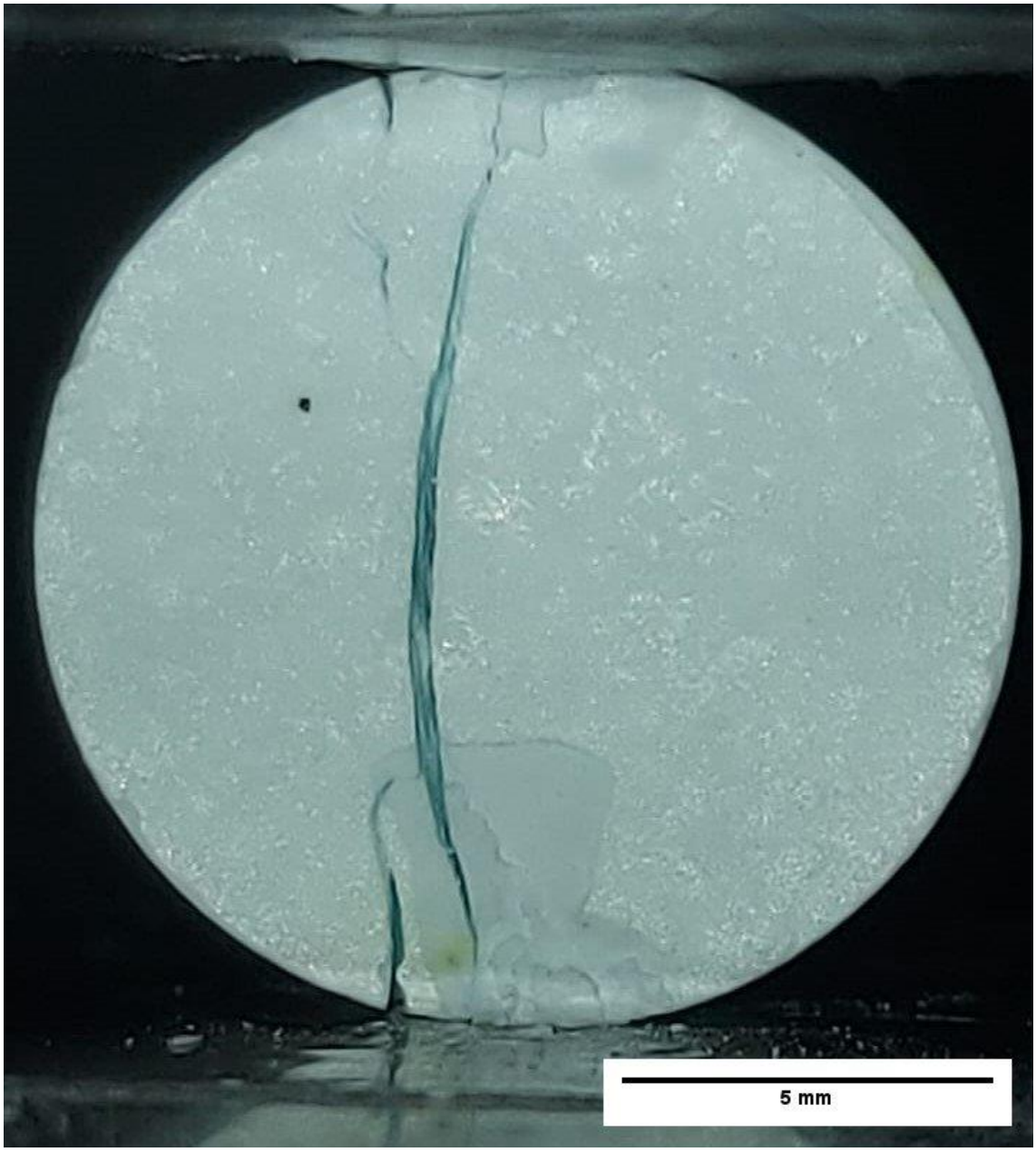

Figure 0.5. Appearance of a valid strontium 3% sample after diametral compression.

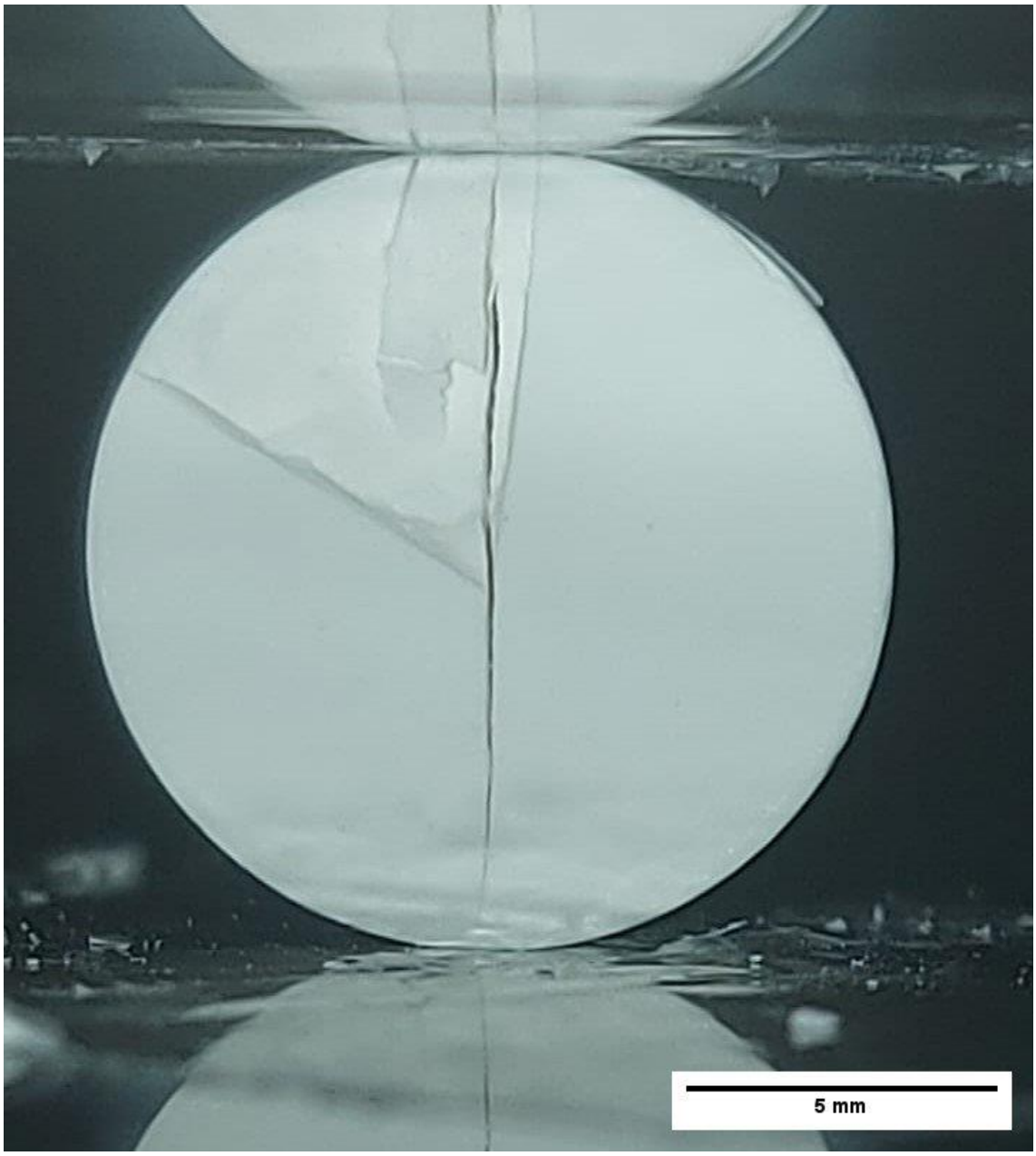

Figure 0.6. Appearance of valid Ta/Sr 1.5% sample after diametral compression.

8.3. Vickers Hardness Test image for each composition

In these SEM images, dashed red lines delineate the boundaries within which the Vickers test was conducted.

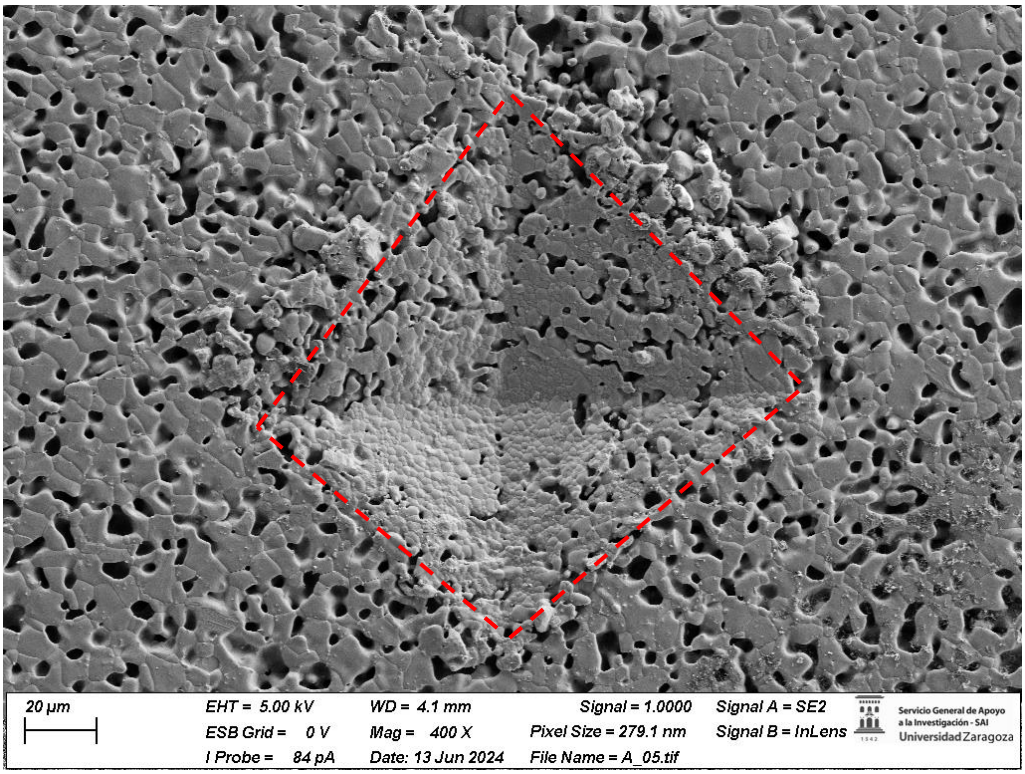

Figure 0.7. Result from Vickers Hardness Test for control at a magnification of 400x.

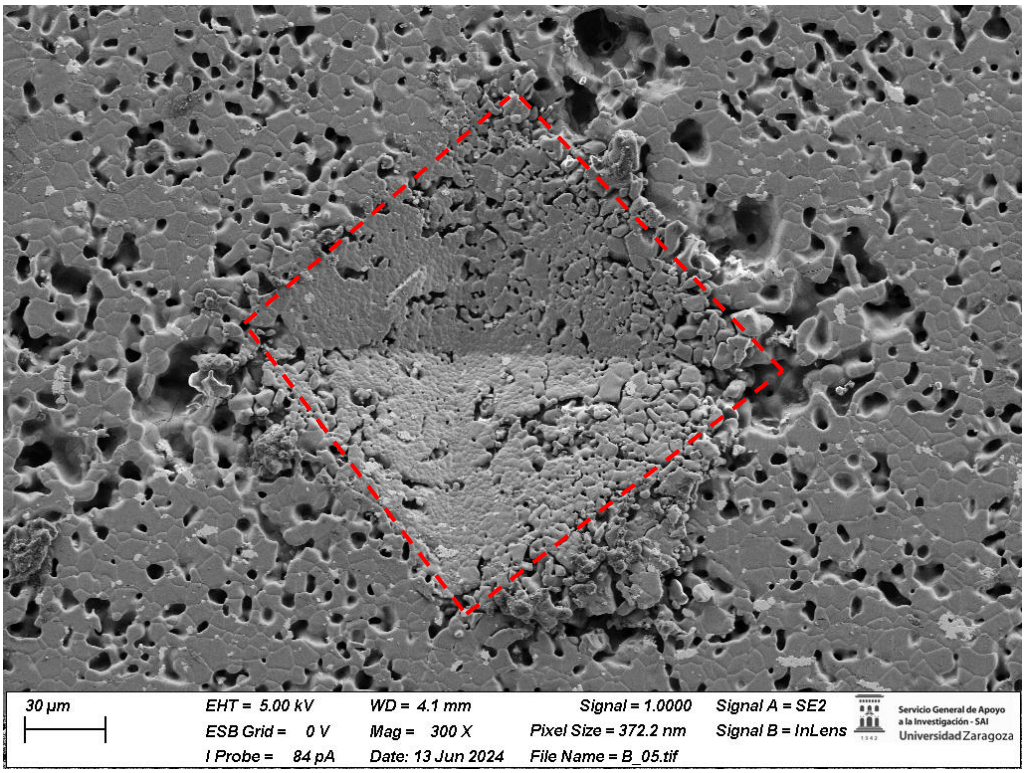

Figure 0.8. Result from Vickers Hardness Test for Ta 3% at a magnification of 300x.

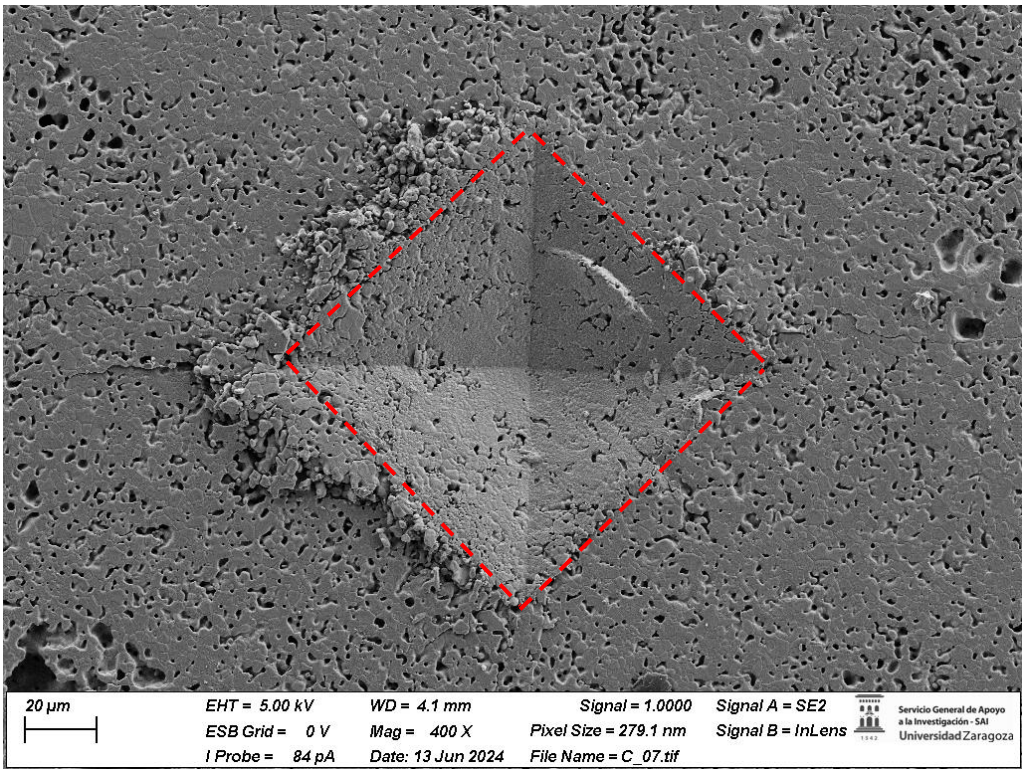

Figure 0.9. Result from Vickers Hardness Test for Sr 3% at a magnification of 400x.

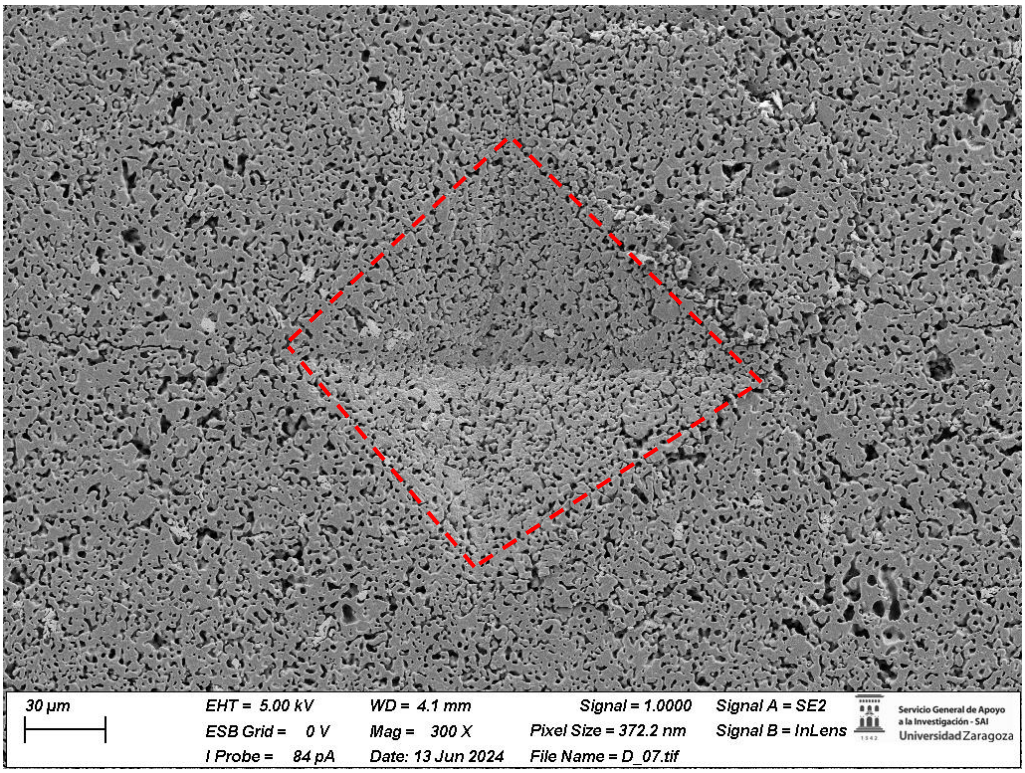

Figure 0.10. Result from Vickers Hardness Test for Ta/Sr 1.5% at a magnification of 300x.

8.4. Surface Images for each composition

In this SEM images, Figure 0.5b, 0.6b,0.7b, and 0.8b, the green arrows point to circular pores, red arrows point to cylindrical arrows, yellow arrows corresponding to faceted grains, blue arrows cylindrical grains, and orange arrows to circular grains.

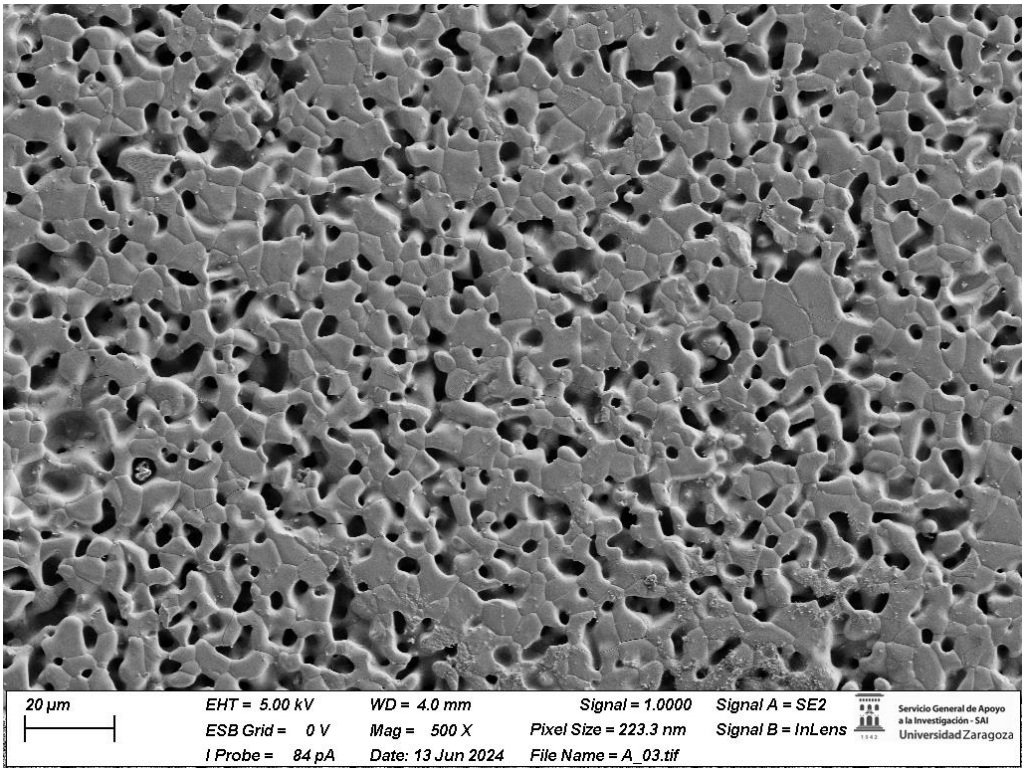

Figure 0.11. SEM image of the surface of control sample at 500x magnification.

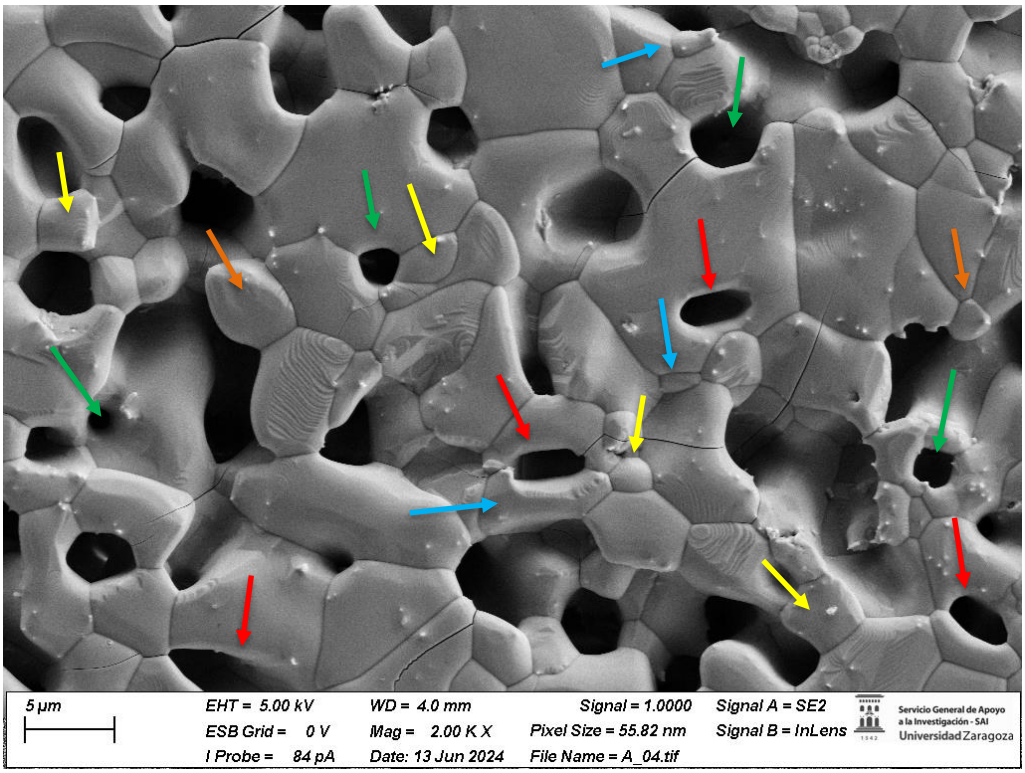

Figure 0.12. SEM image of the surface of control sample at 2000x magnification.

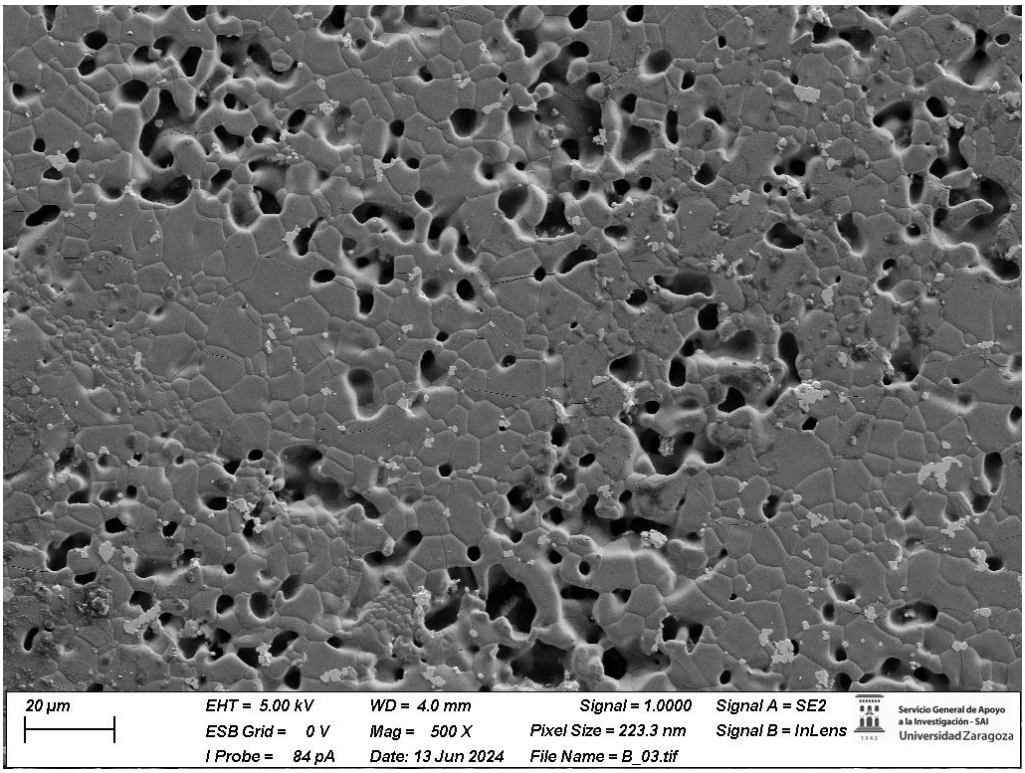

Figure 0.13. SEM image of the surface of Ta 3% sample at 500x magnification..

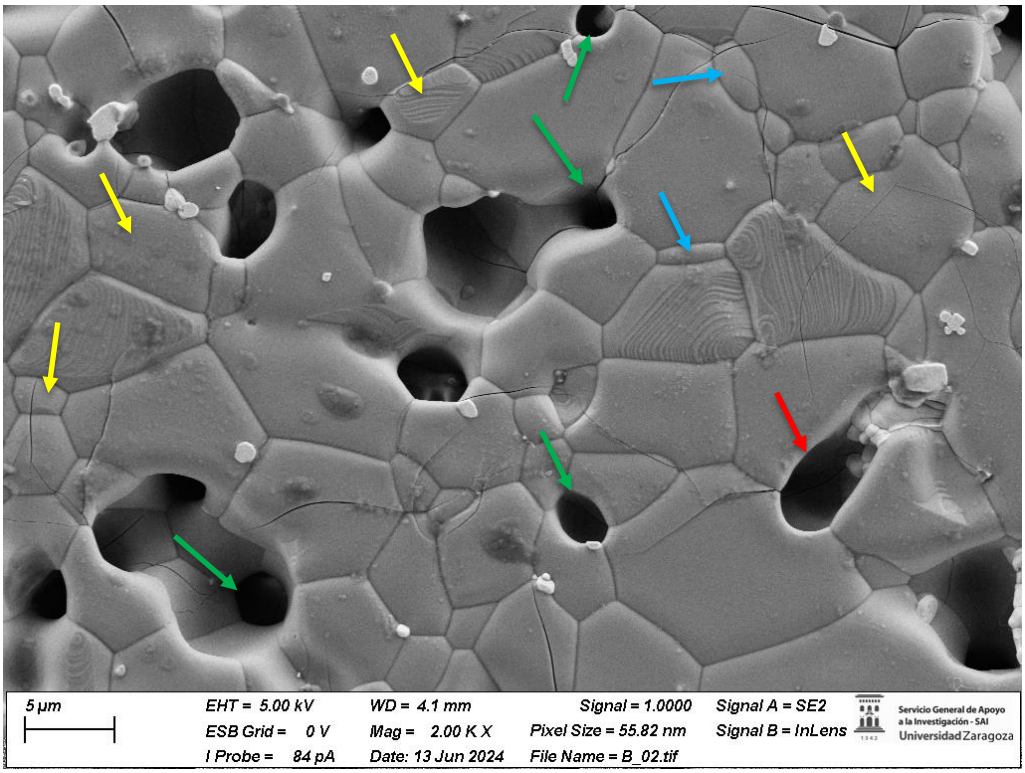

Figure 0.14. SEM image of the surface of Ta 3% sample at 2000x magnification.

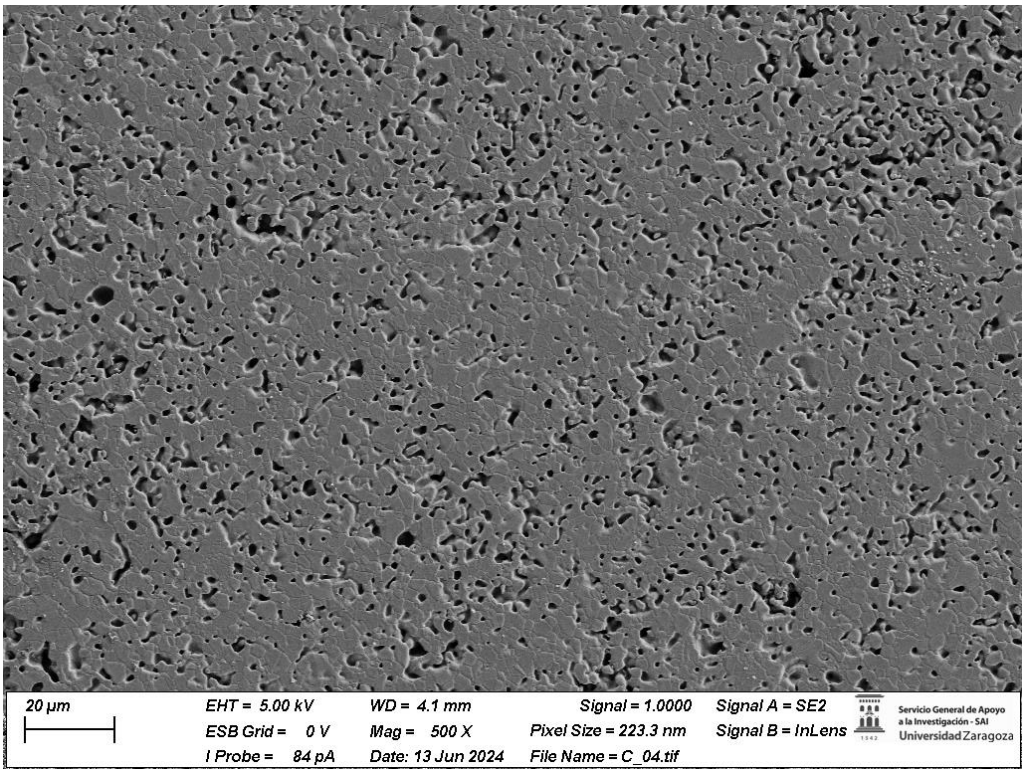

Figure 0.15. SEM image of the surface of Sr 3% sample at 500x magnification.

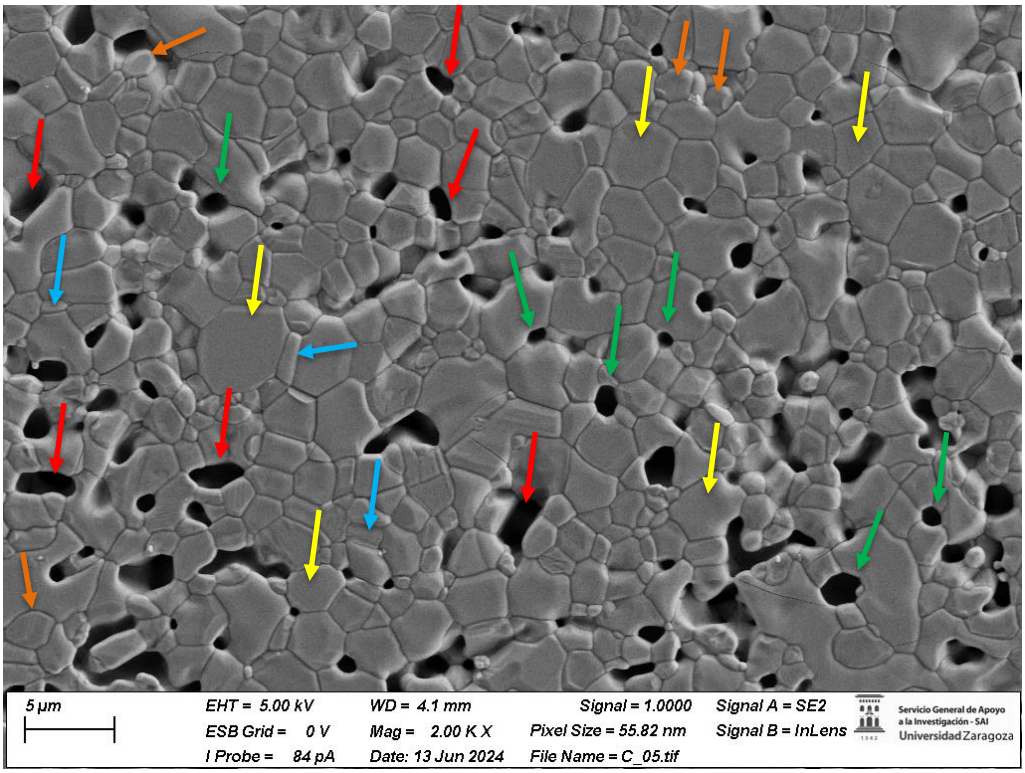

Figure 0.16. SEM image of the surface of Sr 3% sample at 2000x magnification.

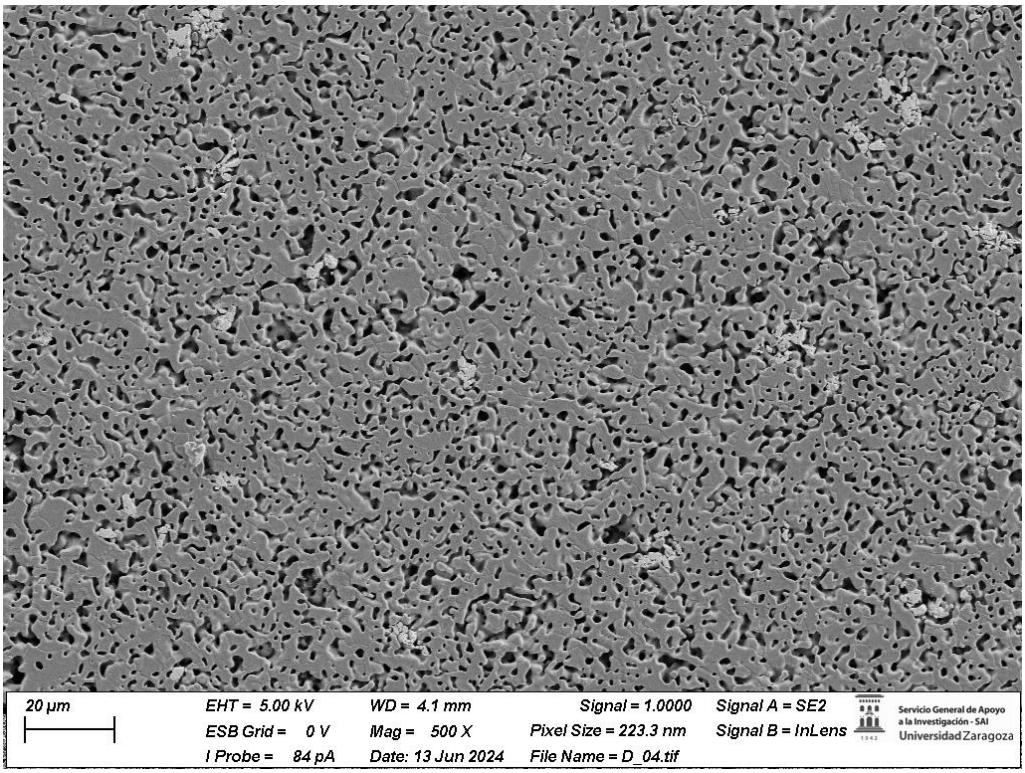

Figure 0.17. SEM image of the surface of Ta/Sr 1.5% sample at 500x magnification.

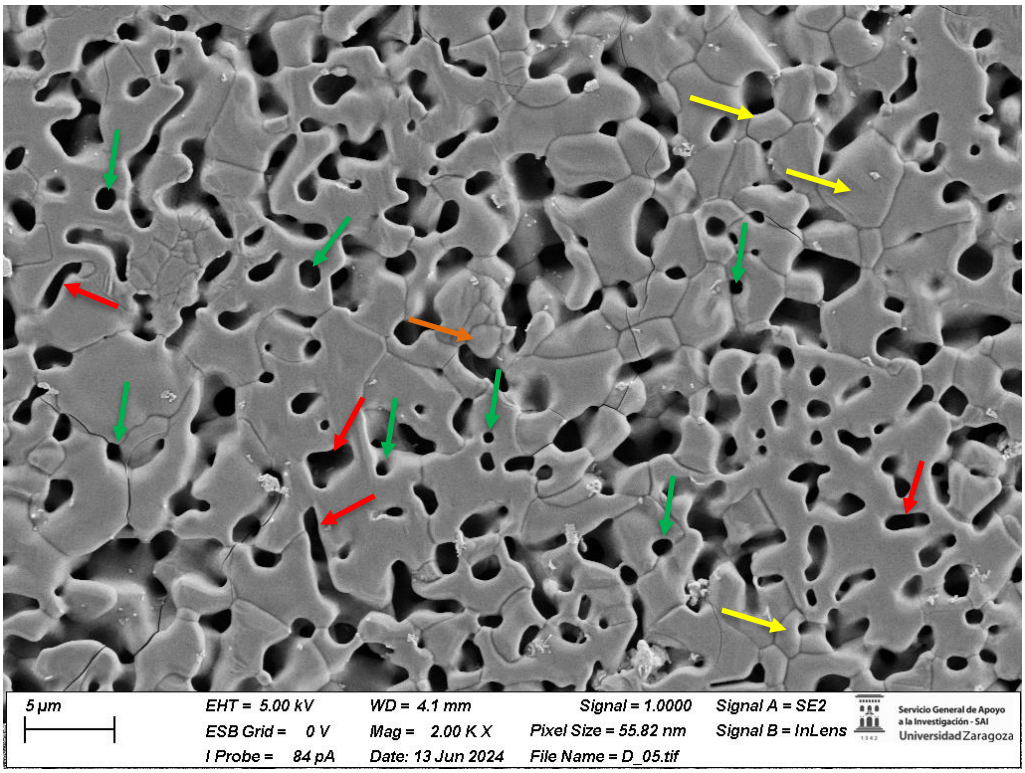

Figure 0.18. SEM image of the surface of Ta/Sr 1.5% sample at 2000x magnification.

8.5. Fracture surface images for each composition.

In this SEM images, Figure 0.9b, 0.10b, 0.11b, and 0.12b, fracture surfaces of transgranular and intergranular types, T and I, respectively, are indicated.

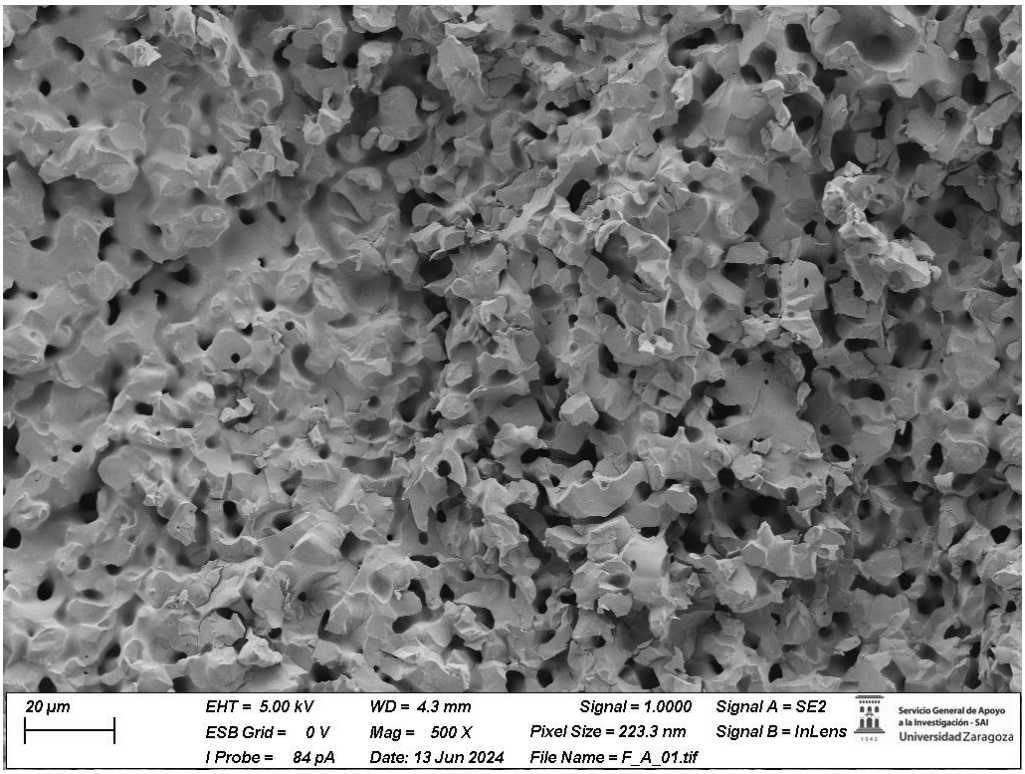

Figure 0.19. SEM image of the fracture surface of control sample at 500x magnification.

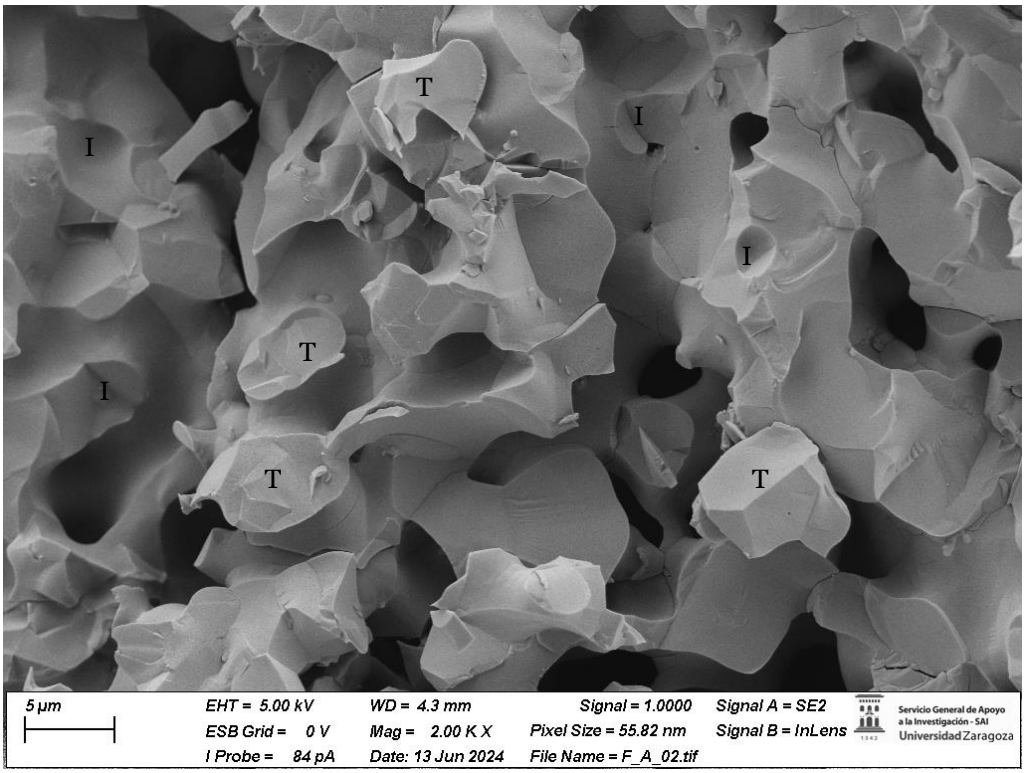

Figure 0.20. SEM image of the fracture surface of control sample at 2000x magnification.

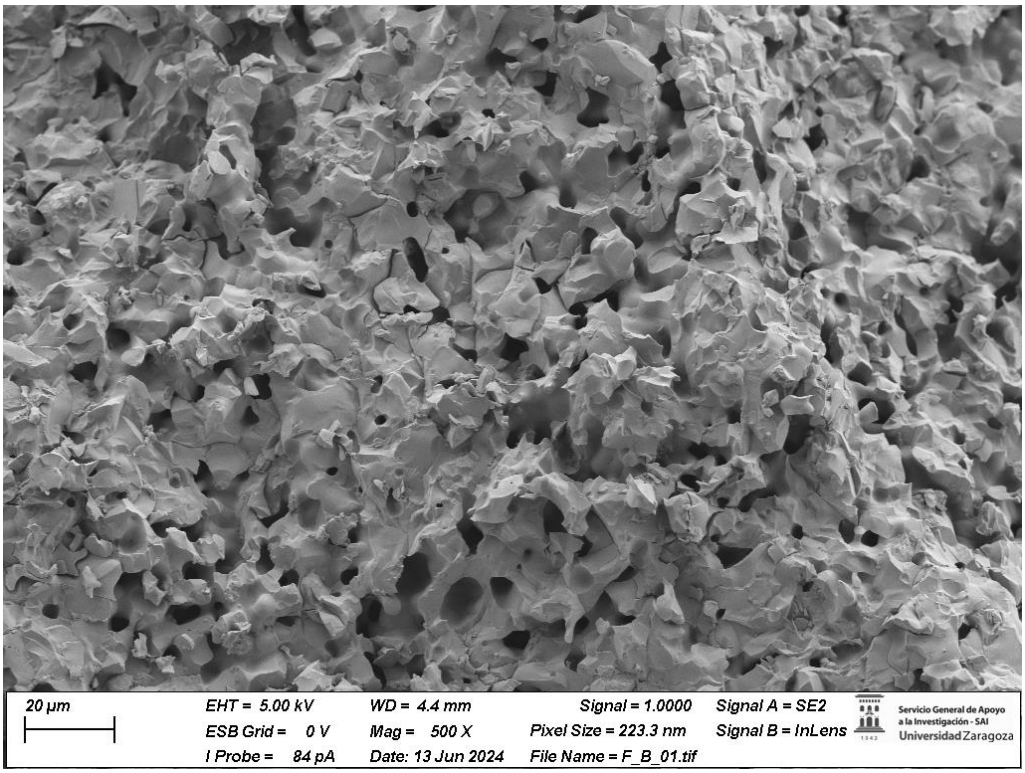

Figure 0.21. SEM image of the fracture surface of Ta 3% sample at 500x magnification.

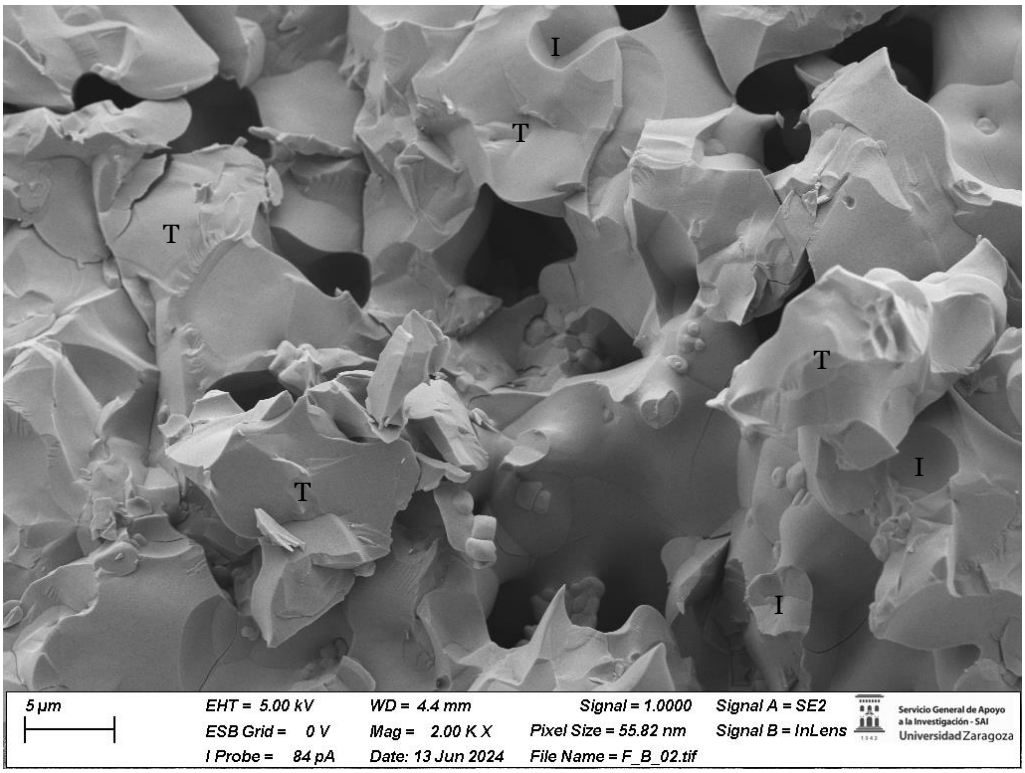

Figure 0.22. SEM image of the fracture surface of Ta 3% sample at 2000x magnification.

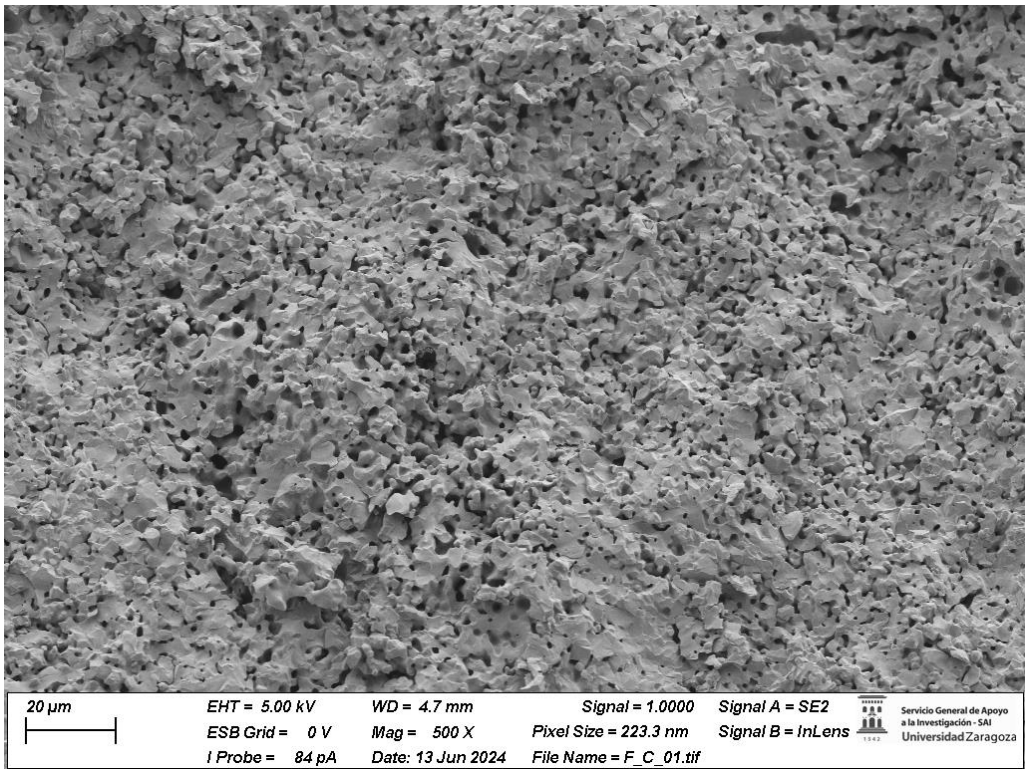

Figure 0.23. SEM image of the fracture surface of Sr 3% sample at 500x magnification.

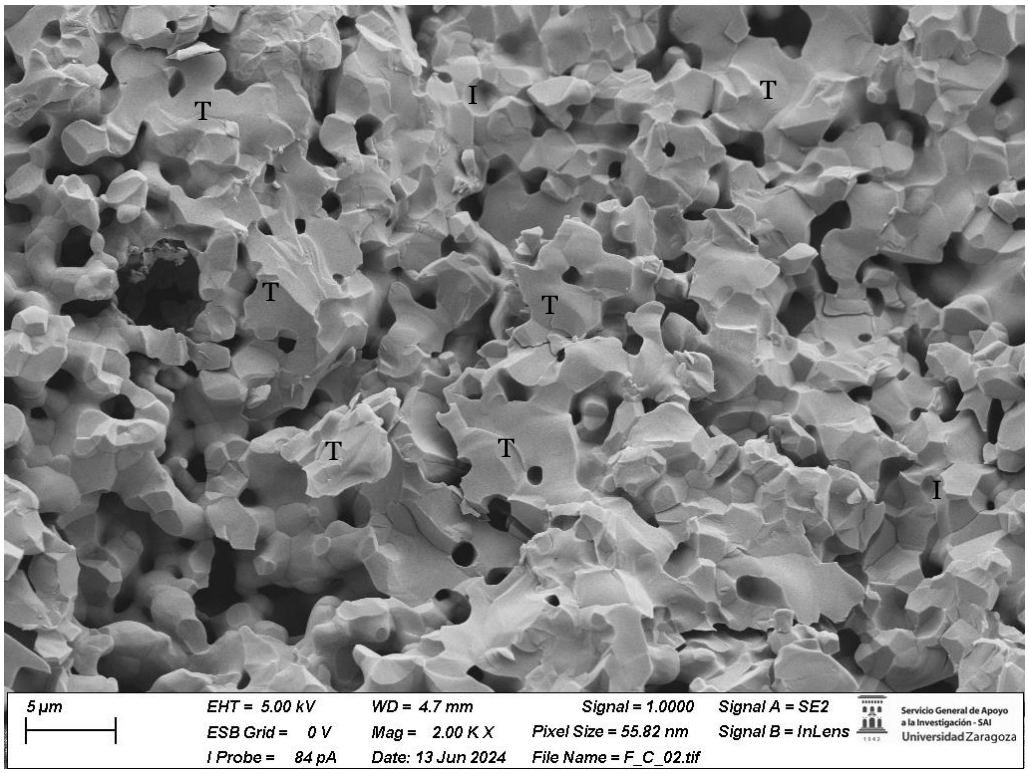

Figure 0.24. SEM image of the fracture surface of Sr 3% sample at 2000x magnification.

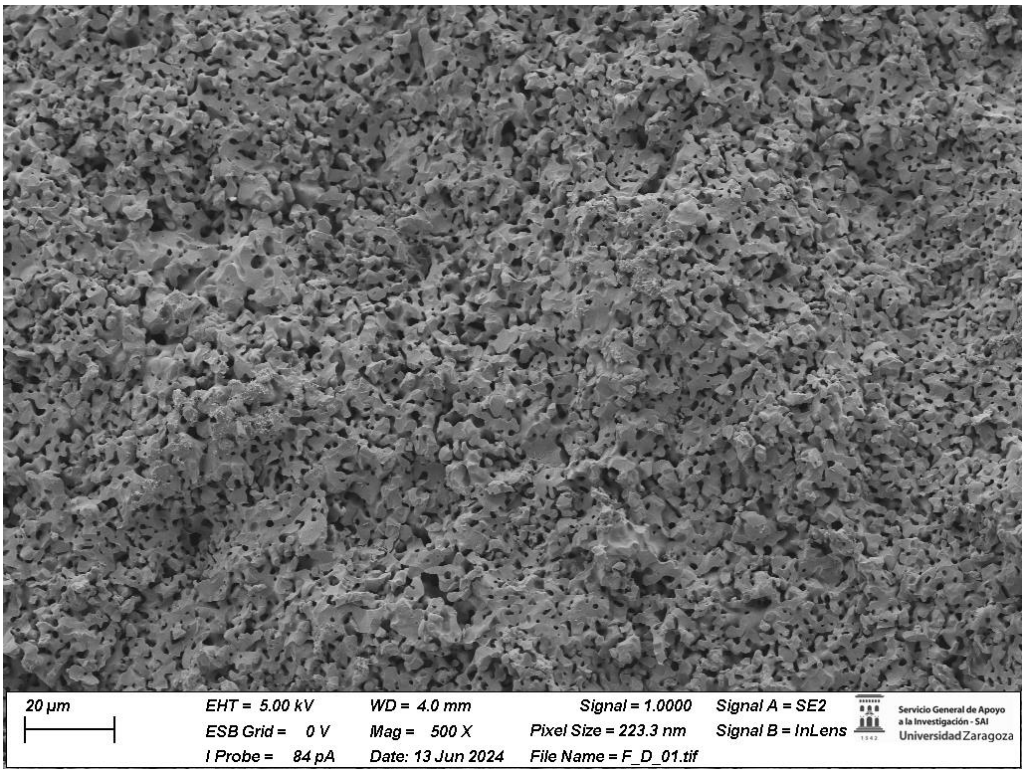

Figure 0.25. SEM image of the fracture surface of Ta/Sr 1.5% sample at 500x magnification.

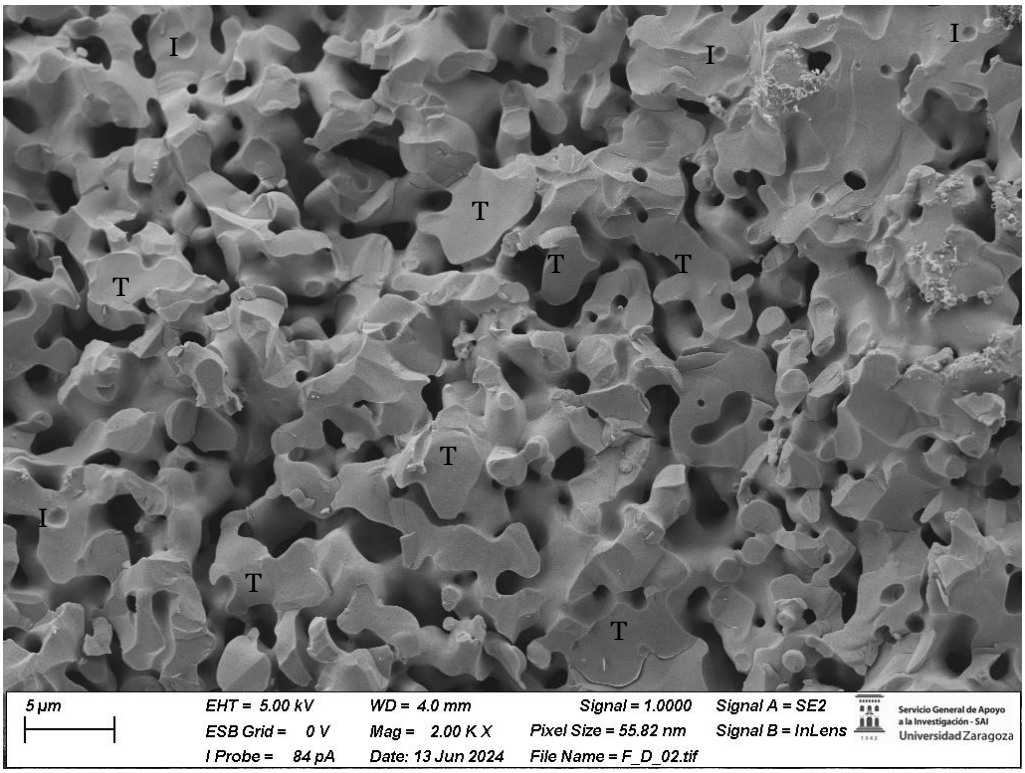

Figure 0.26. SEM image of the fracture surface of Ta/Sr 1.5% sample at 2000x magnification.

8.6. Surface images of the sol-gel coatings for each composition.

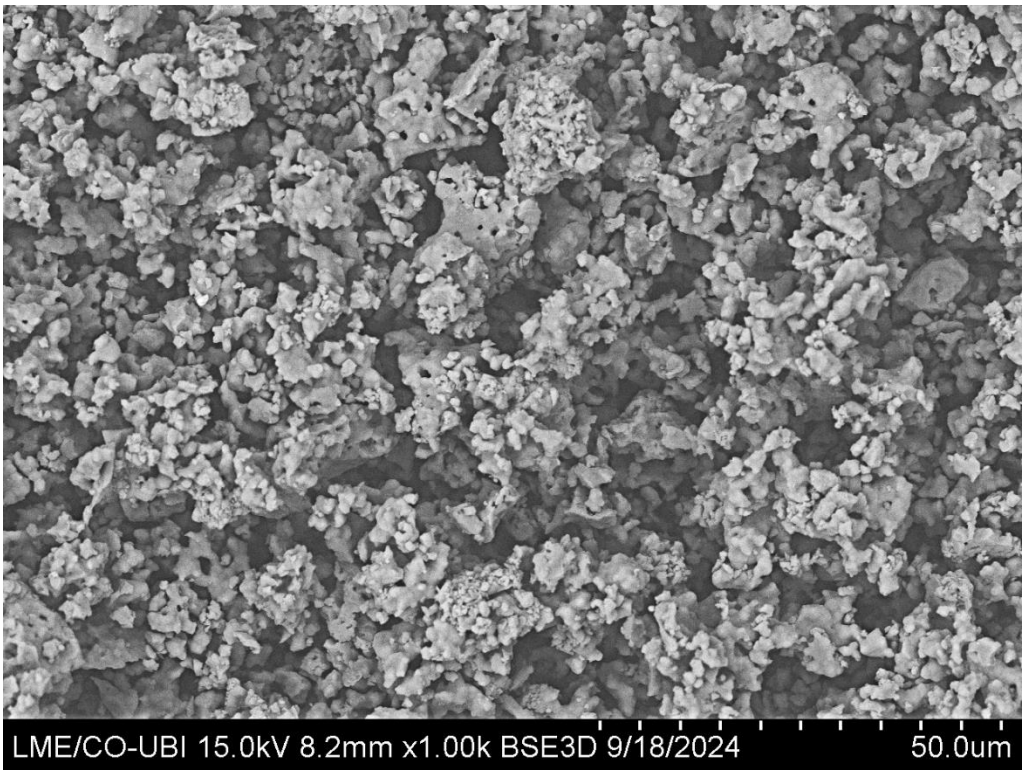

Figure 0.27. SEM images of the sol-gel coating surface for each the control sample at 1000x of magnification.

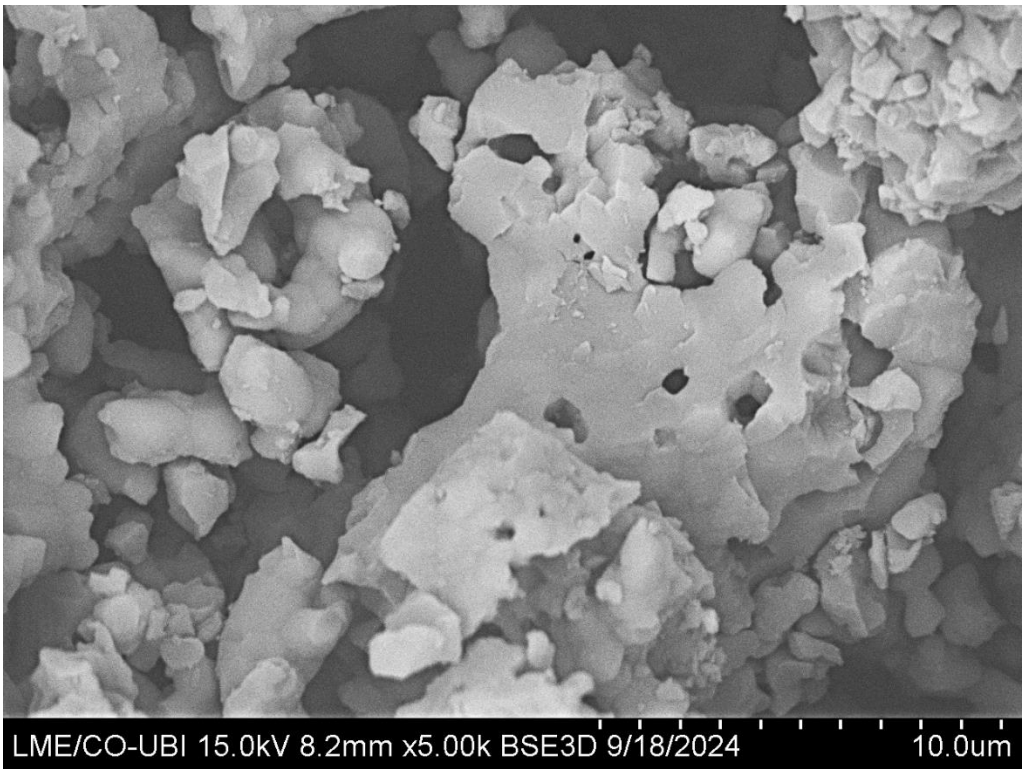

Figure 0.28. SEM images of the sol-gel coating surface for control sample at 5000x of magnification.

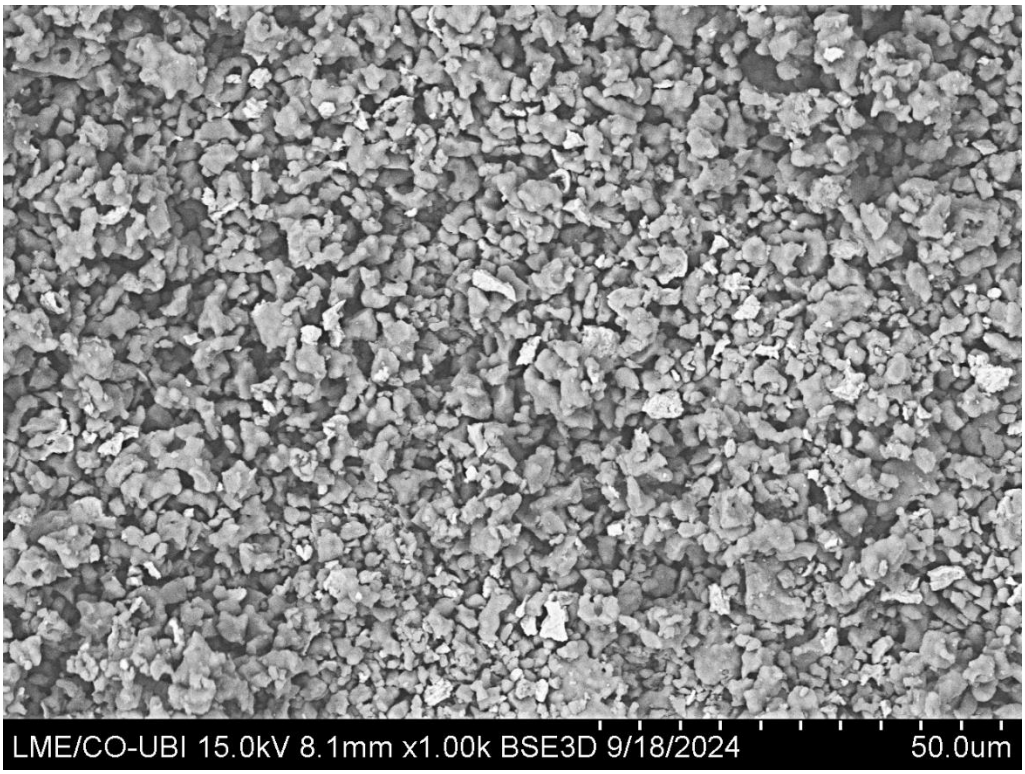

Figure 0.29. SEM images of the sol-gel coating surface for Ta 3% sample at 1000x of magnification.

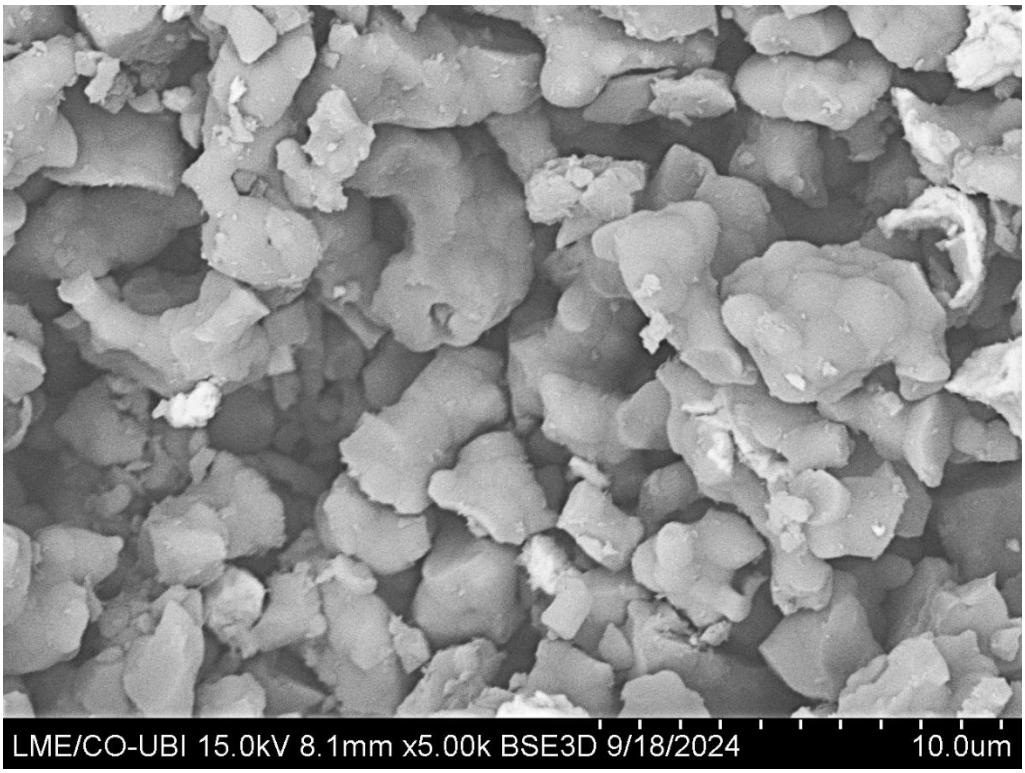

Figure 0.30. SEM images of the sol-gel coating surface for Ta 3% sample at 5000x of magnification.

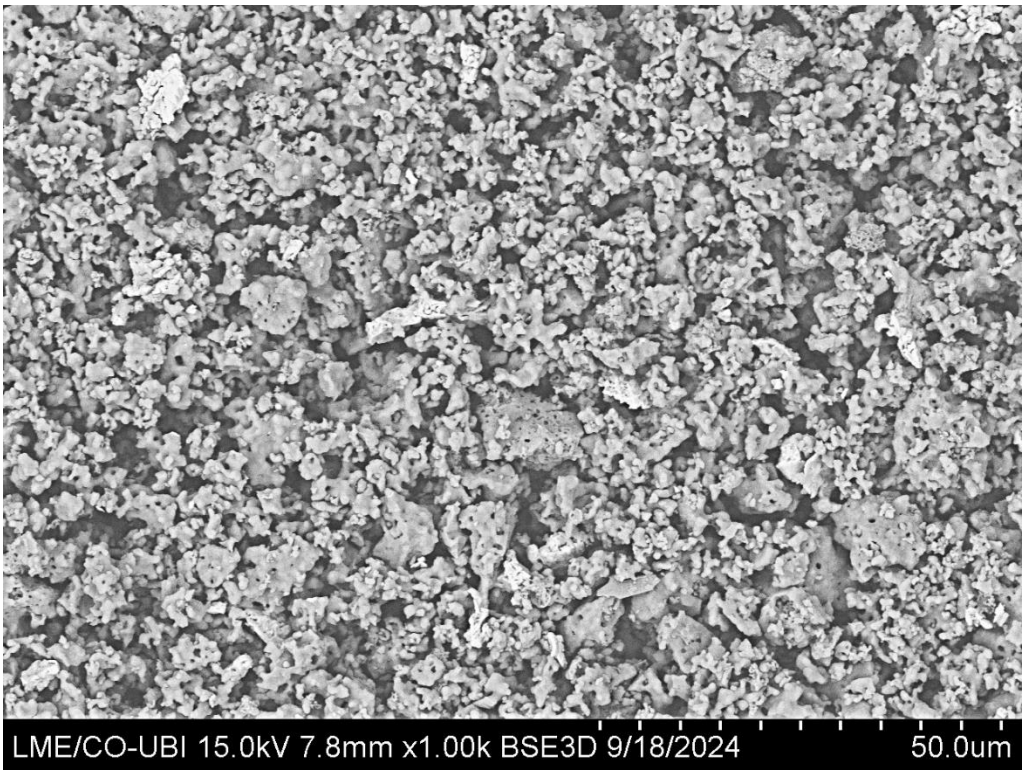

Figure 0.31. SEM images of the sol-gel coating surface for Sr 3% sample at 1000x of magnification.

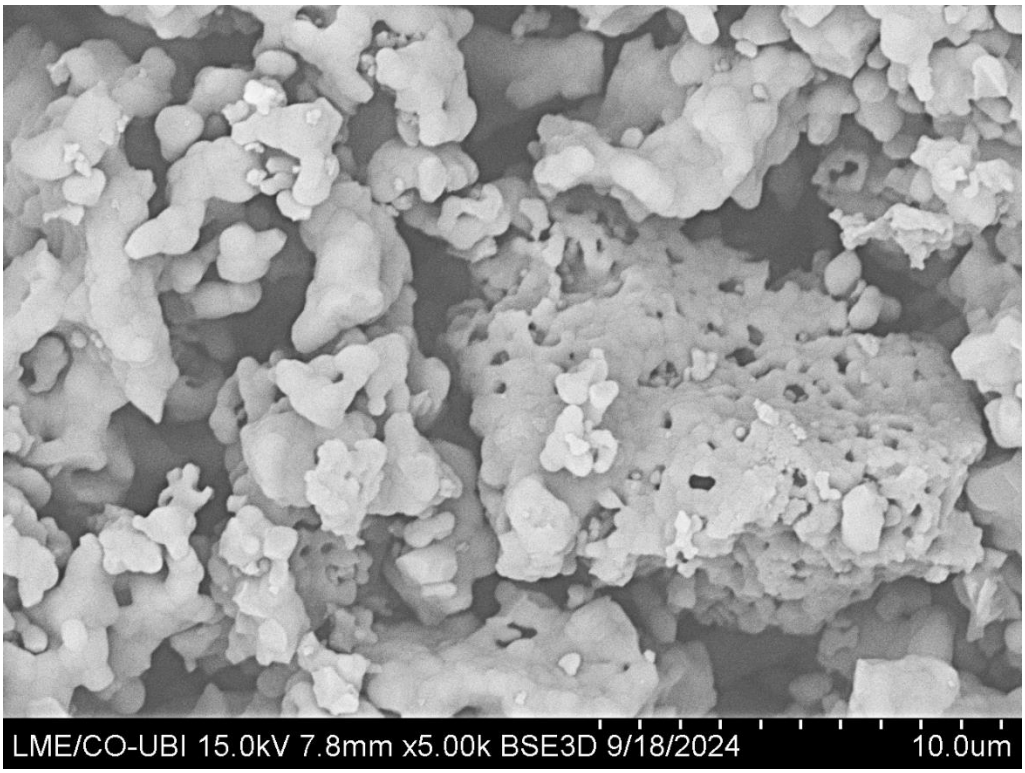

Figure 0.32. SEM images of the sol-gel coating surface for Sr 3% sample at 5000x of magnification.

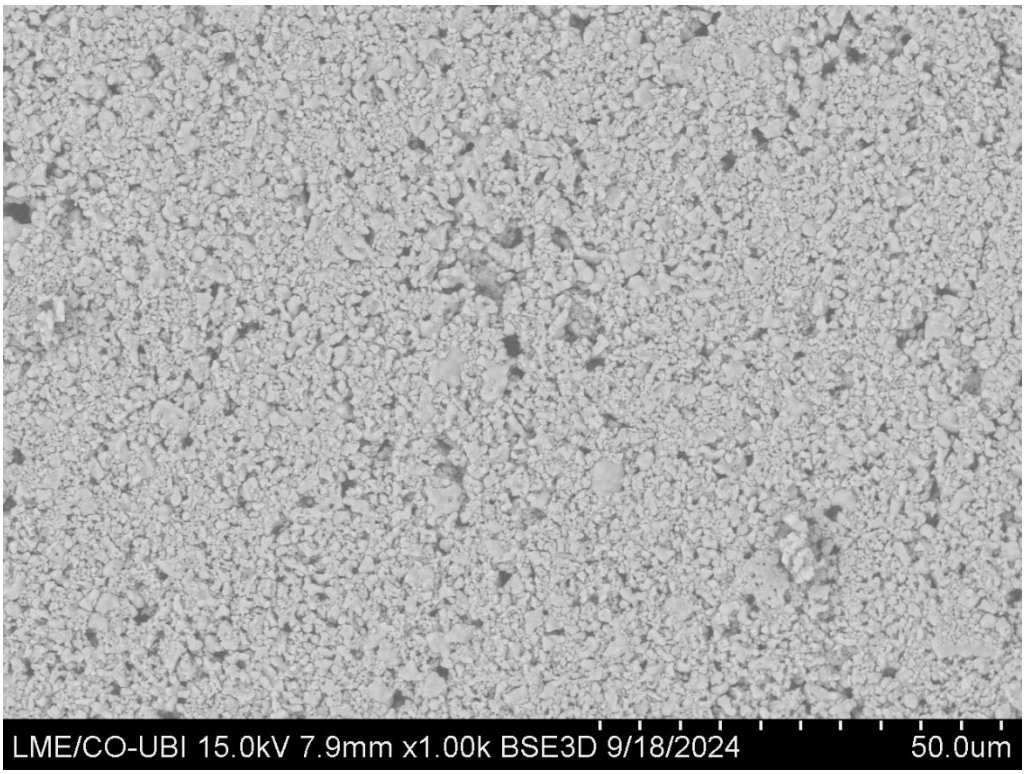

Figure 0.33. SEM images of the sol-gel coating surface for Ta/Sr 1.5% sample at 1000x of magnification.

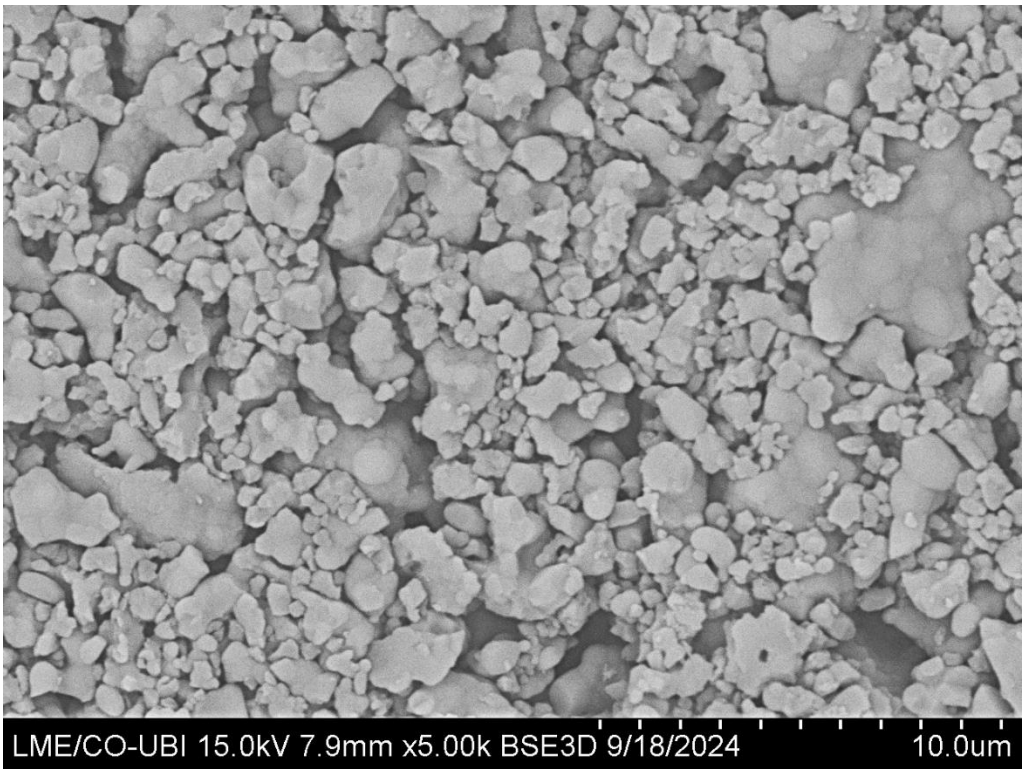

Figure 0.34. SEM images of the sol-gel coating surface for Ta/Sr 1.5% sample at 5000x of magnification.